

TABLES DES MATIÈRES

CHAPITRE 1 – Introduction générale	1
1.1 Introduction	1
1.2 Concepts fondamentaux	2
1.2.1 Les éléments du groupe du platine (EGP)	2
1.2.2 Le fractionnement des EGP	4
1.2.2.1 La fusion partielle	4
1.2.2.2 La cristallisation fractionnée des magmas saturés en sulfures	6
1.2.2.3 La cristallisation fractionnée des magmas sous-saturés en sulfures	7
1.3 Problématique	11
1.3.1 Les hypothèses	12
1.3.2 Les objectifs	13
1.4 Terrain d'étude	15
1.4.1 La Grande Province Ignée d'Emeishan	15
1.4.2 Les picrites d'Emeishan	17
1.5 Méthodologie	18
1.5.1 Échantillonnage	18
1.5.2 Étude pétrographique	19
1.5.3 Étude géochimique	20
1.6 Format du mémoire	21
1.7 Contributions de l'auteur et des collaborateurs	21
1.8 Références	23
 CHAPITRE 2 – The effect of chromite crystallization on the fractionation of osmium, iridium, ruthenium and rhodium in picritic magmas: an example from the Emeishan Large Igneous Province, south-western China	 32
2.1 Abstract	33
2.2 Introduction	35
2.3 Geological background	39
2.4 Samples locations and analytical methods	44
2.5 Results	55
2.5.1 Petrography of picrites and associated rocks	55
2.5.2 Chemical classification of picrites	60
2.5.3 Whole-rock major and trace element compositions	61

2.5.4 Primary mineral assamblage	71
2.5.4.1 Olivine	71
2.5.4.2 Chromite	73
2.5.4.3 Clinopyroxene	76
2.5.5 IPGE and Rh in chromites determined by LA-ICP-MS	76
2.5.6 Presence of PGM grains related to the Emeishan chromites	81
2.6 Discussion	84
2.6.1 The effects of sulphide removal on PGE concentrations in whole-rock	84
2.6.2 The enrichment of IPGE and Rh in chromites	87
2.6.3 Chromite-hosted PGM: evidence of a syn-chromite crystallization origin	91
2.6.4 Determination of the fraction of chromite in the Emeishan volcanic rocks	93
2.6.5 Partition coefficients for IPGE and Rh between chromite and picrite, and mass balance calculations	100
2.6.6 The effects of chromite crystallization on IPGE and Rh concentrations in whole rock: a model for the ELIP	105
2.7 Conclusions	110
2.8 Acknowledgments	113
2.9 References	113
 CHAPITRE 3 – Conclusions générales	 126
3.1 Introduction	126
3.2 Les chromites d'Emeishan	126
3.3 Association IEGP(Rh)-chromite	127
3.3.1 Concentrations en IEGP et en Rh, coefficients de partage et calculs de bilan de masse	127
3.3.2 Processus d'enrichissement en IEGP et en Rh	129
3.3.3 MGP en association avec la chromite	130
3.4 Évolution magmatique et fractionnement des IEGP et du Rh	130
3.5 Travaux futurs	132
3.6 Références	133

LISTE DES TABLEAUX

Table 1: Whole rock major oxide and trace element contents of the Emeishan picrites and basalts (recalculated to 100% anhydrous) _____	48
Table 2: Representative olivine, chromite and clinopyroxene microprobe analyses _____	52
Table 3: Representative IPGE and Rh concentrations in chromite determined by LA-ICP-MS _____	54
Table 4: Compositions of PGM from the Emeishan picrites determined by semi-quantitative analyses _____	84
Table 5: Weight and volume percent chromite present in each sample _____	98
Table 6: Empirical partition coefficients for IPGE and Rh into chromite _____	103

LISTE DES FIGURES

CHAPITRE 1

Figure 1.1: Représentation schématique des hypothèses envisageables pour expliquer l’association IEGP(Rh)-chromite _____ 13

Figure 1.2: Carte des divisions tectoniques de la Chine montrant la localisation de la Grande Province Ignée d’Emeishan _____ 16

CHAPITRE 2

Figure 2.1: Schematic geological map showing the distribution of the flood basalt successions in the ELIP, south-western China _____ 43

Figure 2.2: Transmitted and reflected light photomicrographs of picrites and associated rocks _____ 59

Figure 2.3: Relationships between Ti/Y and Sm/Yb for picrites and OPSV rocks _____ 61

Figure 2.4: Whole-rock major elements (SiO_2 , TiO_2 , Al_2O_3 , $\text{Fe}_2\text{O}_3^{\text{Total}}$ and CaO) plotted against MgO _____ 63

Figure 2.5: Whole-rock Ni, Cr and Cu plotted against MgO _____ 65

Figure 2.6: Primitive mantle-normalized Ni–PGE–Cu patterns for picrites and associated rocks _____ 68

Figure 2.7: Whole-rock PGE plotted against Cr _____ 70

Figure 2.8: Diagrams showing variation of MnO and NiO against Fo for the olivine phenocrysts from picrites and OPSV rocks _____ 72

Figure 2.9: Diagrams showing variation of Al_2O_3 , Cr_2O_3 and Mg# against TiO_2 contents of chromites	75
Figure 2.10: Chemical profiles (Cr, V, Zn, Os, Ir, Ru and Rh), in counts per second vs. time (in seconds), from <i>in situ</i> LA-ICP-MS analyses of chromites	78
Figure 2.11: Primitive mantle-normalized IPGE–Rh patterns for chromites	80
Figure 2.12: Diagrams showing variation of Ir against Os, and Os, Ir and Rh against Ru for individual chromites	81
Figure 2.13: Backscattered electron images of platinum-group minerals	83
Figure 2.14: Relationships between Cu/Pd ratios and Pd concentrations	87
Figure 2.15: Variation of Rh against $\text{Fe}^{3+}/\text{R}^{3+}$ in chromites from the Emeishan volcanic rocks and the Ambae lavas	89
Figure 2.16: Volume percent of olivine phenocryst vs. volume percent of chromite for the picrite samples	97
Figure 2.17: Partition coefficients for IPGE and Rh between chromite and silicate melt established empirically from natural rocks and from experimental petrology	101
Figure 2.18: Diagrams of mass balance calculations showing the proportion of whole-rock IPGE and Rh accounted for by the chromite	105
Figure 2.19: Modelling of the combined effects of olivine and chromite crystallization and the late timing of sulphide liquid segregation on Ru concentrations	107
Figure 2.20: Primitive mantle-normalized IPGE–Rh patterns for the studied flood basalts and the predicted liquid from the numerical modelling	109

LISTE DES ANNEXES

Annexe 1: Localisation des échantillons	136
Annexe 2: Analyses roches totales	137
Annexe 3: Matériaux de références pour les analyses roches totales	146
Annexe 4: Analyses minérales par microsonde	150
Annexe 5: Analyses de chromite par LA-ICP-MS	173
Annexe 6: Matériaux de références pour les analyses par LA-ICP-MS	179

CHAPITRE 1

INTRODUCTION GÉNÉRALE

1.1 INTRODUCTION

Ce chapitre est divisé en six sections distinctes qui sont dédiées à la présentation du cadre d'étude de ce mémoire de maîtrise. La première section (1.2) est une revue de la littérature qui consiste à présenter les concepts fondamentaux qui ont servi à développer la problématique de ce projet de recherche. La deuxième section (1.3) est consacrée à la mise en valeur de la problématique, aux hypothèses de travail qui en découlent ainsi qu'aux objectifs fixés afin de répondre à cette problématique. Les troisième et quatrième sections (1.4 et 1.5) sont davantage dédiées à la présentation du terrain d'étude ainsi qu'aux méthodes descriptives et analytiques permettant de tester les différentes hypothèses de travail. Finalement, les cinquième et sixième sections (1.6 et 1.7) sont employées à définir le format du mémoire et à dévoiler les contributions de l'auteur ainsi que de ces collaborateurs.

1.2 CONCEPTS FONDAMENTAUX

1.2.1 LES ÉLÉMENTS DU GROUPE DU PLATINE (EGP)

Les EGP (Os, Ir, Ru, Rh, Pt et Pd) sont des métaux de transitions du Groupe VIII situés dans les 5^e et 6^e rangées du tableau périodique. Ces éléments partagent avec le Fe et le Ni une tendance à former des liaisons métalliques qui leur procure la capacité de se concentrer sous la forme d'alliages ou de métaux purs, leur valant ainsi le titre d'élément sidérophiles (i.e., *iron-loving*; Goldschmidt, 1937; Barnes et Maier, 1999). D'autre part, comme pour le Cu, l'Ag, l'Au et plusieurs autres métaux de transitions, les EGP peuvent également former des liaisons covalentes avec le S, et par conséquent, se concentrer dans les phases sulfurées du manteau ou de la croûte, ce qui leur vaut aussi le titre d'éléments chalcophiles (i.e., *chalcogen-loving*).

De par leur comportement naturellement sidéophile, il est généralement accepté que les EGP auraient migré avec le Fe et le Ni lors de la formation du noyau, provoquant ainsi l'appauvrissement en EGP de la Terre Silicatée (*Silicate Earth*; e.g., Chou, 1978). Cependant, puisque la plupart des études réalisées à partir de roches volcaniques primitives et de xénolites mantelliques révèlent que les EGP sont relativement abondants dans le manteau supérieur (e.g., Chou, 1978; Chou et al., 1983; Morgan, 1986; Sun et al., 1991), un évènement postérieur à la formation du noyau doit avoir eu lieu pour expliquer cette abondance moderne. Communément appelé le *Late Veneer*, cet évènement correspond à l'accrétion tardive de matériaux extraterrestres causée par un bombardement météorique postérieur à la différenciation terrestre. D'après plusieurs chercheurs, le *Late Veneer* serait

à l'origine du réapprovisionnement de la Terre Silicatée en éléments sidérophiles tels que les EGP (e.g., Kimura et al., 1974; Chou et al., 1983; Morgan, 1986; McDonough et Sun, 1995). La distribution post-acrétionnelle des EGP dans le manteau et la croûte ne semble toutefois pas liée à leur caractère sidérophile, mais plutôt à leur capacité à former des liaisons avec le S, et donc, de se faire séquestrer par des liquides sulfurés (Barnes et Maier, 1999).

Il est conventionnel de subdiviser les EGP en fonction des comportements qu'ils adoptent durant les processus magmatiques qui subsistent dans le manteau et la croûte. Les éléments du sous-groupe de l'Ir, ou IEGP (Os, Ir et Ru), qui se comportent généralement comme des éléments compatibles et réfractaires, ont tendance à montrer une affinité pour les phases solides, tandis que les éléments du sous-groupe du Pd, ou PEGP (Rh, Pt et Pd), qui se comportent comme des éléments incompatibles, montrent plutôt une affinité pour les phases liquides (Barnes et Maier, 1999). Cette différence comportementale fait donc en sorte que les EGP subiront un fractionnement entre les IEGP et les PEGP lors des processus de fusion partielle et de cristallisation fractionnée. Bien que le Rh soit inclus dans le sous-groupe du Pd, il est de plus en plus admis que cet élément exhibe un comportement intermédiaire entre les IEGP et les PEGP lors des différents processus magmatiques (e.g., Brenan et al., 2012; Park et al., 2012).

1.2.2 LE FRACTIONNEMENT DES EGP

1.2.2.1 LA FUSION PARTIELLE

Lorsque le manteau supérieur est soumis au processus de fusion partielle, les EGP sont fractionnés entre le résidu mantellique et le liquide magmatique nouvellement formé. Ce fractionnement dépend majoritairement du taux de fusion partielle ainsi que des coefficients de partage des EGP entre les phases mantelliques et le liquide magmatique.

Des études basées sur l'analyse de xénolites suggèrent que le budget en EGP du manteau est essentiellement contrôlé par les sulfures (Mitchell et Keays, 1981; Handler et Bennett, 1999). En effet, les analyses effectuées par Handler et Bennett (1999) sur des péridotites du manteau démontrent que moins de 10% du budget en EGP est contrôlé par la spinelle, l'olivine et les autres silicates, tandis que plus de 90% du budget est contrôlé par les sulfures et possiblement par des phases plus réfractaires telles que des minéraux du groupe du platine (MGP).

Bien que les coefficients de partage des EGP entre les sulfures et le liquide silicaté n'ont toujours pas été déterminés avec précision ($D_{EGP}^{Sul/Sil} = 10^3$ à 10^6 ; Barnes et Maier, 1999; Barnes et Lightfoot, 2005; et les références qui y sont incluses), il est évident que les EGP préfèrent nettement rester dans les sulfures mantelliques résiduels durant le processus de fusion partielle. Keays (1995) suggère que le taux de fusion partielle requis pour dissoudre tous les sulfures du manteau (i.e., 0,07 à 0,11 % poids de sulfures pour 250 ± 50 ppm de S; McDonough et Sun, 1995) est d'environ 25%. Barnes et Maier (1999) ont

démontré que le ratio Pd/Ir du liquide magmatique évolue en faveur du Pd durant la dissolution des sulfures du manteau (< 25% de fusion partielle), et donc, que les liquides produits par un faible degré de fusion partielle tendent à s'enrichir en PEGP ($\text{Pd}/\text{Ir} > 1$), tandis que le manteau résiduel s'enrichit plutôt en IEGP ($\text{Pd}/\text{Ir} < 1$). Ainsi, lorsque le taux de fusion partielle est relativement faible, par exemple, lorsque des liquides basaltiques sont générés sous une dorsale océanique ou via l'ascension d'un panache mantellique (i.e., généralement < 10%), les sulfures contenus dans le manteau résiduel auront tendance à retenir les IEGP. Cela pourrait donc expliquer pourquoi le contenu en EGP des basaltes est extrêmement fractionné entre les IEGP et les PEGP ($\text{Pd}/\text{Ir} \sim 100$) comparativement aux roches issues d'une fusion partielle plus élevée telles que les komatiites ($\text{Pd}/\text{Ir} \sim 10$; Barnes et al., 1985).

Comme mentionné précédemment, les EGP ont la capacité de former des liaisons métalliques et sont donc susceptibles de se concentrer sous la forme d'alliages en raison de leur comportement sidérophile. Par conséquent, plusieurs auteurs suggèrent que les IEGP sont également présents dans le manteau sous la forme d'IMGP (minéraux d'IEGP) tels que des alliages d'Os-Ir et des sulfures de Ru-Os±Ir (Mitchell et Keays, 1981; Barnes et al., 1985; Handler et Bennett, 1999; Luguet et al., 2007). D'après les travaux réalisés par Luguet et al. (2007), les IMGP dominent le budget en EGP du résidu mantellique suite à la consommation complète des sulfures du manteau. Ainsi, lorsque le taux de fusion partielle est supérieur à 25%, par exemple, lorsque des liquides komatiitiques sont générés (~ 35 à 50% de fusion partielle; Arndt, 1977), le ratio Pd/Ir du liquide magmatique tend à évoluer en faveur de l'Ir en raison d'une plus grande extraction d'IEGP (Barnes et Maier, 1999).

1.2.2.2 LA CRISTALLISATION FRACTIONNÉE DES MAGMAS SATURÉS EN SULFURES

Plusieurs études réalisées sur des gisements à sulfures de Ni-Cu-EGP révèlent que la ségrégation d'un liquide sulfuré à partir du liquide silicaté exerce un grand pouvoir sur l'extraction des EGP et des autres éléments chalcophiles (e.g., Ag, Co, Cd, Cu, Ni, Sb, Sn et Zn; Barnes et Maier, 1999; Barnes et Lightfoot, 2005; Arndt et al., 2005). En effet, Barnes et Lightfoot (2005) ont démontré que les concentrations en EGP du liquide silicaté diminuent très rapidement lors de la ségrégation d'un liquide sulfuré. Le modèle proposé par ces auteurs suggère que l'extraction complète des EGP à partir d'un magma saturé en sulfures nécessite seulement de 2 à 5% du fractionnement des cristaux si les coefficients de partage des EGP entre le liquide sulfuré et le liquide silicaté sont respectivement de 40 000 et de 10 000.

D'après Barnes et Maier (1999), la différenciation du liquide sulfuré mène à un fractionnement entre les IEGP (+Rh) et le couple Pt-Pd qui s'exprime dans les gisements magmatiques sulfurés par la présence d'une portion riche en Fe et Ni, enrichie en IEGP et en Rh, ainsi que d'une portion riche en Cu, enrichie en Pt et en Pd. Ce fractionnement est causé par la cristallisation précoce de solution solide monosulfurée (MSS) dans laquelle le Fe peut être substitué par les IEGP et le Rh. Par conséquent, le liquide fractionné riche en Cu sera enrichi en éléments incompatibles dans les MSS tels que le Pt et le Pd, lesquelles auront tendance à se concentrer dans le liquide résiduel suite à la cristallisation de la solution solide intermédiaire (ISS).

1.2.2.3 LA CRISTALLISATION FRACTIONNÉE DES MAGMAS SOUS-SATURÉS EN SULFURES

Il a déjà été envisagé par Barnes et al. (1985) que le fractionnement des EGP dans les magmas sous-saturés en sulfures est essentiellement contrôlé par la cristallisation de MGP puisque que les silicates et les oxydes tels que l’olivine et la chromite ne conviennent pas à la substitution d’EGP en solution solide en raison du comportement naturellement sidérophiles de ces éléments. En revanche, les avancées technologiques en matière d’analyse ont récemment permis de démontrer que les IEGP et le Rh peuvent être faiblement compatibles dans l’olivine ($D_{IEGP-Rh}^{Ol/Liq} \sim 2$; Brenan et al., 2003, 2005), mais que le fractionnement des EGP dans les magmas sous-saturés en sulfures pourrait être davantage contrôlé par la chromite.

Basé sur des données roches totales et des résultats expérimentaux, il est aujourd’hui accepté que la chromite puisse être un minéral porteur d’EGP, et plus particulièrement d’IEGP. Les corrélations positives entre les concentrations roches totales en IEGP et en Cr observées à partir de nombreuses séquences mafiques et ultramafiques pauvres en sulfures ont mené plusieurs chercheurs à proposer que la chromite joue un rôle important en ce qui a trait au contrôle et au fractionnement des IEGP durant la cristallisation fractionnée (e.g., Barnes et Maier, 1999; Righter et al., 2004; Finnigan et al., 2008; Pagé et al., 2012; Brenan et al., 2012; Park et al., 2012). De plus, la présence d’enrichissements notable en IEGP dans les roches plutoniques riches en chromites, tels que les chromitites associées aux intrusions litées et aux complexes ophiolitiques,

supportent fortement l'hypothèse selon laquelle il existe un lien génétique entre la chromite et les concentrations roches totales en IEGP dans les magmas sous-saturés en sulfures (e.g., Agiorgitis et Wolf, 1978; Oshin et Crocket, 1982; Barnes et al., 1985; Pagé et al., 2012).

De manière générale, deux possibilités ont été proposées pour expliquer l'association entre la chromite et les concentrations roches totales en IEGP : (1) les IEGP sont des éléments peu solubles (ou insolubles) qui co-cristallisent avec la chromite sous la forme d'IMGP, et; (2) les IEGP sont des éléments solubles qui peuvent entrer en solution solide dans la structure de la chromite (Pagé et al., 2012 et références incluses). La première hypothèse est principalement basée sur la présence d'inclusions d'IMGP de taille micrométrique dans les chromites. Plusieurs études réalisées à partir de roches plutoniques riches en chromites révèlent que la laurite (RuS_2) et certains alliages d'Os-Ir-Ru sont les IMGP les plus communément observés en association avec la chromite (Talkington et Lipin, 1986; Prichard et al., 2008; Gonzalez-Jiménez et al., 2009). Dans les roches volcaniques, les évidences prouvant la présence d'inclusions d'IMGP dans les chromites sont essentiellement restreintes à l'observation de pics dans les spectres des IEGP obtenus à l'aide d'analyses *in situ* par ablation laser couplée à un spectromètre de masse (LA-ICP-MS, *laser ablation-inductively coupled plasma-mass spectrometry*). Les résultats obtenus à partir de ce type d'analyse suggèrent principalement la présence d'alliage d'Os-Ir ($\pm\text{Ru}$; Fiorentini et al., 2004; Locmelis et al., 2011).

De nos jours, l'origine des inclusions d'IMGP dans les chromites est toujours un sujet de débat. Gijbels et al. (1974) et Capobianco et al. (1994) ont tout d'abord proposé

une origine postérieure à la cristallisation du spinelle (i.e., chromite et Cr-spinelle, respectivement), suggérant que les IMGP sont formés par exsolution des IEGP contenus en solution solide dans les spinelles durant le refroidissement lent du magma. Plus récemment, Finnigan et al. (2008) ont démontré expérimentalement que la cristallisation de la chromite ou la rééquilibration de celle-ci avec le liquide magmatique environnant peut déclencher la précipitation d'IMGP à l'interface chromite-liquide. Ceux-ci suggèrent que l'incorporation préférentielle de Cr^{3+} et de Fe^{3+} par rapport aux espèces divalentes est responsable de la création d'une zone réductrice à l'interface chromite-liquide qui provoque une diminution de la solubilité des IEGP (+Rh), et plus particulièrement de l'Os et du Ru. Par conséquent, même si le magma hôte est sous-saturé en IMGP, le changement de solubilité ces éléments, en réponse à une réduction locale de la fugacité d'oxygène ($f\text{O}_2$) et à une diminution globale de la température, déclenchera la formation de particules d'IMGP à la marge des cristaux de chromite. Durant la croissance des cristaux, ces particules pourront ensuite être incorporées dans la chromite sous la forme d'inclusions micrométriques.

L'hypothèse selon laquelle les IEGP sont incorporés en solution solide dans la chromite a tout d'abord été supportée par des travaux expérimentaux. Bien que certaines expériences aient été menées dans des conditions qui ne correspondent pas à celles observées sur Terre, ces travaux suggèrent que les coefficients de partage des IEGP entre la chromite et liquide silicaté sont fortement influencés par la $f\text{O}_2$ (Righter et al., 2004; Brenan et al., 2012). Brenan et al. (2012) ont démontré que les IEGP, et par extension le Rh, se substituent préférentiellement au Fe^{2+} et au Fe^{3+} disponible dans les sites octaédriques du spinelle. Ainsi, ces auteurs suggèrent qu'une augmentation de la $f\text{O}_2$, et par

conséquent, du degré d'inversion du spinelle favorise l'incorporation des IEGP et du Rh dans la chromite, et ce, puisque le Fe²⁺ et le Fe³⁺ sont davantage disponibles dans les sites octaédriques lorsque le degré d'inversion augmente.

Récemment, il a été démontré à partir d'analyses *in situ* par LA-ICP-MS que les chromites de roches volcaniques contiennent des concentrations uniformes en IEGP et en Rh, supportant également que ces éléments sont présents en solution solide dans la structure de la chromite (Locmelis et al., 2011; Park et al., 2012; Pagé et al., 2012). Ces analyses ont détecté des concentrations relativement élevées pouvant atteindre jusqu'à 82 ppb d'Os, 202 ppb d'Ir, 540 ppb de Ru, et 151 ppb de Rh. Les coefficients de partage empiriquement déterminés par Pagé et al. (2012) pour l'Os, l'Ir et le Ru entre la chromite et un liquide komatiitique sous-saturé en sulfures (komatiite d'Alexo : $D_{Os}^{Chr/Kom} = 8,3$, $D_{Ir}^{Chr/Kom} = 9,5$ et $D_{Ru}^{Chr/Kom} = 79$) démontrent que les IEGP, et plus particulièrement le Ru, sont compatibles dans la chromite. Puisque les komatiites investiguées par Pagé et al. (2012) ne sont pas reconnues pour être particulièrement oxydées ($fO_2 = QFM - 1,5$ à $-0,5$; Canil, 1997), ceux-ci suggèrent que la température pourrait également être un paramètre critique pour l'incorporation de ces éléments en solution solide dans la chromite.

Borisov et Palme (2000) ont démontré que la solubilité du Ru augmente plus rapidement avec la température que la solubilité de l'Ir. Il est donc possible que dans un liquide à haute température (e.g., picritique ou komatiitique), le Ru, contrairement à l'Os et l'Ir, soit plus soluble et ne cristallise pas sous la forme d'IMGP durant les premières phases du refroidissement, mais serait davantage disponible pour entrer en solution solide dans la

structure de la chromite (Barnes et Fiorentini, 2008). D'après Pagé et al. (2012), cette hypothèse pourrait justifier le fait que les chromites des komatiites d'Alexo peuvent contrôler jusqu'à 100% du budget roche totale en Ru, mais moins de 20% du budget roche totale en Os et en Ir.

1.3 PROBLÉMATIQUE

Il est bien connu par ceux qui portent un intérêt particulier aux comportements adoptés par les EGP lors des processus magmatiques qu'il existe une compétition entre les sulfures et la chromite pour le contrôle et le fractionnement des EGP lors de la cristallisation fractionnée. Comme il a été vu précédemment, lorsque le magma est saturé en sulfures, les EGP et les autres éléments chalcophiles vont entrer préférentiellement dans le liquide sulfuré, et ce, de façon à appauvrir rapidement le liquide silicaté en ces éléments. Par ailleurs, des études ont récemment démontré que les IEGP et le Rh sont compatibles dans la chromite lorsque le magma est sous-saturé en sulfures, et que celle-ci pourrait alors jouer un rôle pour le fractionnement de ces éléments. Cependant, puisque cette dernière hypothèse est principalement basée sur l'observation de corrélations positives entre les concentrations roches totales en IEGP et en Cr, et que celles-ci pourraient tout aussi bien résulter du fait que la cristallisation de la chromite est potentiellement à l'origine de la formation d'IMGP, il semble que le rôle exercé par la chromite sur le fractionnement des IEGP, et par extension du Rh, soit toujours énigmatique. Par conséquent, il est possible de s'interroger

sur le rôle réel que joue la chromite sur le fractionnement de ces éléments dans les magmas mafiques et ultramafiques sous-saturés en sulfures.

1.3.1 LES HYPOTHÈSES

D'après les possibilités proposées pour le lien génétique entre la chromite et les IEGP dans les magmas sous-saturés en sulfures, trois alternatives peuvent être envisagées afin d'expliquer les corrélations positives entre les concentrations roches totales en IEGP et en Cr, et ainsi démystifier l'effet de la chromite sur le fractionnement des IEGP et du Rh lors du processus de cristallisation fractionnée :

- 1) La chromite contrôle le fractionnement des IEGP et du Rh puisque ceux-ci peuvent entrer en solution solide dans la chromite (Fig. 1.1a).
- 2) Les MGP contrôlent le fractionnement des IEGP et du Rh puisque la cristallisation de la chromite pourrait être à l'origine de la formation de ces minéraux tel que proposé par Finnigan et al. (2008) pour expliquer la présence d'IMGP en inclusion dans la chromite (Fig. 1.1b).
- 3) La chromite et les MGP se partagent le contrôle du fractionnement des IEGP et du Rh pour les mêmes raisons évoquées dans les deux premières hypothèses (Fig. 1.1c).

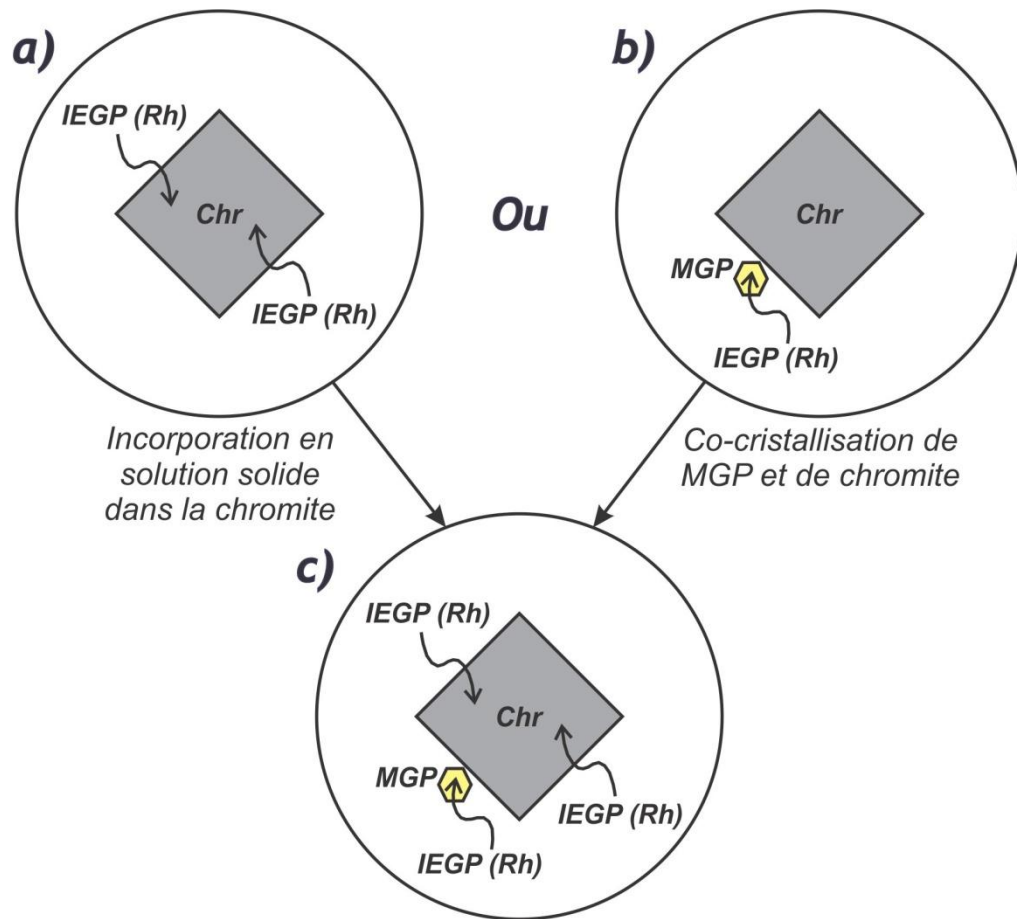


Figure 1.1 Représentation schématique des hypothèses envisageables pour expliquer l'association IEGP(Rh)-chromite : (a) incorporation des IEGP et du Rh en solution solide dans la chromite; (b) formation de MGP lors de la cristallisation de la chromite selon le modèle proposé par Finnigan et al. (2008), et; c) combinaison des deux premières hypothèses. Chr, chromite.

1.3.2 LES OBJECTIFS

L'objectif principal de ce projet de recherche est d'évaluer l'effet de la cristallisation de la chromite sur le fractionnement des IEGP et du Rh durant les premiers stades de la cristallisation fractionnée des magmas picritiques sous-saturés en sulfures de la Grande

Province Ignée d'Emeishan en Chine. Plusieurs objectifs secondaires ont également été fixés afin de complémer l'étude et de confirmer ou d'infirmer les hypothèses proposées dans la section précédente :

- 1) Déterminer si les chromites contiennent des concentrations uniformes en IEGP et en Rh.

Dans le cas advenant :

- Déterminer les coefficients de partage empiriques pour ces éléments dans la chromite.
- Évaluer la proportion des concentrations roches totales en ces éléments qui est contrôlée par la chromite.
- Clarifier les paramètres qui influencent l'incorporation de ces éléments en solution solide dans la chromite.

- 2) Déterminer si les chromites sont en relation avec des IMGP ou d'autres minéraux enrichis en EGP.

Dans le cas advenant :

- Identifier ces minéraux.
- Caractériser leur relation avec la chromite.
- Déterminer leur origine.

- 3) Déterminer si l'olivine peut également jouer un rôle en ce qui a trait au contrôle et au fractionnement des IEGP et du Rh dans les magmas picritiques sous-saturés en sulfures.

1.4 TERRAIN D'ÉTUDE

Cette section est consacrée à la présentation du contexte géologique. Elle consiste à exposer les caractéristiques majeures du terrain investigué ainsi que des roches principalement étudiées lors de ce projet de recherche. Des détails supplémentaires relatifs au contexte géologique sont fournis dans le manuscrit disponible au chapitre 2.

1.4.1 LA GRANDE PROVINCE IGNÉE D'EMEISHAN

La Grande Province Ignée d'Emeishan ou *Emeishan Large Igneous Province* (ELIP) est une province géologique de basaltes de plateau continental située à la marge ouest du Craton de Yangtze, au sud-ouest de la Chine (Fig. 1.2). Celle-ci s'étend sur plus de 250 000 km², pour un volume total d'environ 0.3×10^6 km³ (Ali et al., 2005). La plupart des datations radiométriques suggèrent que la ELIP se serait mise en place à environ 260 Ma (Liu et Zhu, 2009), ce qui correspond à la limite entre le Permien moyen et supérieur (i.e., fin du Guadalupien). Des évidences d'un soulèvement pré-volcanique ainsi que l'épanchement rapide de cet immense volume de magma (entre ~1 à 2 Ma selon Ali et al., 2005) indiquent fortement que la mise en place serait liée à l'ascension d'un panache mantellique (e.g., He et al., 2003; Ali et al., 2005; Campbell, 2007).

La ELIP est principalement constituée d'empilements volcaniques variant de 200 à plus de 5000 m en épaisseur (Shellnutt, 2013). Ces empilements sont majoritairement composés de basaltes tholéïitiques (> 95%), mais incluent également des roches

intermédiaires à felsiques (e.g., andésites basaltiques et ryholites) dans la partie supérieure des séquences, ainsi que des picrites à différents niveaux stratigraphiques (Chung et Jahn, 1995; Xu et al., 2001; Xiao et al., 2004; Shellnutt, 2013). En plus des roches volcaniques, la ELIP est également constituée d'une portion intrusive qui est essentiellement composée d'intrusions mafiques et ultramafiques, lesquelles sont principalement exposées au centre de la province (e.g., Zhou et al., 2008). Ces intrusions sont considérées comme étant d'importantes cibles d'exploration pour les chinois puisque certaines d'entre elles contiennent des gisements de Fe-Ti-V de classe mondiale (e.g., intrusion de Panzhihua), tandis que d'autres contiennent des dépôts économiques à sulfures de Ni-Cu-EGP (e.g., intrusions de Jinbaoshan, Limahe et Baimazhai).

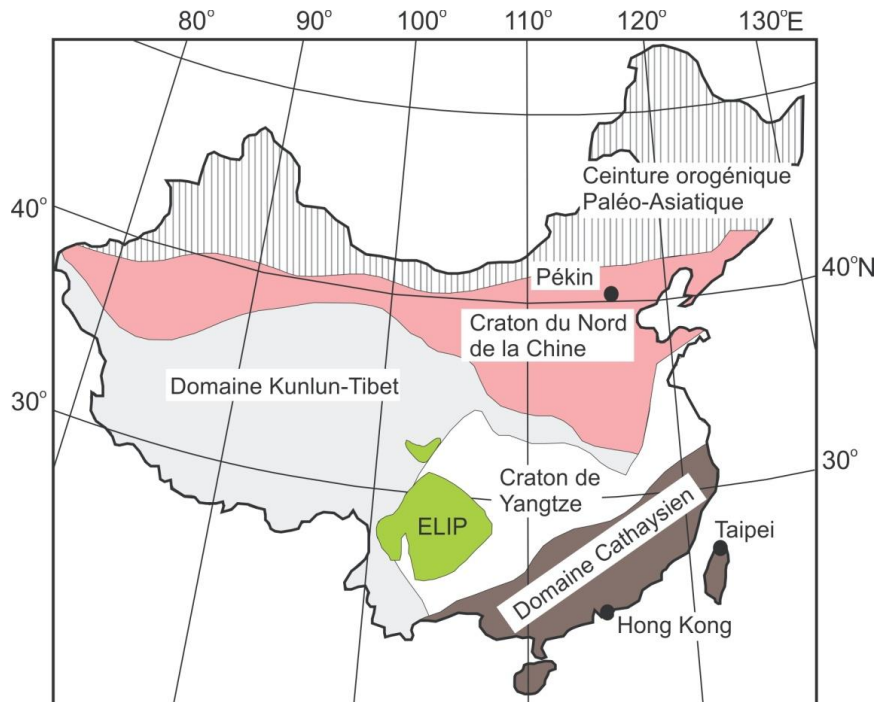


Figure 1.2 Carte des divisions tectoniques de la Chine montrant la localisation de la Grande Province Ignée d'Emeishan (ELIP; modifiée d'après Shellnutt, 2013).

1.4.2 LES PICRITES D'EMEISHAN

Le terme ‘picrite’ a traditionnellement été utilisé pour définir les roches extrusives dont la minéralogie est caractérisée par une abondance de phénocristaux d’olivine. Plus récemment, le terme ‘picrite’ a été utilisé pour définir les roches extrusives issues d’un liquide primitif qui contient entre 12 et 18% poids de MgO, entre 30 et 52% poids de SiO₂ et < 3% poids de Na₂O + K₂O (Le Bas, 2000). Kerr et Arndt (2001) suggèrent d’utiliser cette dernière définition uniquement pour les roches extrusives dépourvues de texture spinifex afin d’éviter de confondre les picrites avec les komatiites, puisque ces dernières sont minéralogiquement et chimiquement semblables à l’exception de leur contenu en MgO plus élevé (> 18% poids de MgO).

Au sein de la ELIP, les picrites sont principalement contenues dans les parties inférieures et intermédiaires des séquences volcaniques et peuvent atteindre plusieurs dizaines de mètres en épaisseur (e.g., Xu et al., 2001; Xiao et al., 2004). La minéralogie des picrites d’Emeishan est principalement caractérisée par la présence de phénocristaux automorphes à subautomorphes d’olivine (~15 à 20% volumique), et occasionnellement de diopside. La portion matricielle est essentiellement constituée de microlites de clinopyroxène, de plagioclase et d’oxydes de Fe-Ti (Zhang et al., 2005, 2006; Kamenetsky et al., 2012; Bai et al., 2013). De la chromite est également présente en trace sous la forme de micro-phénocristaux automorphes à subautomorphes en inclusion dans l’olivine ou libre dans la matrice (Zhang et al., 2005, 2006; Kamentesky et al., 2012).

Les picrites d'Emeishan ont été considérées comme étant de bons candidats pour cette étude pour les raisons suivantes : (1) les picrites d'Emeishan contiennent une quantité considérable de chromite (Zhang et al., 2005, 2006; Kamenetsky et al., 2012); (2) il est généralement admis que leur composition représente celle des magmas parents des basaltes tholéïtiques ainsi que des intrusions porteuses de minéralisation (e.g., Chung et Jahn, 1995; Ali et al., 2005; Hanski et al., 2010; Zhou et al., 2013); (3) les picrites d'Emeishan ont été générés par un taux de fusion partielle relativement élevé ($> 15\%$ selon Bai et al., 2013), et par conséquent, leur contenu en IEGP en Rh est relativement élevé (Zhang et al., 2005; Li et al., 2012; Bai et al., 2013; Li et al., 2014).

1.5 MÉTHODOLOGIE

La section qui suit correspond à un résumé des méthodes utilisées afin de parvenir aux objectifs que nous nous étions préalablement fixés. Tous les détails concernant l'étude pétrographique ainsi que les procédures analytiques sont fournis dans le manuscrit présenté dans le second chapitre de ce mémoire.

1.5.1 ÉCHANTILLONNAGE

Une excursion d'une quinzaine de jours en Chine a été organisée dans le but de prélever une trentaine d'échantillons non minéralisés en sulfures, incluant des picrites ($n = 24$), des basaltes tholéïtiques ($n = 9$) et quelques roches subvolcaniques (ou hypabyssales) riches en

phénocristaux d'olivine ($n = 3$). Les échantillons ont été récoltés sur 5 sites d'échantillonnage situés à proximité des communautés de Dali, Binchuan, Jianchuan et Lijiang dans la province de Yunnan, et d'Ertan dans la province de Sichuan. L'accessibilité à ces sites d'échantillonnage nous a été grandement facilitée par nos collaborateurs chinois, le professeur Xie-Yan Song et le docteur Song-Yue Yu, du *State Key Laboratory of Ore Deposit Geochemistry* à Guiyang en Chine.

1.5.2 ÉTUDE PÉTROGRAPHIQUE

Tous les échantillons ont servi à la fabrication de lames minces polies afin d'effectuer une étude pétrographique détaillée au microscope. Cette étude inclus : (1) l'identification et la caractérisation des minéraux constituant les portions phénocristique et matricielle des échantillons; (2) la détermination des proportions modales de chaque espèce de phénocristaux et micro-phénocristaux; (3) la caractérisation des textures globales des échantillons, et; (4) la caractérisation des textures spécifiques aux chromites. Les lames minces de trois échantillons de picrites ont également fait l'objet d'une étude au microscope électronique à balayage (SEM, *scanning electron microscope*) afin de vérifier si des grains de MGP sont présents en association avec de la chromite. Les informations fournies par l'étude pétrographique ont été mises en relation avec les résultats géochimiques afin de faciliter l'interprétation de l'ensemble des données et ainsi parvenir à des conclusions formelles.

1.5.3 ÉTUDE GÉOCHIMIQUE

Tous les échantillons ont été soumis à une série d'analyses roches totales et minérales *in situ*. Les analyses roches totales incluent des analyses par fluorescence X (XRF, *X-Ray Fluorescence*) et ICP-MS afin de déterminer la composition en éléments majeurs et en éléments traces, respectivement, ainsi que des analyses par pyro-analyses au sulfure de Ni (*Ni-sulfide fire assay*) pour déterminer le contenu en EGP des échantillons. En ce qui concerne les analyses minérales, celles-ci incluent des analyses microsonde afin de déterminer la composition en éléments majeurs des minéraux tels que l'olivine et la chromite, ainsi que des analyses par LA-ICP-MS pour déterminer la composition en éléments traces des chromites. Les analyses *in situ* par LA-ICP-MS sont critiques pour ce type d'étude puisqu'elles permettent de déterminer la signature en IEGP et en Rh des chromites, mais également de détecter la présence d'inclusions enrichies en EGP. De plus, les données fournies par l'ensemble de ces analyses roches totales et minérales sont indispensable pour effectuer un calcul de bilan de masse et ainsi évaluer le contrôle exercé par la chromite sur le budget roche totale en IEGP et en Rh. Des analyses semi-quantitatives par EDS (*energy dispersive X-ray spectrometry*) ont également été planifiées afin d'évaluer la composition de micro-grains de MGP en association avec la chromite.

1.6 FORMAT DU MÉMOIRE

Ce mémoire de maîtrise en Sciences de la Terre est divisé en trois chapitres. Le premier chapitre (ci-présent) est dédié à la présentation du cadre d'étude et consiste principalement à une revue de la littérature résumant les différents concepts qui ont mené au développement de la problématique de ce projet de recherche, et ainsi, à la formulation d'hypothèses de travail et à l'organisation d'une méthodologie permettant de tester ces hypothèses. Le deuxième chapitre correspond à une publication scientifique rédigée en anglais et qui a récemment été soumise dans le journal scientifique *Journal of Petrology*. Intitulé *The effect of chromite crystallization on the fractionation of osmium, iridium, ruthenium and rhodium in picritic magmas: an example from the Emeishan Large Igneous Province, south-western China*, ce manuscrit représente le corps de ce mémoire et consiste principalement à présenter les points culminants de l'étude, incluant un survol des résultats descriptifs et analytiques ainsi que les interprétations et les conclusions qui en ont découlé. L'ensemble des données géochimiques recueillies lors de cette étude est disponible en annexe à la fin du mémoire. Finalement, le dernier chapitre est davantage consacré à la présentation d'une synthèse de l'étude et des conclusions générales qui en ont été tirées.

1.7 CONTRIBUTIONS DE L'AUTEUR ET DES COLLABORATEURS

- 1) Auteur : Jean-Philippe Arguin, étudiant à la maîtrise en Science de la Terre à l'Université du Québec à Chicoutimi (UQAC).

- L'auteur à contribuer à l'échantillonnage, à la réalisation de toutes les analyses *in situ* par LA-ICP-MS, à la collecte des données pétrographiques et géochimiques, ainsi qu'à l'interprétation des résultats descriptifs et analytiques. De plus, l'auteur a rédigé la totalité du mémoire ainsi que la publication scientifique qui y est incluse. Il est également le concepteur de toutes les figures présentées dans le mémoire.
- 2) 1^{er} collaborateur : Philippe Pagé, directeur du projet et professeur sous-octroi à l'UQAC.
- 3) 2^e collaborateur : Sarah-Jane Barnes, co-directrice du projet, professeur à l'UQAC et titulaire de la Chaire de Recherche du Canada en Métallogénie Magmatique.
- Les 1^{er} et 2^e collaborateurs ont tous deux contribué à la planification et la direction du projet ainsi qu'à la correction du manuscrit. Le 1^{er} collaborateur a également contribué à l'échantillonnage et à la réalisation d'une partie des analyses *in situ* par LA-ICP-MS. Certaines interprétations peuvent également lui être attribuées.
- 4) 3^e collaborateur : Song-Yue Yu, professeur sous-octroi à la *Institute of Geochemistry, Chinese Academy of Sciences* à Guiyang en Chine.
- 5) 4^e collaborateur : Xie-Yan Song, professeur à la *Institute of Geochemistry, Chinese Academy of Sciences* à Guiyang en Chine.
- Les 3^e et 4^e collaborateurs ont essentiellement contribué à l'accessibilité aux sites d'échantillonnage ainsi qu'à l'échantillonnage proprement dit.

1.8 RÉFÉRENCES

- Ali, J. R., Thompson, G. M., Zhou, M.-F. & Song, X., 2005. Emeishan large igneous province, SW China. *Lithos* 79, 475-489.
- Argiorgitis, G. & Wolf, R., 1978. Aspects of osmium, ruthenium and iridium contents in some Greek chromites. *Chemical Geology* 23, 267-272.
- Arndt, N. T., 1977. Thick, layered peridotite-gabbro lava flows in Munro Township, Ontario. *Canadian Journal of Earth Sciences* 14, 2620-2637.
- Arndt, N. T., Lesher, C. M., & Czamanske, G. K., 2005. Mantle-derived magmas and magmatic Ni-Cu-(PGE) deposits. *Economic Geology, 100th Anniversary volume*, 5-24.
- Bai, M., Zhong, H., Zhu, W., Bai, Z. & He, D., 2013. Platinum-Group Element Geochemical Characteristics of the Picrites and High-Ti Basalts in the Binchuan Area, Yunnan Province. *Acta Geologica Sinica* 87, 158-840.
- Barnes, S.-J., Naldrett, A. J. & Gorton, M. P., 1985. The origin of the fractionation of Platinum-Group Elements in terrestrial magmas. *Chemical Geology* 53, 303-323.
- Barnes, S.-J. & Maier, W. D., 1999. The fractionation of Ni, Cu and the noble metals in silicate and sulphide liquids. *Geological Association of Canada Short Course Notes* 13, 69-106.

- Barnes, S.-J. & Lightfoot, P. C., 2005. Formation of magmatic nickel sulfide deposits and processes affecting their copper and platinum group element contents. *Society of Economic Geologist 100th anniversary volume*, 179-213.
- Barnes, S. J. & Fiorentini, M. L., 2008. Iridium, ruthenium and rhodium in komatiite: Evidence for iridium alloy saturation. *Chemical Geology* 257, 44-58.
- Borisov, A. & Palme, H., 2000. Solubilities of noble metals in Fe-containing silicate melts as derived from experiments in Fe-free systems. *American Mineralogist* 85, 1665-1673.
- Brenan, J. M., McDounough, W. F. & Dalpé, C., 2003. Experimental constraints on the partitioning of rhenium and some platinum-group elements between olivine and silicate melt. *Earth and Planetary Science Letters* 212, 135-150.
- Brenan, J. M., McDonough, W. F. & Ash, R., 2005. An experimental study of the solubility and partitioning of iridium, osmium and gold between olivine and silicate melt. *Earth and Planetary Science Letters* 237, 855-872.
- Brenan, J. M., Finnigan, C. F., McDonough, W. F. & Homolova, V., 2012. Experimental constraints on the partitioning of Ru, Rh, Ir, Pt and Pd between chromite and silicate melt: The importance of ferric iron. *Chemical Geology* 302-303, 16-32.
- Campbell, I. H., 2007. Testing the plume theory. *Chemical Geology* 241, 153-176.

- Canil, D., 1997. Vanadium partitioning and the oxidation state of Archaean komatiite magmas. *Nature* 389, 842-845.
- Capobianco, C. J., Hervig, R. L. & Drake, M. J., 1994. Experiments on crystal/liquid partitioning of Ru, Rh and Pd for magnetite and hematite solid solutions crystallized from silicate melt. *Chemical Geology* 113, 23-43.
- Chou, C. L., 1978. Fractionation of siderophile elements in the Earth's upper mantle. *Proceedings Of The 9th Lunar And Planetary Science Conference*, 219-230.
- Chou, C. L., Show, D. M. & Crockett, J. H., 1983. Siderophile trace elements in the Earth's oceanic crust and upper mantle. *Journal of Geophysical Research* 88, A507-A518.
- Chung, S.-L. & Jahn, B.-m., 1995. Plume-lithosphere interaction in generation of the Emeishan flood basalts at the Permian-Triassic boundary. *Geology* 23, 889-892.
- Finnigan, C. S., Brenan, J. M., Mungall, J. E. & McDonough, W. F., 2008. Experiments and model bearing on the role of chromite as a collector of platinum group minerals by local reduction. *Journal of Petrology* 49, 1647-1665.
- Fiorentini, M. L., Stone, W. E., Beresford, S. W. & Barley, M. E., 2004. Platinum-group element alloy inclusions in chromites from Archaean mafic-ultramafic units: evidence from the Abitibi and the Agnew-Wiluna Greenstone Belts. *Mineralogy and Petrology* 82, 341-355.

- Gijbels, R. H., Millard, H. T., Desborough, G. A. & Bartel, A. J., 1974. Osmium, ruthenium, iridium and uranium in silicates and chromite from the eastern Bushveld Complex, South Africa. *Geochimica et Cosmochimica Acta* 38, 319-337.
- Goldschmidt, V.M., (1937) The principles of distribution of chemical elements in minerals and rocks. *Journal of Chemical Society*, 655-673.
- Gonzalez-Jiménez, J. M., Gerville, F., Proenza, J. A., Augé, T. & Kerestedjian, T., 2009. Distribution of platinum-group minerals in ophiolitic chromitites. *Transactions of the Institution of Mining and Metallurgy, Section B (Applied Earth Sciences)* 118, 101-110.
- Handler, M. R. & Bennet, V. C., 1999. Behaviour of Platinum-group elements in the subcontinental mantle of eastern Australia during variable metasomatism and melt depletion. *Geochimica et Cosmochimica Acta* 63, 3597-3618.
- Hanski, E., Kamenetsky, V. S., Luo, Z.-Y., Xu, Y.-G. & Kuzmin, D. V., 2010. Primitive magmas in the Emeishan Large Igneous Province, southwestern China and northern Vietnam. *Lithos* 119, 75-90.
- He, B., Xu, Y.-G., Chung, S.-L., Xiao, L. & Wang, Y., 2003. Sedimentary evidence for a rapid, kilometer-scale crustal doming prior to the eruption of the Emeishan flood basalts. *Earth and Planetary Science Letters* 213, 391-405.

- Kamenetsky, V. S., Chung, S.-L., Kamenetsky, M. B. & Kuzmin, D. V., 2012. Picrites from the Emeishan Large Igneous Province, SW China: a Compositional Continuum in Primitive Magmas and their Respective Mantle Sources. *Journal of Petrology* 53, 2095-2113.
- Keays, R. R., 1995. The role of komatiitic and picritic magmatism and S-saturation in the formation of ore deposits. *Lithos* 34, 1-18.
- Kerr, A. C. & Arndt, N. T., 2001. A Note on the IUGS Reclassification of the High-Mg and Picritic Volcanic Rocks. *Journal of Petrology* 42, 2169-2171.
- Kimura, K., Lewis, R. S. & Anders, E., 1974. Distribution of gold and rhenium between nickel-iron and silicate melts: implications for the abundances of siderophile elements on the Earth and Moon. *Geochimica et Cosmochimica Acta* 38, 683-701.
- Le Bas, M. J., 2000. IUGS Reclassification of the High-Mg and Picritic Volcanic Rock. *Journal of Petrology* 41, 1467-1470.
- Li, C., Tao, Y., Qi, L. & Ripley, E. M., 2012. Controls on PGE fractionation in the Emeishan picrites and basalts: Constraints from integrated lithophile-siderophile elements and Sr-Nd isotopes. *Geochimica et Cosmochimica Acta* 90, 12-32.
- Li, J., Wang, X.-C., Ren, Z.-Y., Xu, J.-F., He, B. & Xu, Y.-G., 2014. Chemical heterogeneity of the Emeishan mantle plume: evidence from highly siderophile element abundances in picrites. *Journal of Asian Earth Sciences* 79, 191-205.

- Liu, C. & Zhu, R., 2009. Geodynamic Significances of the Emeishan Basalts. *Earth Science Frontiers* 16, 52-69.
- Locmelis, M., Pearson, N. J., Barnes, S. J. & Fiorentini, M. L., 2011. Ruthenium in komatiitic chromite. *Geochimica et Cosmochimica Acta* 75, 3645-3661.
- Luguet, A., Shirey, S. B., Lorand, J.-P., Horan, M. F. & Carlson, R. W., 2007. Residual platinum-group minerals from highly depleted harzburgites of the Lherz massif (France) and their role in HSE fractionation of the mantle. *Geochimica et Cosmochimica Acta* 71, 3082-3097.
- Mitchell, R. H. & Keays, R. R., 1981. Abundance and distribution of gold, palladium and iridium in some spinel and garnet lherzolites: implications for the nature and origin of precious metal-rich intergranular components in the upper mantle. *Geochimica et Cosmochimica Acta* 45, 2425-2442.
- McDonough, W. F. & Sun, S.-S., 1995. The composition of the Earth. *Chemical Geology* 120, 223-253.
- Morgan, J. W., 1986. Ultramafic xenoliths: clues to Earth's late accretionary history. *Journal of Geophysical research* 91, 12375-12387.
- Oshin, I. O. & Crocket, J. H., 1982. Noble metals in Thetford Mines ophiolites, Quebec, Canada. Park I: distribution of gold, iridium, platinum, and palladium in the ultramafic and gabbroic rocks. *Economic Geology* 77, 1556-1570.

- Pagé, P., Barnes, S.-J., Bédard, J. H. & Zientek, M. L., 2012. In situ determination of Os, Ir and Ru in chromites formed from komatiite, tholeiite and boninite magmas: Implications for chromite control of Os, Ir and Ru during partial melting and crystal fractionation. *Chemical Geology* 302-303, 1-15.
- Park, J.-W., Campbell, I. H. & Eggins, S. M., 2012. Enrichment of Rh, Ru, Ir and Os in Cr spinels from oxidized magmas: Evidence from the Ambae volcano, Vanuatu. *Geochimica et Cosmochimica Acta* 78, 28-50.
- Prichard, H. M., Neary, C. R., Fisher, P. C. & O'Hara, M. J., 2008. PGE-rich podiform chromitites in the Al'Ays ophiolite complex, Saudi Arabia: an example of critical mantle melting to extract and concentrate PGE. *Economic Geology* 103, 1507-1529.
- Righter, K., Campbell, A. J., Humayun, M. & Hervig, R. L., 2004. Partitioning of Ru, Rh, Pd, Re, Ir and Au between Cr-bearing spinel, olivine, pyroxene and silicate melts. *Geochimica et Cosmochimica Acta* 68, 867-880.
- Shellnutt, J. G., 2013. The Emeishan large igneous province: a synthesis. *Geoscience Frontiers* 5, 369-394.
- Sun, S.-S., Wallace, D. A., Hoatson, D. M., Glikson, A. Y. & Keays, R. R., 1991. Use of geochemistry as a guide to platinum group element potential of mafic ultramafic rocks: examples from the west Pilbara Block and Halls Creek mobile zone, Western Australia. *Precambrian Research* 50, 1-35.

- Talkington, R. W. & Lipin, B. R., 1986. Platinum-group minerals in chromite seams of the Stillwater Complex, Montana. *Economic Geology* 81, 1179-1186.
- Xiao, L., Xu, Y. G., Mei, H. J., Zheng, Y. F., He, B. & Pirajno, F., 2004. Distinct mantle sources of low-Ti and high-Ti basalts from the western Emeishan large igneous province, SW China: implications for plume-lithosphere interaction. *Earth and Planetary Science Letters* 228, 525-546.
- Xu, Y., Chung, S.-L., Jahn, B.-m. & Wu, G., 2001. Petrologic and geochemical constraints on the petrogenesis of Permian-Triassic Emeishan flood basalts in southwestern China. *Lithos* 58, 145-168.
- Zhang, Z. C., Mao, J., Mahoney, J. J., Wang, F. & Qu, W., 2005. Platinum group elements in the Emeishan large igneous province, SW China: Implications for mantle sources. *Geochemical Journal* 39, 371-382.
- Zhang, Z. C., Mahoney, J. J., Mao, J. W. & Wang, F. S., 2006. Geochemistry of picritic and associated basalt flows of the Western Emeishan flood basalt province. *Journal of Petrology* 47, 1997-2019.
- Zhou, M.-F., Arndt, N. T., Malpas, J., Wang, C. Y. & Kennedy, A. K., 2008. Two magma series and associated ore deposit types in the Permian Emeishan large igneous province. *Lithos* 103, 352-368.

Zhou, M.-F., Chen, W. T., Wang, C. Y., Prevec, S. A., Liu, P. P. & Howarth, G. H., 2013. Two stages of immiscible liquid separation in the formation of Panzhihua-type Fe-Ti-V oxide deposits, SW China. *Geoscience Frontiers* 4, 481-502.

CHAPITRE 2

THE EFFECT OF CHROMITE CRYSTALLIZATION ON THE FRACTIONATION OF OSMIUM, IRIDIUM, RUTHENIUM AND RHODIUM IN PICRITIC MAGMAS: AN EXAMPLE FROM THE EMEISHAN LARGE IGNEOUS PROVINCE, SOUTH-WESTERN CHINA

Arguin, Jean-Philippe ^{1,*}, Pagé, Philippe ¹, Barnes, Sarah-Jane ¹, Yu, Song-Yue ², Song, Xie-Yan ²

¹ Université du Québec à Chicoutimi; Canada Research Chair in Magmatic Ore Deposits, Chicoutimi, G7H 2B1, Canada.

² State Key Laboratory of Ore Deposit Geochemistry; Institute of Geochemistry, Chinese Academy of Sciences, Guiyang, Guizhou 550002, China.

JOURNAL OF PETROLOGY, SUBMITTED APRIL, 2015

2.1 ABSTRACT

Because chromite-rich cumulates from plutonic settings tend to be enriched in Os, Ir and Ru (referred to collectively as iridium-like platinum-group elements (IPGE)), and whole-rock Cr positively correlates with IPGE in numerous sulphide-poor mafic to ultramafic sequences, it appears that chromites play an important role in the fractionation of IPGE, and by extension Rh, during crystal fractionation of sulphide-undersaturated magmas. However, it is not clear if the fractionation is controlled by the partitioning of IPGE and Rh into the chromite or by the crystallization of IPGE–Rh-rich minerals together with chromite. Furthermore, because MgO positively correlates with Cr, as well as with IPGE, it appears that olivine may also play a role in the fractionation of IPGE.

In order to investigate the effect of chromite crystallization on the fractionation of IPGE and Rh in sulphide-undersaturated picritic magmas, we report *in situ* laser ablation inductively coupled plasma mass spectrometry (LA-ICP-MS) analyses of IPGE and Rh abundances in chromites from the Emeishan Large Igneous Province in south-western China. The time-resolved analysis signals for IPGE and Rh in chromites are generally constant, indicating that these elements are found homogeneously distributed in the chromite structure. Median Os, Ir, Ru and Rh concentrations are 30, 23, 248 and 21 ppb, respectively. Rhodium enrichment in chromite seems to be promoted by the increase of the inversion degree of the chromite structure, and by extension, by the increase of the oxygen fugacity, as suggested by the positive correlation observed between $\text{Fe}^{3+}/(\text{Cr} + \text{Al} + \text{Fe}^{3+})$ and Rh in chromites, whereas Os, Ir and Ru enrichments appear to be controlled by other

parameters such as a high temperature of the magmas, and/or a greater concentration of IPGE in the magmas. The empirical partition coefficients between chromites and picrites decrease in the following order: Ru (119) > Rh (43) with Ir and Os approximately equal (21 and 17, respectively). Despite the high IPGE and Rh concentrations in chromite, mass balance calculations show that the chromite does not account for all the IPGE and Rh, with a maximum of ~85% of the whole-rock Ru budget, ~50% of the Rh budget and less than 25% of the Os and Ir budgets. *In situ* LA-ICP-MS and scanning electron microscopy (SEM) analyses reveal the presence of micrometric-sized IPGE±Rh-rich minerals, such as laurite (RuS_2), Os–Ir±Ru alloys and Pt–Fe (\pm IPGE and Rh) alloys, in association with chromites. The presence of these minerals could explain the whole-rock IPGE and Rh proportion that is not accounted for by the chromite. However, assuming that IPGE and Rh may be moderately compatible with olivine, this phase could also be considered due to a large amount of phenocrysts in the Emeishan picrites (up to ~50 vol. %).

Based on numerical modelling, we conclude that chromite, olivine and platinum-group minerals all play a role in the fractionation of IPGE and Rh during the early stages of crystal fractionation of picritic magmas. Furthermore, we establish that the preferential incorporation of Ru into the chromite structure is responsible for the Ru anomalies observed in platinum-group element patterns of the Emeishan basalts. On the other hand, the relative importance of olivine and PGM in controlling IPGE and Rh remains uncertain and is a key subject for further investigations.

Key words: chromite; Emeishan; picrites; platinum-group elements

2.2 INTRODUCTION

Those who have studied the behaviour of platinum-group elements (PGE) in magmatic systems consider that Os, Ir and Ru (the iridium-like platinum-group elements (IPGE)) behave as compatible elements, and that Rh, Pt and Pd (the palladium-like platinum-group elements (PPGE)) behave as incompatible elements during partial melting and crystal fractionation of sulphide-undersaturated magmas (e.g. Barnes *et al.*, 1985; Crocket, 2002; Mungall, 2005). More recently, it appears that Rh shows an intermediate behaviour between these two extremes. Based on whole-rock data from both volcanic and plutonic suites from a variety of geological settings, it has been suggested that chromite could be an important host mineral for IPGE when it crystallizes from sulphide-undersaturated magmas. Indeed, the positive correlations observed between whole-rock IPGE and Cr for many sulphide-poor mafic to ultramafic sequences have led many researchers to propose that chromite plays a role in the fractionation of IPGE during crystal fractionation (e.g. Barnes & Maier, 1999; Puchtel & Humayun, 2001; Brenan *et al.*, 2003, 2005, 2012; Righter *et al.*, 2004; Finnigan *et al.*, 2008; Fiorentini *et al.*, 2008; Pagé *et al.*, 2012; Park *et al.*, 2012). In addition, the occurrence of IPGE enrichments in chromite-rich plutonic rocks, such as mantle podiform and crustal stratiform chromitites, also supports the genetic link between whole-rock IPGE and chromites (Agiorgitis & Wolf, 1978; Oshin & Crocket, 1982; Barnes *et al.*, 1985; Pagé *et al.*, 2012).

Two major possibilities have been considered to explain the IPGE–chromite association: (1) these elements could crystallize as IPGE-rich phases, such as iridium-like

platinum-group minerals (IPGM), together with chromite (e.g. Finnigan *et al.*, 2008); and (2) these elements could be incorporated in solid solution into the chromite structure (Pagé *et al.*, 2012 and references therein). The first possibility is mainly based on the presence of micrometric-sized IPGM grains found included in chromites from plutonic rocks. Chromite-hosted IPGM have been well documented from chromitites of layered intrusions and ophiolites, and the most common phases are those from the laurite (RuS_2)–erlichmanite (OsS_2) series followed by some IPGE alloys (e.g. Prichard *et al.*, 1981, 2008; Talkington *et al.*, 1983; Augé 1985, 1988; Talkington & Lipin, 1986; Gonzalez-Jiménez *et al.*, 2009; Barnes *et al.*, 2015). Based on the presence of peaks of Os–Ir (\pm Ru) observed from time-resolved PGE signals from *in situ* analyses by laser ablation inductively coupled plasma mass spectrometry (LA-ICP-MS) of chromites from komatiites, Fiorentini *et al.* (2004) and Locmelis *et al.* (2011) suggest that volcanic chromites can also contain micro-alloy inclusions. Furthermore, it has recently been demonstrated from *in situ* observations in scanning electron microscopy (SEM) that volcanic chromites can also host Pt–Fe alloys, which contain minor IPGE (Park *et al.*, 2012). Broadly speaking, two hypotheses have been advanced for the presence of micrometric-sized PGM inclusions in spinels: (1) PGM could result from post-crystallization exsolution of PGE, initially in solid solution, from chromite during slow cooling (Gijbels *et al.*, 1974; Capobianco *et al.*, 1994); and (2) PGE could be relatively insoluble in magmas (O'Neill *et al.*, 1995; Borisov & Palme, 2000) and crystallize as primary PGM grains, which could then be included into crystallizing chromite (e.g. Prichard *et al.*, 1981; Finnigan *et al.*, 2008).

Although the case for collection of IPGE and Rh by IPGM appears to be strong, there is also evidence for their incorporation in solid solution into the chromite structure. Early experimental work on partitioning of IPGE and Rh into spinel yielded very high partition coefficients (up to 530, 2300 and 22,000 for Rh, Ru and Ir, respectively) supporting the idea of IPGE and Rh partitioning into chromite (Capobianco & Drake, 1990; Capobianco *et al.*, 1994; Righter *et al.*, 2004). However, the composition of these spinels (Al or Fe-rich) and the very high oxygen fugacity ($f\text{O}_2$) under which these experiments were conducted (~QFM + 3 to + 8 (QFM = quartz-fayalite-magnetite buffer)) raised doubts about how applicable the results are to the crystallization of chromite. More recently, Brenan *et al.* (2012) performed experiments at lower $f\text{O}_2$ and spinel compositions corresponding to chromite, and found that IPGE and Rh do partition into chromite. Furthermore, *in situ* LA-ICP-MS analyses on chromites from volcanic rocks also support the partitioning of IPGE and Rh into chromite because these elements are homogeneously distributed within grains as shown on time-resolved signals (Locmelis *et al.*, 2011; Pagé *et al.*, 2012; Park *et al.*, 2012). Pagé *et al.* (2012) calculated that chromites from the Alexo komatiites in the Abitibi greenstone belt (Canada) control ~100% of the whole-rock Ru budget, but less than 20% of the whole-rock Os and Ir budgets. For this reason they concluded that IPGE must be partitioned between both chromite and IPGM, since Os and Ir require the presence of some other phase(s) to account for their mass balance.

Most of the above studies have not evaluated the role of olivine in collecting IPGE and Rh. The experiments performed by Brenan *et al.* (2003, 2005) show that IPGE and Rh are incompatible to slightly compatible with olivine. In the latter case and because olivine

generally co-crystallizes with chromite, it is possible that olivine may also play a role in controlling IPGE and Rh.

The three studies carried out so far using *in situ* LA-ICP-MS analyses on chromites from volcanic rocks were from two komatiitic sequences (Locmelis *et al.*, 2011; Pagé *et al.*, 2012) and one island arc (Park *et al.*, 2012). In order to expand the range of magma types and crystallization conditions that have been studied, we have performed laser ablation analyses on chromites from picrites and some other sulphide-poor mafic to ultramafic volcanic rocks from the Emeishan Large Igneous Province (ELIP) in south-western China. Furthermore, we report new whole-rock and primary mineral compositions for the Emeishan volcanic rocks; these include samples from two magmatic series (the high- and low-Ti). Our results from time-resolved analyses show that chromite microphenocrysts are markedly enriched in IPGE and Rh relative to the whole rock and that the uniformity of the signals indicates that these elements substitute into the chromite structure. Despite the high IPGE and Rh concentrations in chromites, mass balance calculations show that the chromite does not account for all of the whole-rock IPGE and Rh budgets, which require the presence of some other phase(s), such as olivine and PGM, to account for their mass balance. After having conducted numerical modelling of IPGE and Rh distribution we conclude that chromite, olivine and PGM all contribute to the fractionation of these elements during crystal fractionation of sulphide-undersaturated magmas from the Emeishan system. Furthermore, we conclude that the crystallization of chromite is responsible for Ru anomalies observed in the Ni–Cu–PGE patterns of the flood basalts. On the other hand, the

relative importance of olivine and PGM in controlling IPGE and Rh remains to be established.

2.3 GEOLOGICAL BACKGROUND

The ELIP is a rhombic-shaped continental flood basalt province extending from the eastern margin of the Tibetan Plateau to the western margin of the Yangtze Block in south-western China and covering an area of $> 250,000 \text{ km}^2$ in the Yunnan, Sichuan and Guizhou Provinces, for a total volume of $0.3 \times 10^6 \text{ km}^3$ (Ali *et al.*, 2005). The ELIP is bordered in the north by the Longmenshan thrust fault (He *et al.*, 2003) and in the south by the sinistral Ailao Shan-Red River fault zone, which runs in the NW–SE direction from north-western Yunnan Province to northern Vietnam (Fig. 2.1; Hanski *et al.*, 2010; Kamenetsky *et al.*, 2012). As summarized by Liu & Zhu (2009), radiometric dating shows that the province was emplaced within a few million years (i.e. 1–2 Ma; Ali *et al.*, 2005) around 260 Ma, corresponding to the end-Guadalupian (Late Permian) mass extinction. Late Permian volcanic rocks correlating with those of the ELIP have been reported in the Jinping area in southern Yunnan Province close to the China–Vietnam border and in the Song Da Zone in northern Vietnam (Wang *et al.*, 2007; Hao *et al.*, 2008). According to Pearce & Mei (1988), correlative basalts also occur on the eastern Qiangtang Terrane in Tibet.

The Emeishan flood basalts are unconformably underlain by a thick sequence of limestones, the Maokou Formation (Middle Permian), and overlain by sedimentary rocks

from Late Permian in the east and west, and from Late Triassic or Jurassic in the central part (He *et al.*, 2003). The Maokou Formation limestones are thinner in the central part of the province and become progressively thicker towards the margins (He *et al.*, 2003). As proposed by He *et al.* (2003), this domal thinning could be explained by a kilometre-scale crustal uplift induced by the emplacement of a mantle plume at the base of the lithosphere, followed by partial erosion of the limestones prior to the eruption of the first Emeishan lavas. Consequently, evidence of crustal uplift prior to the volcanic activity combined with the relatively quick effusion of a large volume of magma is consistent with the initial stages of mantle-plume activity (e.g. Campbell & Griffiths, 1990; Campbell & Davies, 2006; Campbell, 2007).

The lava sequence ranges in thickness from 1000 to more than 5000 m in the western part of the ELIP, and from 200 to 2600 m in the eastern part (Shellnutt, 2013) and consists mostly of tholeiitic basalts which represent more than 95% of the magma volume (Xiao *et al.*, 2004; Hanski *et al.*, 2010). Other volcanic rocks include basaltic-andesites and rhyolites or trachytes in the upper part and picrites at various stratigraphic levels (Chung & Jahn, 1995; Xu *et al.*, 2001; Xiao *et al.*, 2004; Shellnutt, 2013). Picrites are essentially found in the western part of the ELIP (e.g. Dali, Binchuan, Jianchuan and Lijiang areas; Fig. 2.1; Song *et al.*, 2001; Xu *et al.*, 2001; Xiao *et al.*, 2004; Zhang *et al.*, 2005, 2006a; Hanski *et al.*, 2010), in the Panxi (Panzhihua-Xichang) region in the Ertan area (Song *et al.*, 2001; Xu *et al.*, 2001) and in the NW continuation of the Song Da Zone in the Jinping area (Wang *et al.*, 2007). The stratigraphy of the Binchuan lava section, which is more than 5000 m thick, and the Shiman and Daju sections close to the city of Lijiang, which are 800

m and 5500 m thick, respectively, is described in several recent papers (Xu *et al.*, 2001; Xiao *et al.*, 2004; Zhang *et al.*, 2005, 2006a, 2008). According to these descriptions, the Emeishan picritic flows are mainly observed in the lower and middle parts of the volcanic sequence and can reach several tens of metres in thickness.

In addition to the volcanic rocks, the ELIP also contains intrusive rocks including numerous mafic to ultramafic dikes and intrusions which are mainly exposed in the Panxi region due to several N–S-trending faults (Zhou *et al.*, 2008). Two main types of mineral deposits have been found in the intrusions related to the ELIP magmatic event: (1) Ni–Cu–(PGE) sulphide deposits; and (2) world-class Fe–Ti–V oxide deposits. The magmatic sulphide deposits are found mainly in small, primitive intrusions throughout the entire flood basalt province. They include Ni–Cu–(PGE) sulphide deposits hosted by mafic–ultramafic sills (e.g. Yangliuping: Song *et al.*, 2003, 2004, 2006), Ni–Cu sulphide deposits hosted by mafic–ultramafic intrusions (e.g. Limahe and Baimazhai: Wang & Zhou, 2006; Wang *et al.*, 2006; Tao *et al.*, 2008, 2010) and PGE mineralization within ultramafic rocks (e.g. Jinbaoshan: Wang *et al.*, 2005, 2008; Tao *et al.*, 2007). Conversely, the Fe–Ti–V oxide deposits occur in larger and more evolved intrusions which are mainly distributed in the Panxi region along major N–S-trending faults (e.g. Taihe, Xinjie, Baima, Hongge and Panzhihua: Zhou *et al.*, 2005, 2008, 2013; Zhong & Zhu, 2006).

Based mainly on their Ti/Y ratios, Xu *et al.* (2001) classified the tholeiitic basalts of the ELIP into two major magma series. The low-Ti basalts have $\text{Ti}/\text{Y} < 500$, whereas the high-Ti basalts have $\text{Ti}/\text{Y} > 500$. According to these authors, the occurrence of a thick

succession of low-Ti lavas in the lower half of the volcanic sequence in the western part of the province results from partial melting in the plume axis region and may record the main episode of the ELIP flood basalt emplacement. On the other hand, the occurrence of less abundant high-Ti lavas, overlying the low-Ti lavas, may imply a waning activity of the mantle plume (Xu *et al.*, 2001). Xu *et al.* (2001) also suggested that the dominance of high-Ti lavas in the eastern part of the province results from melting of the mantle at the plume periphery. In contrast to these authors, Zhou *et al.* (2013) proposed generalized models for the ELIP magmatism which suggest that the high-Ti lavas were formed from Fe-rich picritic magmas originating from a fertile, deep mantle source, whereas the low-Ti lavas were formed from picritic magmas originating from a shallower and more depleted mantle source. Moreover, they also maintain that the mafic–ultramafic intrusions that host the Fe–Ti–V oxide deposits were formed from high-Ti basalt whereas the Ni–Cu sulphide-bearing intrusions are genetically associated with the low-Ti magma series.

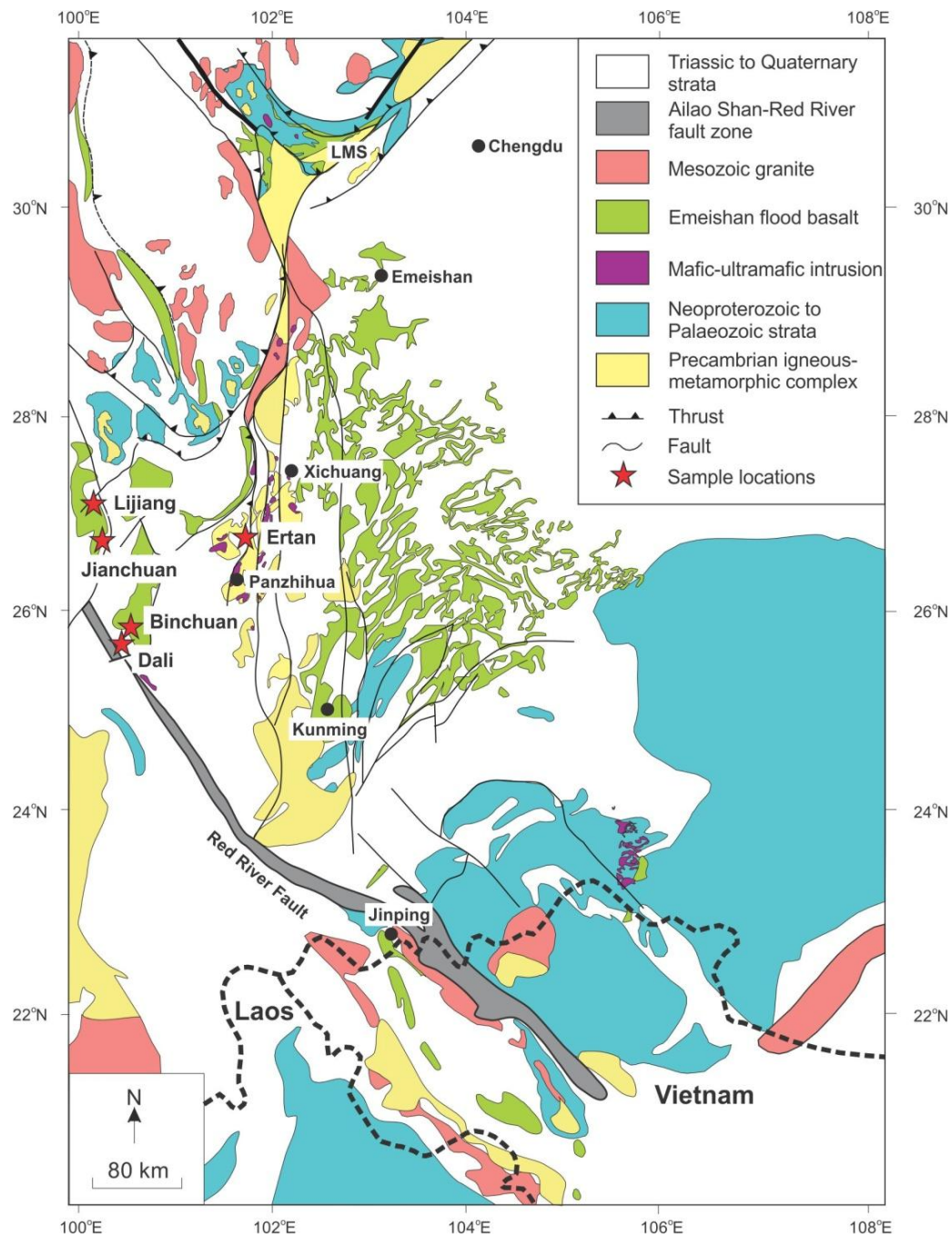


Figure 2.1 Schematic geological map showing the distribution of the flood basalt successions in the ELIP, south-western China (modified after Kamenetsky et al., 2012). Locations of picrites and other volcanic rocks reported in this study are indicated. LMS, Longmenshan thrust fault.

2.4 SAMPLE LOCATIONS AND ANALYTICAL METHODS

Samples of fresh to slightly weathered sulphide-poor picrites ($n = 24$) and flood basalts ($n = 9$) were collected mainly from road cuts in four locations in the western part of the ELIP in Yunnan Province: Dali, Binchuan, Jianchuan and Lijiang areas (from south to north; Fig. 2.1). Additional samples including olivine-phyric subvolcanic rocks (OPSV; $n = 3$) from the Ertan area, close to Panzhihua (Sichuan Province), were also considered in this study. In general, the outcrops where samples were collected are moderately to highly weathered due to a subtropical monsoon climate. Consequently, fresh samples were mainly obtained from preserved parts within these outcrops and thus a systematic sampling of the volcanic sequence was not possible. However, this does not interfere with the main objective of this study, which is to investigate whether IPGE and Rh partition into chromite, and if they do, to what extent chromite crystallization has influenced the fractionation of these elements in picritic magmas from the ELIP.

For whole-rock analyses, the samples were crushed in a steel jaw crusher and then pulverized in an alumina-ceramic shatterbox. Major and trace elements were determined by X-ray fluorescence (XRF) and ICP-MS methods, respectively, at Geoscience Laboratories (Geo Labs) in Sudbury, Canada. For trace elements, the powders were first dissolved in four acids in a closed vessel and then analysed. The whole-rock PGE were determined in the Laboratoire des Matériaux Terrestres (LabMaTer) at the Université du Québec à Chicoutimi by Ni-sulphide fire assay combined with Te co-precipitation followed by ICP-MS solution analysis (see Savard *et al.*, 2010). Reference materials were also analysed and

tests indicate that the three whole-rock analytical methods are accurate and precise (see Electronic Appendix 1). The whole-rock compositions recalculated to 100% anhydrous are given in Table 1.

Polished thin sections (30 µm thick) were made of each sample. These were examined with a petrographic microscope and chromite grains were selected for *in situ* analysis. The major elemental composition of chromite and other minerals was determined on a CAMECA SX100 microprobe with wavelength dispersive spectroscopy at the Université Laval in Québec City. The microprobe analytical conditions were 15 kV and 20 nA, with a beam size of 2 µm. Representative major element compositions of olivine, chromite and clinopyroxene as determined by microprobe are given in Table 2. Compositions of other minerals, including plagioclase and Fe–Ti oxides, and supplementary data for olivine, chromite and clinopyroxene are given in Electronic Appendix 2.

The trace element concentrations in chromite were determined by LA-ICP-MS in the LabMaTer. The LA-ICP-MS used is a Resonetics RESOlution M-50 Excimer using a 193 nm laser ablation microprobe and coupled with a Agilent 7700 Series ICP-MS. The laser was equipped with a double primary pump system and a Laurin Technic S-155 sample cell (large format cell). Ablated material was carried by a He–Ar gas mixture and analysed by ICP-MS operating in time-resolved mode using peak jumping. The analyses were conducted using a 6 mJ/pulse power, a frequency of 14 Hz and either a 73 µm or a 100 µm beam diameter. The gas blank was collected for 30 s followed by 30 s of laser ablation. The

following peaks were monitored : ^{25}Mg , ^{27}Al , ^{29}Si , ^{34}S , ^{43}Ca , ^{45}Sc , ^{47}Ti , ^{51}V , ^{53}Cr , ^{55}Mn , ^{57}Fe , ^{59}Co , ^{60}Ni , ^{63}Cu , ^{66}Zn , ^{69}Ga , ^{71}Ga , ^{74}Ge , ^{88}Sr , ^{95}Mo , ^{101}Ru , ^{102}Ru , ^{103}Rh , ^{105}Pd , ^{115}In , ^{118}Sn , ^{189}Os , ^{190}Os , ^{191}Ir , ^{192}Os , ^{193}Ir , ^{195}Pt and ^{197}Au .

We used ^{57}Fe from the ICP-MS combined with Fe from the microprobe analysis as the internal standard. All data were reduced using Iolite software by subtracting the gas blank from each of the analysed isotopes. Some inclusions were encountered during analysis and they were excluded from the time-resolved spectrum before calculating the average signal. Consequently, chromite ablation profiles having less than 5 s of signal were discarded from the study. In the absence of any matrix-match reference material, we used a synthetic Fe-sulphide (Laflamme-Po727) provided by Memorial University (Newfoundland, Canada) and doped with approximately 40 ppm of each PGE and Au to calibrate for the PGE and Au, as used by Barnes *et al.* (2008), Dare *et al.* (2010) and Pagé *et al.* (2012). In order to test the accuracy and the precision of the PGE calibration we also analysed a chromite monitor (AX37, chromites from the Alexo komatiite; see Electronic Appendix 3) as used by Pagé *et al.* (2012). The Ru concentrations have been corrected for Ni-argide interference on ^{101}Ru as: ^{101}Ru ppm – $(3.55886 \times 10^{-6} * \text{Ni ppm})$, and on ^{102}Ru as: ^{102}Ru ppm – $(6.06871 \times 10^{-6} * \text{Ni ppm})$. The ^{103}Rh and ^{105}Pd concentrations have been corrected for Cu-argide interference as: ^{103}Rh ppm – $(5.0 \times 10^{-5} * \text{Cu ppm})$ and ^{105}Pd ppm – $(1.64 \times 10^{-4} * \text{Cu ppm})$, respectively. Both Ru corrections were generally under 5% of the signal, whereas the averages of the ^{103}Rh and ^{105}Pd corrections were 14% and 167%, respectively. For this study, 223 laser ablation spots on chromites from the Emeishan samples were used. Osmium, Ir and Ru concentrations were determined by the average of a

number of different isotopes after correcting the Ni-argide interferences on Ru. Representative concentrations of Os, Ir, Ru and Rh in chromites and the detection limit for each of these elements are given in Table 3. Supplementary data are given in Electronic Appendix 4.

Table 1: Whole rock major oxide and trace element contents of the Emeishan picrites and basalts (recalculated to 100% anhydrous)

Location Rock type	<i>Daju</i>					<i>Shiman</i>			<i>Jianchuan</i>		
	<i>High-Ti picrites</i>										
Sample	13-DJ-03	13-DJ-04	13-DJ-05	13-DJ-06	13-DJ-08	13-DJ-09	13-SM-02	13-SM-03	13-JC-01	13-JC-02	13-JC-03
<i>Oxides (wt %)</i>											
SiO ₂	43.97	44.94	44.97	44.9	44.88	44.67	45.35	45.20	45.47	44.38	44.99
TiO ₂	1.21	1.78	1.76	1.76	1.72	1.34	1.48	1.39	1.82	1.37	1.20
Al ₂ O ₃	5.45	8.31	8.13	8.19	8.02	6.81	7.61	7.30	8.50	7.98	7.93
Fe ₂ O ₃ ^{Total}	12.78	12.71	12.69	12.77	12.69	12.31	13.68	12.73	13.16	12.86	12.20
MnO	0.17	0.18	0.18	0.18	0.18	0.17	0.23	0.19	0.18	0.19	0.18
MgO	30.45	21.43	21.99	21.65	22.36	24.67	23.32	23.85	20.60	23.35	23.99
CaO	5.79	8.74	8.65	8.79	8.33	9.42	7.61	8.55	8.74	8.42	8.14
Na ₂ O	0.02	0.98	0.81	0.88	0.97	0.37	0.40	0.49	1.07	0.84	0.82
K ₂ O	0.03	0.66	0.57	0.63	0.61	0.12	0.13	0.14	0.26	0.41	0.38
P ₂ O ₅	0.12	0.25	0.24	0.24	0.23	0.13	0.17	0.16	0.20	0.18	0.18
Total	99.99	99.98	99.99	99.99	99.99	100.01	99.98	100.00	100.00	99.98	100.01
LOI	8.79	3.90	4.82	4.19	3.63	4.50	6.76	5.91	3.13	3.76	4.62
<i>Trace elements (ppm)</i>											
Cr	2513	1922	1975	1936	2054	2332	2244	2012	1591	2311	2161
Cu	74	135	128	131	120	86	82	108	106	99	87
Ni	1625	957	975	963	968	1063	1160	1026	906	945	945
Ti/Y	621	623	617	607	621	557	581	572	559	488	493
Sm/Yb	3.26	3.41	3.34	3.46	3.44	3.02	2.87	2.90	3.12	2.80	2.84
<i>PGE (ppb)</i>											
Os	2.82	1.64	1.74	2.09	2.04	2.26	2.21	3.76	1.52	2.21	1.67
Ir	1.22	1.15	1.08	1.28	1.24	1.30	1.42	2.22	0.86	1.31	1.24
Ru	2.24	2.44	2.14	1.77	2.23	2.04	2.54	3.19	1.77	2.28	1.79
Rh	0.39	0.50	0.51	0.40	0.51	0.36	0.54	0.79	0.43	0.66	0.46
Pt	15.57	7.54	7.15	6.40	7.74	6.15	9.40	9.94	7.43	9.03	5.86
Pd	3.93	3.95	2.79	2.11	2.79	4.12	3.01	3.83	5.89	9.63	2.50
Pd/Ir	3.22	3.42	2.59	1.65	2.25	3.18	2.11	1.73	6.82	7.38	2.01
Σ PGE	6.27	5.23	4.95	5.14	5.51	5.60	6.17	9.17	4.16	5.80	4.70

Table 1: Continued

Location Rock type	<i>Jianchuan</i>				<i>Dali</i>				<i>Binchuan</i>		
	<i>High-Ti picrites</i>				<i>Low-Ti picrites</i>						
Sample	13-JC-04	13-JC-05	13-JC-06	13-JC-07	13-DL-02	13-DL-03	13-DL-04	13-DL-06	13-BC-02	13-BC-04	13-BC-05
<i>Oxides (wt %)</i>											
SiO ₂	45.57	46.90	45.65	45.57	45.41	45.51	50.41	45.38	44.52	44.20	44.46
TiO ₂	1.84	1.97	1.71	1.84	1.10	1.10	1.17	1.10	0.80	0.73	0.80
Al ₂ O ₃	8.58	9.72	8.37	8.58	10.09	9.86	10.14	9.93	8.67	8.03	8.67
Fe ₂ O ₃ ^{Total}	13.11	12.51	13.06	13.22	12.14	12.19	10.77	12.26	11.76	11.76	11.86
MnO	0.18	0.18	0.18	0.18	0.18	0.18	0.14	0.18	0.18	0.18	0.18
MgO	20.46	17.80	20.64	20.26	19.70	20.68	15.82	20.15	24.24	25.78	24.11
CaO	8.69	9.17	8.95	8.75	9.61	8.92	9.62	9.33	8.27	8.30	8.65
Na ₂ O	1.06	1.33	0.94	1.13	1.35	1.15	1.51	1.24	1.04	0.66	0.84
K ₂ O	0.30	0.23	0.32	0.27	0.28	0.25	0.24	0.27	0.33	0.19	0.27
P ₂ O ₅	0.20	0.20	0.17	0.20	0.16	0.16	0.17	0.16	0.18	0.16	0.18
Total	99.99	100.01	99.99	100.00	100.02	100.00	99.99	100.00	99.99	99.99	100.02
LOI	3.03	1.88	3.13	2.58	2.11	3.61	3.71	2.78	3.54	4.20	3.82
<i>Trace elements (ppm)</i>											
Cr	1581	1281	1598	1551	1747	1794	1775	1593	2110	2350	2159
Cu	119	131	98	125	124	121	139	123	95	84	102
Ni	898	775	907	891	933	964	996	920	1093	1149	1084
Ti/Y	567	553	575	569	374	375	363	375	312	316	317
Sm/Yb	3.18	3.12	3.13	3.24	1.70	1.71	1.76	1.72	2.40	2.37	2.32
<i>PGE (ppb)</i>											
Os	2.17	0.55	1.57	2.81	1.24	1.20	1.39	1.34	2.15	2.10	1.80
Ir	1.32	0.67	0.97	1.88	0.73	0.83	0.76	0.87	1.28	1.31	1.19
Ru	2.43	1.49	1.91	2.44	1.68	1.85	1.93	1.58	2.44	3.06	2.07
Rh	0.50	0.45	0.41	0.57	0.39	0.51	0.49	0.41	0.61	0.74	0.58
Pt	8.41	8.35	8.11	9.03	7.32	8.14	6.70	7.02	7.14	7.81	6.79
Pd	7.04	8.02	3.03	8.75	5.65	7.20	5.78	5.77	6.15	5.53	4.52
Pd/Ir	5.34	11.89	3.11	4.65	7.71	8.66	7.60	6.67	4.81	4.21	3.81
ΣPGE	5.92	2.71	4.45	7.13	3.66	3.88	4.08	3.78	5.87	6.48	5.06

Table 1: Continued

Location	<i>Binchuan</i>		<i>Ertan</i>		<i>Ertan</i>	<i>Daju</i>		<i>Shiman</i>		<i>Dali</i>	
Rock type	<i>Low-Ti picrites</i>		<i>OPSV</i>		<i>OPSV</i>	<i>Px-phyric basalts</i>				<i>Pl-phyric basalts</i>	
Sample	13-BC-06	13-BC-07	13-ET-02	13-ET-03	13-ET-04	13-DJ-01 ^a	13-DJ-07	13-DJ-10	13-SM-01	13-SM-04	13-DL-01 ^a
<i>Oxides (wt %)</i>											
SiO ₂	45.46	44.58	46.30	46.10	44.89	48.29	46.05	48.33	46.66	45.14	50.41
TiO ₂	0.96	0.78	2.05	2.02	1.05	2.31	2.17	1.97	2.15	2.39	2.54
Al ₂ O ₃	10.67	8.74	6.80	6.74	5.76	12.90	11.77	12.01	11.81	11.03	13.53
Fe ₂ O ₃ ^{Total}	11.92	11.73	13.38	13.33	13.05	12.08	13.14	12.75	12.39	13.10	14.70
MnO	0.18	0.18	0.18	0.17	0.18	0.18	0.22	0.18	0.42	0.25	0.18
MgO	18.87	24.55	21.86	22.22	26.59	9.97	11.15	10.22	9.80	9.94	3.57
CaO	9.71	8.17	7.50	7.42	7.81	9.55	11.94	10.23	14.12	15.66	7.67
Na ₂ O	1.24	0.88	0.73	0.78	0.43	3.72	2.31	2.63	1.99	1.74	5.08
K ₂ O	0.76	0.23	0.97	0.99	0.18	0.63	0.83	1.42	0.26	0.22	1.34
P ₂ O ₅	0.22	0.17	0.22	0.22	0.08	0.38	0.43	0.26	0.39	0.54	0.95
Total	99.99	100.01	99.99	99.99	100.02	100.01	100.01	100.00	99.99	100.01	99.97
LOI	2.99	4.09	3.87	3.34	4.17	2.95	2.87	2.53	2.07	2.20	1.24
<i>Trace elements (ppm)</i>											
Cr	1497	2222	2053	2047	2213	625	713	631	592	574	6
Cu	113	101	87	70	76	59	81	116	>2900	193	164
Ni	757	1096	1004	1034	1279	240	283	225	172	178	13
Ti/Y	308	301	732	721	588	572	568	507	630	700	355
Sm/Yb	2.34	2.47	6.06	6.03	3.24	2.82	2.77	2.71	2.71	3.11	2.16
<i>PGE (ppb)</i>											
Os	0.68	1.27	5.31	5.07	2.23	0.15	0.19	0.25	0.25	0.12	bdl
Ir	0.72	0.96	1.94	1.84	1.82	bdl	0.31	0.46	0.72	0.83	bdl
Ru	1.98	2.16	3.51	3.77	3.46	0.25	0.14	0.36	0.26	0.18	bdl
Rh	0.73	0.66	0.60	0.65	0.79	0.14	0.36	0.34	0.89	0.85	0.05
Pt	10.53	8.95	18.81	18.98	15.64	5.15	7.82	8.78	13.71	17.4	2.61
Pd	9.10	5.79	7.86	7.95	7.96	2.81	5.39	6.63	12.94	11.90	5.85
Pd/Ir	12.59	6.00	4.05	4.31	4.38		17.50	14.34	18.00	14.40	
Σ PGE	3.39	4.39	10.76	10.68	7.51	0.41	0.64	1.07	1.23	1.13	

Table 1: Continued

Location	<i>Dali</i>	<i>Binchuan</i>	<i>Daju</i>			
Rock type	<i>Pl-phyric basalts</i>			<i>Aphyric basalt</i>		
Sample	13-DL-05 ^a	13-BC-03	13-DJ-02	DL ^b	HT pm ^c	LT pm ^c
<i>Oxides (wt %)</i>						
SiO ₂	49.16	50.39	53.35	0.040	46.51	45.28
TiO ₂	3.42	3.66	2.19	0.010	1.88	0.91
Al ₂ O ₃	12.95	13.28	13.19	0.020	9.20	9.82
Fe ₂ O ₃ ^{Total}	16.20	15.53	11.25	0.010	13.53	12.41
MnO	0.28	0.14	0.11	0.002	0.19	0.21
MgO	4.63	3.25	5.93	0.010	18.22	21.00
CaO	9.34	6.98	7.09	0.006	9.83	9.37
Na ₂ O	2.62	5.94	5.92	0.020	1.04	1.18
K ₂ O	0.98	0.40	0.70	0.010	0.35	0.38
P ₂ O ₅	0.42	0.43	0.26	0.002	0.19	0.21
Total	100.00	100.00	99.99		100.94	100.75
LOI	0.72	1.74	1.50	0.050		
<i>Trace elements (ppm)</i>						
Cr	55	83	428	3.0		
Cu	342	254	75	1.4		
Ni	56	79	171	1.6		
Ti/Y	473	529	563			
Sm/Yb	2.44	3.14	2.80			
<i>PGE (ppb)</i>						
Os	0.03	0.08	0.21	0.065		
Ir	bdl	0.05	0.11	0.025		
Ru	bdl	0.19	0.21	0.120		
Rh	0.21	0.50	0.10	0.082		
Pt	4.62	8.67	3.08	0.084		
Pd	13.54	12.58	2.78	0.471		
Pd/Ir		245.02	25.18			
ΣPGE	0.03	0.32	0.53			

^a bdl, below detection limits.^b DL, detection limits; detection limits for PGE are from Savard et al. (2010).^c HT pm, high-Ti primitive melt; LT pm, low-Ti primitive melt; calculated to be in equilibrium with the olivine phenocrysts with the highest Fo content (91.1 mol. %, high-Ti and 92.9 mol. %, low-Ti picrites).

Table 2: Representative olivine, chromite and clinopyroxene microprobe analyses

Sample	13-DJ-03	13-SM-02	13-JC-03	13-BC-02	13-DL-02	13-DJ-09	13-BC-04	13-DJ-02	13-SM-02	13-JC-03	13-DL-03	13-BC-04
Series ^a	HT	HT	HT	LT	LT	HT	LT	HT	HT	LT	LT	LT
Mineral ^b	<i>Olivine phenocrysts</i>					<i>Olivine mp (or rims)</i>			<i>Chromite microphenocrysts</i>			
Grain #	Dj3a-O1	Sm2h-O1	Jc3c-O1	Bc2f-O1	Dl2c-O1	Dj9d-Om1	Bc4h-Om1	Dj2d-Cm2	Sm2e-Cm1	Jc3b-Cm1	Dl3c-Cm1	Bc4c-Cm1
SiO ₂ (wt %)	40.68	40.90	40.51	41.02	41.04	39.32	39.32	0.08	0.07	0.07	0.13	0.07
TiO ₂								1.77	1.80	1.43	0.56	0.56
Al ₂ O ₃	0.05	0.04	0.02	0.07	0.08	0.03	0.61	16.60	12.41	13.23	17.09	15.98
Cr ₂ O ₃	0.05		0.16	0.12	0.19		0.35	40.22	47.34	49.57	51.18	46.61
V ₂ O ₅							0.39	0.17	0.21	0.17	0.17	0.19
FeO ^{Total}	10.15	11.27	10.47	8.07	9.49	17.86	16.68	27.33	30.78	23.69	17.94	25.95
MnO	0.15	0.16	0.18	0.13	0.11	0.31	0.28	0.10	0.30			0.26
MgO	48.57	48.00	48.28	50.45	49.89	42.60	41.92	11.54	7.55	10.99	13.50	9.43
CaO	0.29	0.41	0.34	0.31	0.28	0.28	2.17					
Na ₂ O												
NiO	0.37	0.29	0.39	0.31	0.37	0.27	0.28	0.18	0.10	0.19	0.14	0.15
Total	100.31	101.07	100.35	100.48	101.45	100.67	101.61	98.21	100.52	99.38	100.71	99.20
FeO ^c								18.62	24.30	18.74	15.19	20.49
Fe ₂ O ₃ ^c								9.68	7.20	5.50	3.06	6.07
Fo (mol. %)	89.51	88.36	89.16	91.77	90.35	80.96	81.75					
Mg# ^d								53.15	35.90	51.52	61.89	45.41
Cr# ^e								61.91	71.91	71.54	66.76	66.18
Fe ³⁺ /R ^{3+, f}								0.13	0.10	0.07	0.04	0.08

Table 2: Continued

Sample Series ^a	13-DJ-04 HT	13-DJ-08 HT	13-SM-03 HT	13-JC-01 HT	13-ET-02 HT	13-DL-03 LT	13-DL-06 LT	13-BC-04 LT	13-BC-06 LT	13-DJ-10 HT	13-DL-02 LT	13-JC-01 HT
Mineral ^b	Chromite (olivine-hosted inclusions)										Diopside ph	Augite ph
Grain #	Dj4f-Ci1	Dj8a-Ci1	Sm3g-Ci1	Jc1a-Ci1	Et2b-Ci1	Dl3b-Ci1	Dl6a-Ci2	Bc4e-Ci1	Bc6c-Ci1	Dj10a-Cx1	Dl2a-Cx1	Jc1a-Cx1
SiO ₂ (wt %)	0.16	0.08	0.08	0.07	0.08	0.08	0.13	0.16	0.12	50.13	49.76	51.89
TiO ₂	1.93	1.47	2.03	1.62	2.38	0.91	0.54	0.59	0.61	0.87	0.81	0.64
Al ₂ O ₃	13.76	14.37	14.51	12.96	10.68	14.27	15.35	15.57	15.69	3.63	5.33	2.18
Cr ₂ O ₃	49.83	48.78	44.44	48.60	47.91	49.36	52.99	50.85	49.29	0.56	1.02	0.66
V ₂ O ₅	0.43	0.15	0.20	0.22	0.28	0.29	0.13	0.10	0.13			
FeO ^{Total}	22.44	21.9	27.57	23.91	28.44	24.37	13.21	18.70	21.36	5.38	5.55	4.98
MnO	0.01	0.23	0.24	0.06	0.20	0.16		0.13	0.11	0.12	0.13	0.08
MgO	12.82	11.92	9.90	11.30	9.35	10.69	16.34	11.39	12.09	15.86	15.52	17.38
CaO										22.64	22.22	21.35
Na ₂ O										0.26	0.24	0.23
NiO	0.17	0.14	0.16	0.09	0.17	0.14	0.30	0.16	0.19			
Total	101.55	99.04	99.13	98.83	99.49	100.27	98.99	97.65	99.59	99.45	100.58	99.39
FeO ^c	17.61	17.15	20.84	18.29	21.68	19.14	9.79	16.98	16.57			
Fe ₂ O ₃ ^c	5.37	5.27	7.48	6.25	7.50	5.81	3.81	1.91	5.32			
Fo (mol. %)												
Mg# ^d	57.38	55.73	46.20	52.83	43.90	50.38	75.48	54.96	57.00	93.17	90.75	90.84
Cr# ^e	70.84	69.49	67.27	71.55	75.06	69.89	69.85	68.67	67.82	9.44	11.39	17.00
Fe ³⁺ /R ^{3+, f}	0.08	0.07	0.10	0.08	0.11	0.08	0.05	0.03	0.07			

^a HT, high-Ti; LT, low-Ti.^b mp, microphenocrysts; ph, phenocrysts.^c FeO and Fe₂O₃ are obtained by stoichiometric calculations using equations of Barnes & Roeder (2001).^d Mg# = 100 * Mg / (Mg + Fe²⁺).^e Cr# = 100 * Cr / (Cr + Al).^f Fe³⁺/R³⁺ = Fe³⁺ / (Cr + Al + Fe³⁺).

Table 3: Representative IPGE and Rh concentrations (ppb) in chromite determined by LA-ICP-MS

Series	Sample	Grain #	Os	Ir	Ru	Rh
High-Ti	13-DJ-02	Dj2d-Cm2	18	11	162	19
	13-DJ-03	Dj3f-Cm1	42	27	236	12
	13-DJ-04	Dj4a-Cb1	21	11	284	7
	13-DJ-05	Dj5a-Ci1	19	24	203	34
		Dj5f-Cb2	16	18	322	36
	13-DJ-06	Dj6a-Cm1	40	12	275	22
	13-DJ-08	Dj8a-Ci1	17	15	283	18
		Dj8b-Cm1	32	23	336	27
	13-DJ-09	Dj9e-Cb1	91	21	148	19
	13-SM-02	Sm2c-Ci2	30	11	188	42
	13-SM-03	Sm3g-Cb1	19	17	212	55
	13-JC-01	Jc1a-Ci1	27	21	177	13
	13-JC-02	Jc2a-Cb1	19	18	231	30
	13-JC-03	Jc3a-Ci1	97	53	240	12
		Jc3b-Cm1	28	30	211	36
	13-JC-04	Jc4a-Ci1	32	25	305	12
	13-JC-06	Jc6a-Cb1	29	14	304	65
	13-JC-07	Jc7a-Cm1	32	25	222	21
Low-Ti	13-ET-02	Et2b-Ci1	83	36	122	16
		Et2c-Cb1	93	42	110	12
	13-ET-03	Et3a-Ci1	124	48	155	11
	13-ET-04	Et4b-Cm1	68	48	280	20
	13-DL-02	Dl2c-Ci1	22	15	224	4
		Dl2d-Cb1	26	30	272	10
	13-DL-03	Dl3b-Ci1	45	20	217	11
	13-DL-04	Dl4a-Cm1	12	18	226	14
		Dl4d-Cm1	15	7	222	16
	13-DL-06	Dl6a-Ci2	39	14	214	2
	13-BC-02	Bc2a-Ci2	36	26	271	10
		Bc2i-Cb1	35	26	280	20
	13-BC-04	Bc4c-Cm1	41	27	248	27
		Bc4e-Ci1	56	36	284	15
DL ^a	13-BC-05	Bc5a-Cb1	62	32	333	31
	13-BC-06	Bc6a-Cm1	21	25	251	14
		Bc6c-Ci1	22	19	323	24
	13-BC-07	Bc7f-Cm2	46	17	300	56
			7.59	3.76	5.76	1.31
	Ave. ^b		36 (65)	25 (42)	244 (32)	23 (60)
	Med. ^b		30	23	248	21

^a DL, detection limits; detection limits are based on the median values given by Iolite from 146 analyses.

^b Average and median values are based on 223 analyses, numbers in brackets represent one standard deviation (1σ) expressed in relative percent to the average.

The results of all LA-ICP-MS analyses performed on chromites are given in Electronic Appendix 4.

2.5 RESULTS

2.5.1 PETROGRAPHY OF PICRITES AND ASSOCIATED ROCKS

Most of the picrites are highly porphyritic and contain from 19 to 47 vol. % of olivine phenocrysts and microphenocrysts with minor diopsidic clinopyroxene and accessory chromite. The olivine phenocrysts and microphenocrysts are euhedral or subhedral to rounded, rarely embayed or resorbed, and range from 0.2 to 10 mm in size (Fig. 2.2a). Olivine is generally fresh or partially serpentinized with an unaltered core, but some grains are completely altered to greenish or yellowish serpentine. Strained crystals are present in some cases and characterized by slightly different extinction angles. In some picrites, native copper is present in very small amounts within the altered olivine phenocrysts, and sometimes as micro-nuggets within small serpentinized veinlets, thus appearing to be related to the serpentinization process. Secondary chalcopyrite was observed in similar contexts. The clinopyroxene phenocrysts are more abundant in picrite samples from the Jianchuan area and the Shiman and Daju lava sections, accounting for 1 to 6% of the volume of these rocks. The clinopyroxene grains are usually subhedral or anhedral, sometimes twinned or zoned, and range from 0.5 to 4.5 mm. Plagioclase phenocrysts are absent in the picrites except for sample 13-JC-02 which contains about 5 vol. % of tabular-shaped grains ranging from 0.5 to 2 mm in size. A small amount of chromite (i.e. < 1 vol. %) is present in all picrite samples. The chromite grains are euhedral or subhedral and range mainly from 50 to 800 μm . They can be subdivided into: (1) chromite microphenocrysts in the groundmass; and (2) olivine-hosted chromite inclusions. The

chromite microphenocrysts in the groundmass are generally surrounded by Ti-rich overgrowth rims which are sometimes characterized by the presence of small silicate inclusions (Fig. 2.2b), whereas the olivine-hosted chromites are characterized by sharp chromite–olivine interfaces (Fig. 2.2c). The olivine microphenocrysts (i.e. < 1 mm in size) appear to be generally devoid of chromite inclusions, these being rather observed within the larger phenocrysts. The groundmass of the picrite samples is fine grained (a few hundred micrometres), sometimes with intergranular texture, and consists predominantly of anhedral clinopyroxene and tabular-shaped plagioclase with minor devitrified glass and rare olivine grains. The plagioclase grains are sometimes altered to epidote. The groundmass also contains minor oxide minerals such as anhedral Ti-rich magnetite with minor ilmenite. Vesicles and amydales are present in some samples.

The principal flood basalt samples in this study are pyroxene-phyric basalts ($n = 5$) from the Shiman and Daju lava sections, and plagioclase-phyric basalts ($n = 3$) from the Dali and Binchuan areas. The pyroxene-phyric basalts contain from 5 to 30 vol. % of euhedral or subhedral diopsidic clinopyroxene phenocrysts and microphenocrysts, sometimes with complex zoning structure, and ranging from 0.4 to 5 mm in size (Fig. 2.2d). Some of the clinopyroxene crystals are altered, probably to actinolite and talc. Glomeroporphyritic texture is locally present in the pyroxene-phyric basalts and characterized by the agglomeration of clinopyroxene microphenocrysts, commonly forming irregular clusters or clots. The pyroxene-phyric basalts can also contain up to 5 vol. % of highly serpentinized olivine phenocrysts mainly ranging from 1 to 4 mm in size. Native copper is present in some of the pyroxene-phyric basalts, particularly within serpentinized

olivine phenocrysts from one sample of the Shiman section (13-SM-01; Fig. 2.2e). The plagioclase-phyric basalts contain about 1 to 5 vol. % of plagioclase phenocrysts and microphenocrysts with minor clinopyroxene. The plagioclase phenocrysts are partially or completely sericitized and usually form radial clusters up to 6 mm made of tabular-shaped grains ranging from 0.6 to 5 mm. Some of the phryic basalt samples from the Shiman and Daju sections contain a very small amount (i.e. < 5 grains per thin section) of euhedral or subhedral chromite microphenocrysts ranging from 100 to 400 μm . In the other phryic basalts, the major oxide minerals are magnetite and Ti-rich magnetite which are present as euhedral to anhedral microphenocrysts ranging from 100 to 700 μm and accounting for less than 1% of the volume of these rocks. The groundmass of the phryic basalts is fine grained to very fine grained, with intergranular texture, and consists mainly of tabular-shaped plagioclase (sometimes altered to epidote) and anhedral clinopyroxene with minor Ti-rich magnetite and ilmenite.

An additional sample from the Daju lava section (13-DJ-02) is an aphyric basalt with amygdaloidal texture, which is characterized by a content of about 30 vol. % of rounded vesicles ranging from 0.5 to 5 mm and mainly filled with sericitized plagioclase grains. This sample contains a small amount (i.e. < 10 grains) of euhedral or subhedral chromite microphenocrysts ranging from 100 to 200 μm . The groundmass of the aphyric basalt is fine grained and consists of a similar assemblage of minerals to that of the phryic basalts.

The OPSV rocks are mineralogically very similar to the typical Emeishan picrites, containing from about 20 to 30 vol. % of olivine phenocrysts and microphenocrysts, minor clinopyroxene and plagioclase phenocrysts, and accessory chromite. The olivine phenocrysts are euhedral or subhedral and vary in size from 0.5 to 8 mm. Olivine is partially or completely altered to serpentine. The samples contain up to 15 vol. % of euhedral or subhedral diopside microphenocrysts ranging from 0.5 to 1 mm, and up to 10 vol. % of tabular-shaped plagioclase microphenocrysts ranging from 0.5 to 1.5 mm. Chromite is also present in small amounts (i.e. < 1 vol. %) as isolated microphenocrysts in the groundmass and as olivine-hosted chromite inclusions. The chromite crystals are euhedral or subhedral and range mainly from 100 to 500 μm . The groundmass of the OPSV rocks is coarser grained than the typical picrites (up to 1 or 2 mm in size) and consists mainly of anhedral clinopyroxene and tabular-shaped plagioclase with minor Ti-rich magnetite (Fig. 2.2f).

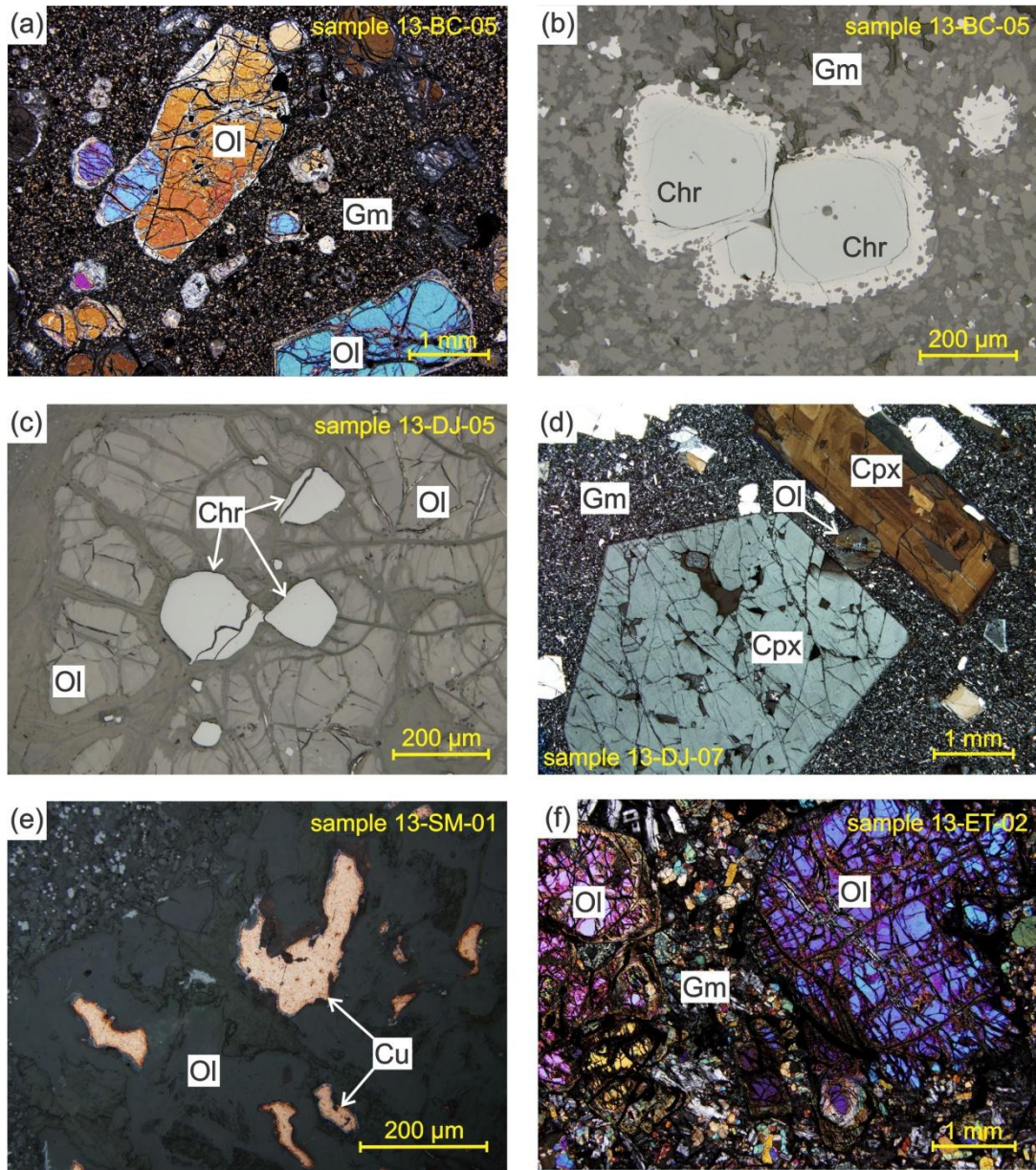


Figure 2.2 Transmitted (a, d, f) and reflected (b, c, e) light photomicrographs showing: (a) fresh olivine phenocrysts in a picrite sample; (b) euhedral microphenocrysts of chromites surrounded by Ti-rich overgrowth rims; (c) subhedral olivine-hosted chromite inclusions free of overgrowth rim; (d) clinopyroxene phenocrysts in a pyroxene-phyric basalt sample; (e) native copper in serpentinized olivine from a pyroxene-phyric basalt sample; and (f) representative textural characteristic of the OPSV rocks. Ol, olivine; Gm, groundmass; Chr, chromite; Cpx, clinopyroxene; Cu, native copper.

2.5.2 CHEMICAL CLASSIFICATION OF PICRITES

Over the last few decades, the continental flood basalts worldwide have been classified into two major magma types, the low- and high-Ti series, according to their TiO_2 content or their Ti/Y ratio (e.g. Bellieni *et al.*, 1984; Fodor, 1987; Peate *et al.*, 1992; Gibson *et al.*, 1995; Hawkesworth *et al.*, 1995). In order to reduce the influence of crystal fractionation, Xu *et al.* (2001) proposed a chemical classification for the Emeishan flood basalts based mainly on their Ti/Y ratio (the TiO_2 content tends to increase during crystal fractionation but the Ti/Y ratio does not). According to this classification, a Ti/Y ratio of 500 was used to subdivide the basalts into low- and high-Ti series. Xu *et al.* (2001) also suggest that two types of picrites can be distinguished under this classification. Combining our dataset with the literature values, we suggest that the boundary between the low- and high-Ti picrites should rather be set at Ti/Y = 440 because there is no value between 420 and 460 (Fig. 2.3). Our data show that the picrites from the Dali and Binchuan areas exhibit low Ti/Y and Sm/Yb ratios ($\text{Ti/Y} = 301\text{--}375$, $\text{Sm/Yb} = 1.70\text{--}2.47$), similar to the Emeishan low-Ti picrites previously studied by other researchers (see Fig. 2.3 caption for references), whereas the picrites from the Jianchuan and Lijiang areas (the latter includes the Shiman and Daju lava sections) exhibit higher Ti/Y and Sm/Yb ratios ($\text{Ti/Y} = 488\text{--}621$, $\text{Sm/Yb} = 2.80\text{--}3.46$) similar to other high-Ti picrites found in the ELIP. Because the Sm/Yb ratio is commonly used to indicate the depth of magma generation, the strong positive correlation with Ti/Y values suggests that both magma types were produced from two distinct mantle sources.

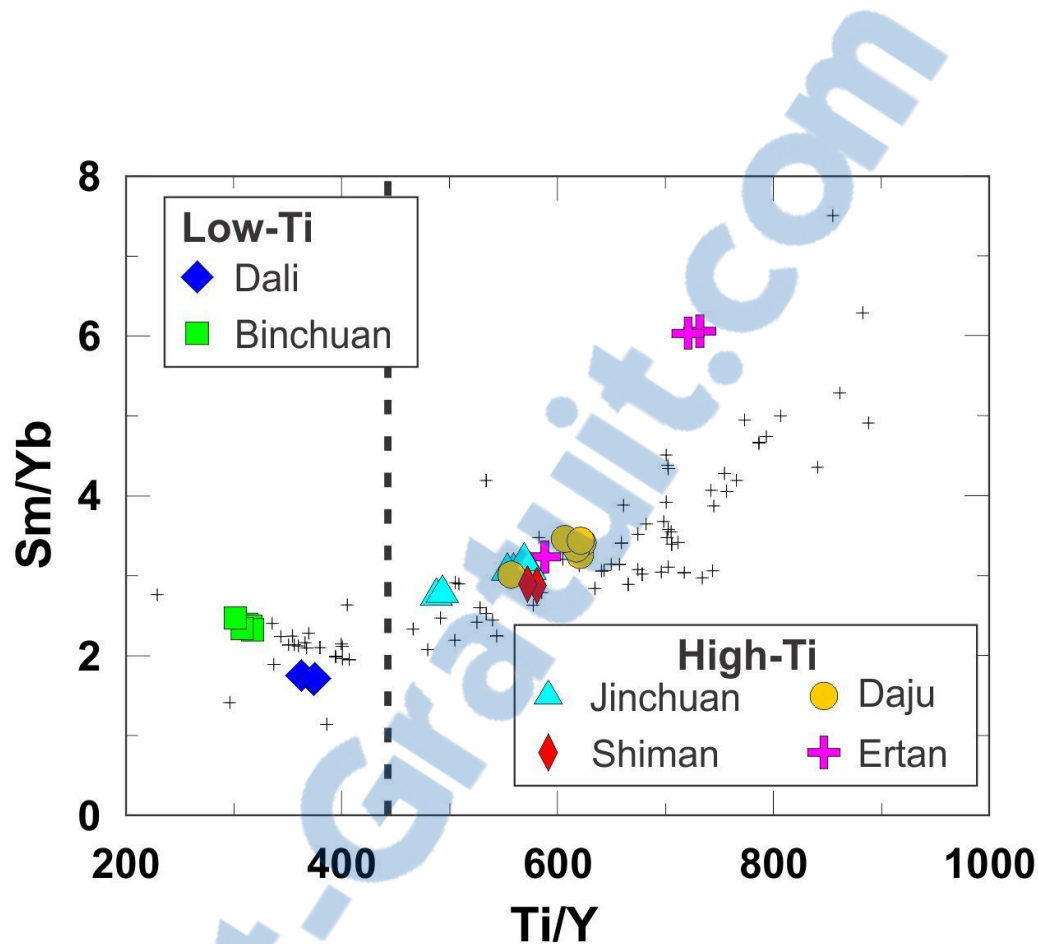


Figure 2.3 Relationships between Ti/Y and Sm/Yb for picrites and OPSV rocks reported in this study. Compiled data for the Emeishan picrites (small crosses) are from Chung & Jahn (1995), Song et al. (2001), Xu et al. (2001), Xiao et al. (2004), Zhang et al. (2006a), Hanski et al. (2010), Li et al. (2010), Kamenetsky et al. (2012), Li et al. (2012) and Bai et al. (2013). Dashed line represents the boundary between the low- and high-Ti picrites.

2.5.3 WHOLE-ROCK MAJOR AND TRACE ELEMENT COMPOSITIONS

Relationships between MgO and other major elements (SiO_2 , TiO_2 , Al_2O_3 , $\text{Fe}_2\text{O}_3^{\text{Total}}$ and CaO), and with Ni, Cr and Cu, for the Emeishan picrites and the associated rocks are presented in Figures 2.4 and 2.5. The picrites display wide variations of MgO and Cr

contents ranging from 15.82 to 30.45 wt % and from 1281 to 2513 ppm, respectively. Trends of increasing SiO₂, TiO₂, Al₂O₃ and CaO with decreasing MgO values observed for the picrites could reflect the olivine fractionation during the early stages of magmatic differentiation or the accumulation of olivine phenocrysts (Fig. 2.4a, b, c and e). Furthermore, the positive correlation between MgO and Ni is consistent with these trends, whereas the correlation between MgO and Cr reflects the fractionation or the accumulation of co-crystallizing olivine and chromite (Fig. 2.5a and b). On the other hand, the negative correlation between MgO and Cu is due to the incompatible behaviour of Cu with silicates and oxides (Fig. 2.5c).

In terms of major elements, the low- and high-Ti picrites are mainly distinguishable by their TiO₂, Al₂O₃ and Fe₂O₃^{Total} contents (see Kamenetsky *et al.*, 2012 for whole-rock trace element distinction between both types of picrites). The low-Ti picrites have relatively lower TiO₂ and Fe₂O₃^{Total} and higher Al₂O₃ contents than the high-Ti picrites at a given MgO, defining two distinct trends (Fig. 2.4b, c and d). While the major and trace element compositions of the OPSV rocks appear to be slightly different from those of the picrites, these samples show several geochemical similarities with the picrites from the high-Ti suite (Figs 2.3 and 2.4).

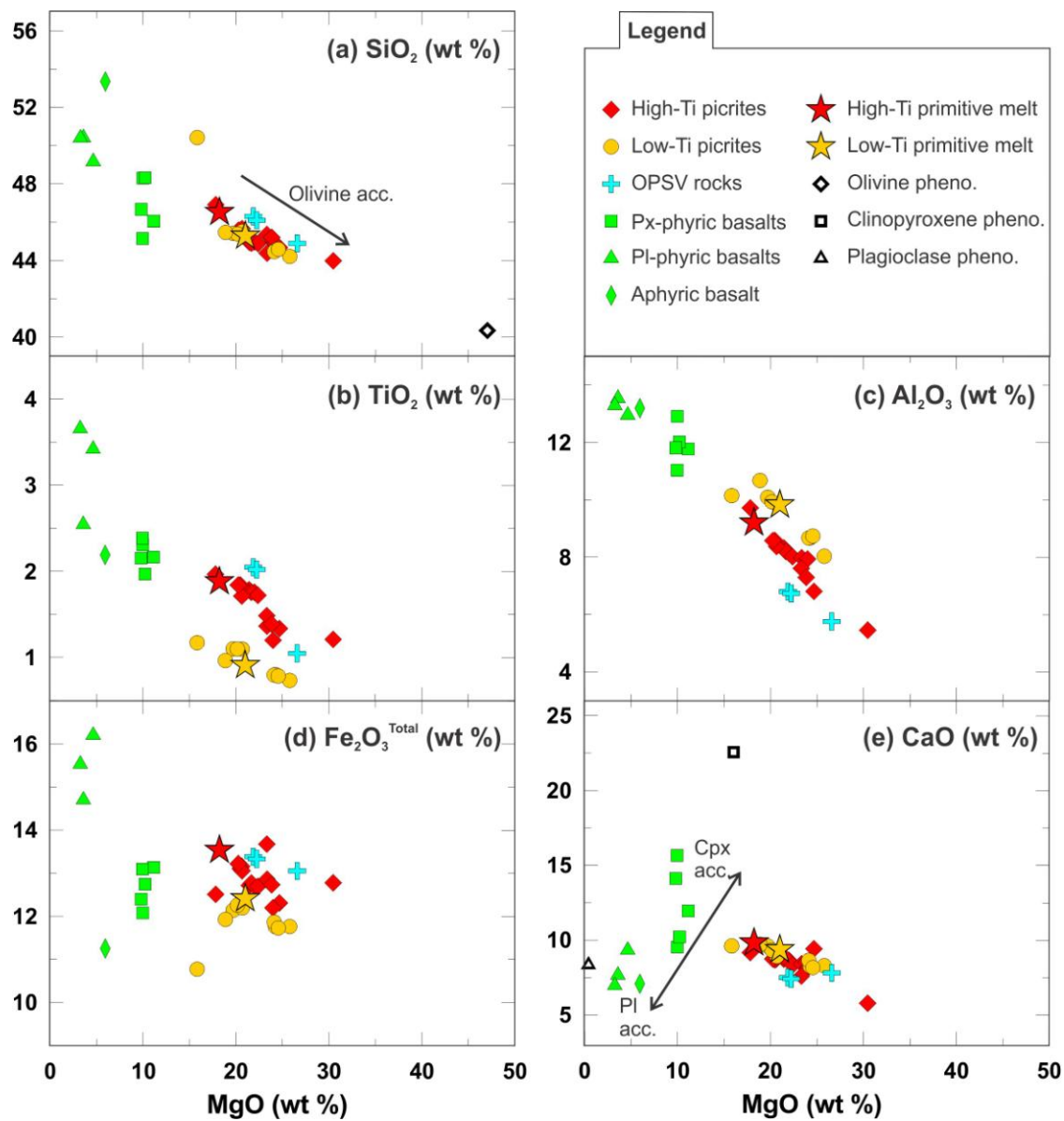


Figure 2.4 Whole-rock major elements (SiO_2 , TiO_2 , Al_2O_3 , $\text{Fe}_2\text{O}_3^{\text{Total}}$ and CaO) plotted against MgO for the studied samples. The compositions of the primitive melts in equilibrium with the most forsteritic olivine phenocrysts for the high- and low-Ti series have been calculated using Pele 7.07. The average compositions of the olivine phenocryst cores, clinopyroxene and plagioclase phenocrysts are indicated (a, e). The solid arrows represent the accumulation trends of these phenocrysts. acc., accumulation; Cpx, clinopyroxene; pheno., phenocrysts; Pl, plagioclase; Px, pyroxene.

Based on the highest forsterite (Fo) content of olivine phenocrysts from the high-(Fo = 91.1 mol. %) and low-Ti picrites (Fo = 92.9 mol. %), we calculated the compositions of the primitive melts which would be in equilibrium with these olivine phenocrysts (Fig. 2.4; Table 1). The liquids calculated for both magma types contain between ~18 to 21 wt % MgO, which is considerably lower than the MgO content of most of the picrites. Therefore, our results suggest that the wide range of MgO and Ni content of the picrites (Fig. 2.5a) is due partly to the evolution of the primitive melt, but mostly to the accumulation of various proportions of olivine phenocrysts which appear to have crystallized at depth and subsequently been transported to the Earth's surface within these lava flows. Similarly the range in Cr content is due to the accumulation of various proportions of chromite microphenocrysts in the rocks.

The flood basalts have significantly lower MgO and Cr contents than the picritic rocks (MgO = 3.24–9.94 wt % and Cr = 6–712 ppm; Fig. 2.5b). The distinction between the pyroxene- and plagioclase-phyric basalts is easily made by using SiO₂, TiO₂, Fe₂O₃^{Total}, MgO and CaO contents (Fig. 2.4a, b, d and e), reflecting the accumulation of distinct proportions of clinopyroxene and plagioclase phenocrysts. This feature is more clearly illustrated by the positive correlation between MgO and CaO, which extends approximately between the average compositions of clinopyroxene and plagioclase phenocrysts (Fig. 2.4e). In general, the aphyric basalt (sample 13-DJ-02) is not compositionally similar to particular phyric basalt types in terms of major element content due to the absence of cumulative phenocrysts.

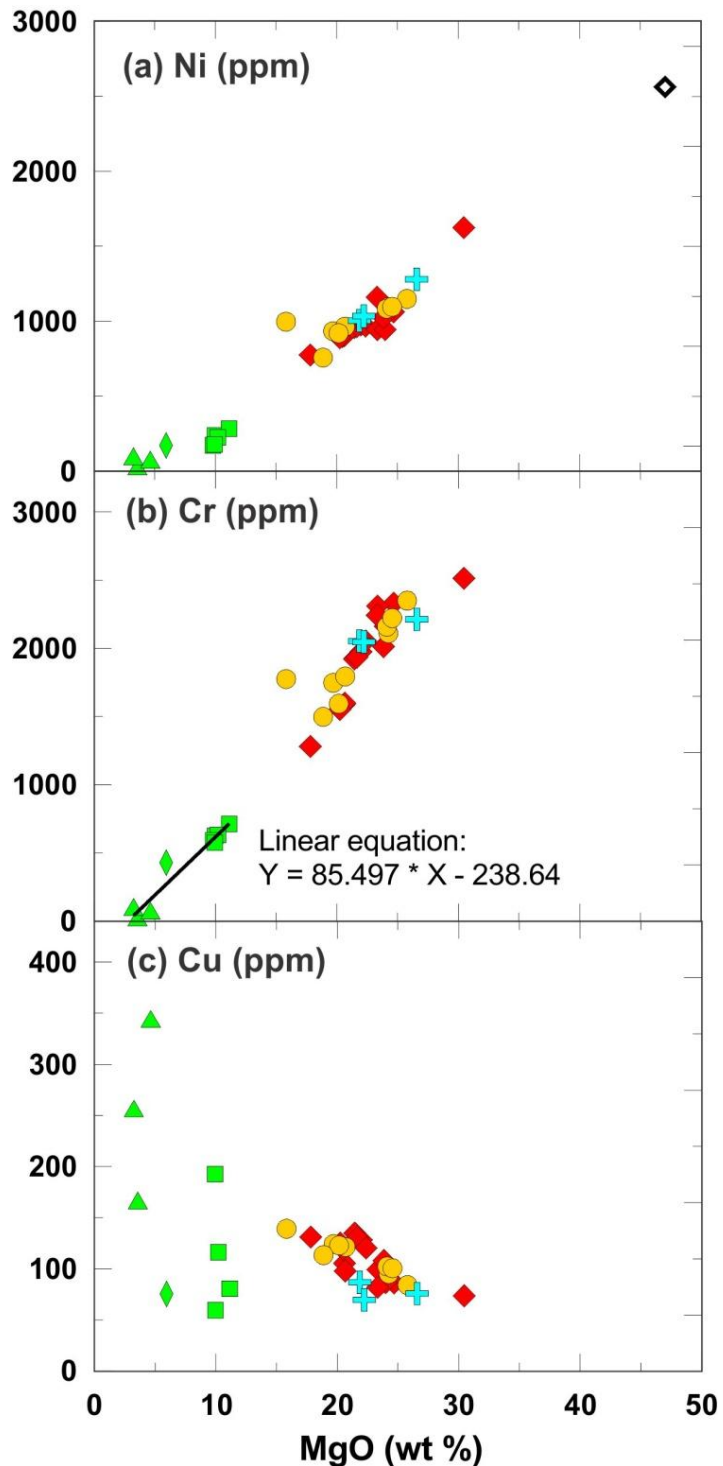


Figure 2.5 Whole-rock Ni, Cr and Cu plotted against MgO for the studied samples. Symbols as in Fig. 2.4. The linear equation in the diagram of Cr vs. MgO is from the trend of the basalt samples (solid line).

In contrast to the picritic samples, the basalts show wide variation in their Cu content. As shown in Figure 2.5c, some of the basalt samples are clearly Cu-depleted relative to others, suggesting modification of Cu concentrations possibly in response to the removal of sulphide liquid from magma. Moreover, the concentrations of Cu could also have been modified by the addition of native copper or secondary chalcopyrite, thus promoting a Cu enrichment of some samples (note that the basalt sample 13-SM-01 is not included in Fig. 2.5c because it contains too much Cu to fit on the figure due to the presence of a greater amount of native copper; see previous section ‘Petrography of picrites and associated rocks’, and Table 1).

The primitive mantle-normalized Ni–PGE–Cu patterns for the picrites and the associated rocks are shown in Figure 2.6. In general, the picrite samples are characterized by relatively high IPGE contents and low Pd/Ir ratios ($\Sigma\text{IPGE} = 2.71\text{--}9.17 \text{ ppb}$, $\text{Pd/Ir} = 1.65\text{--}12.59$; Table 1), which are close to the primitive mantle values ($\Sigma\text{IPGE} = 11.6\text{--}11.8 \text{ ppb}$, $\text{Pd/Ir} = 1.18\text{--}1.22$; McDonough & Sun, 1995; Barnes & Maier, 1999), thus defining slightly fractionated PGE patterns with moderate depletion of IPGE relative to PPGE (Fig. 2.6a and b). On the other hand, the OPSV rocks are characterized by similar PGE patterns with enrichments of IPGE and Pt (Fig. 2.6a), whereas the flood basalt samples are characterized by highly fractionated PGE patterns resulting from lower IPGE contents and higher Pd/Ir ratios than the picrites ($\Sigma\text{IPGE} = 0.03\text{--}1.07 \text{ ppb}$, $\text{Pd/Ir} = 14.34\text{--}245.02$; Fig. 2.6c, Table 1). The high IPGE contents of picrites, their low Pd/Ir ratios combined with high MgO, Ni and Cr, as well as the presence of highly forsteritic olivine phenocrysts in the picrites (see below), are all consistent with the idea that the picrites represent compositions

close to the primitive melts of the ELIP (e.g. Chung & Jahn, 1995; Ali *et al.*, 2005; Hanski *et al.*, 2010; Zhou *et al.*, 2013). Although the high- and low-Ti magmas are known to be produced from two distinct mantle sources, picrites from both suites have very similar PGE patterns, except that some high-Ti picrites exhibit a negative Pd anomaly.

As shown in diagrams of Cr vs. PGE, whole-rock IPGE, and particularly Ru, these all correlate positively with whole-rock Cr (Fig. 2.7a, b and c). As discussed in the introduction, the correlations between whole-rock IPGE and Cr observed for many other sulphide-undersaturated volcanic and plutonic rocks have led many researchers to propose that chromite plays a role in the fractionation of these elements. Since Ru appears to be more compatible with chromite than Os, Ir and Rh (Pagé *et al.*, 2012; Park *et al.* 2012), the crystallization of chromite would create a negative Ru anomaly in the Ni–Cu–PGE patterns, such as we observed for the least evolved basalts from the ELIP (i.e. pyroxene-phyric; Fig. 2.6c), and which support the proposal that chromite contributes to the IPGE fractionation. On the other hand, the overall depletion in IPGE with the magmatic evolution could be attributed to the combined effect of the partitioning of these elements into chromite and the co-crystallization of IPGM and chromite (Barnes & Fiorentini, 2008; Fiorentini *et al.*, 2008; Pagé *et al.*, 2012). However, because MgO correlates with Cr, as well with IPGE (not shown), it is also possible that olivine plays a role in the fractionation of IPGE.

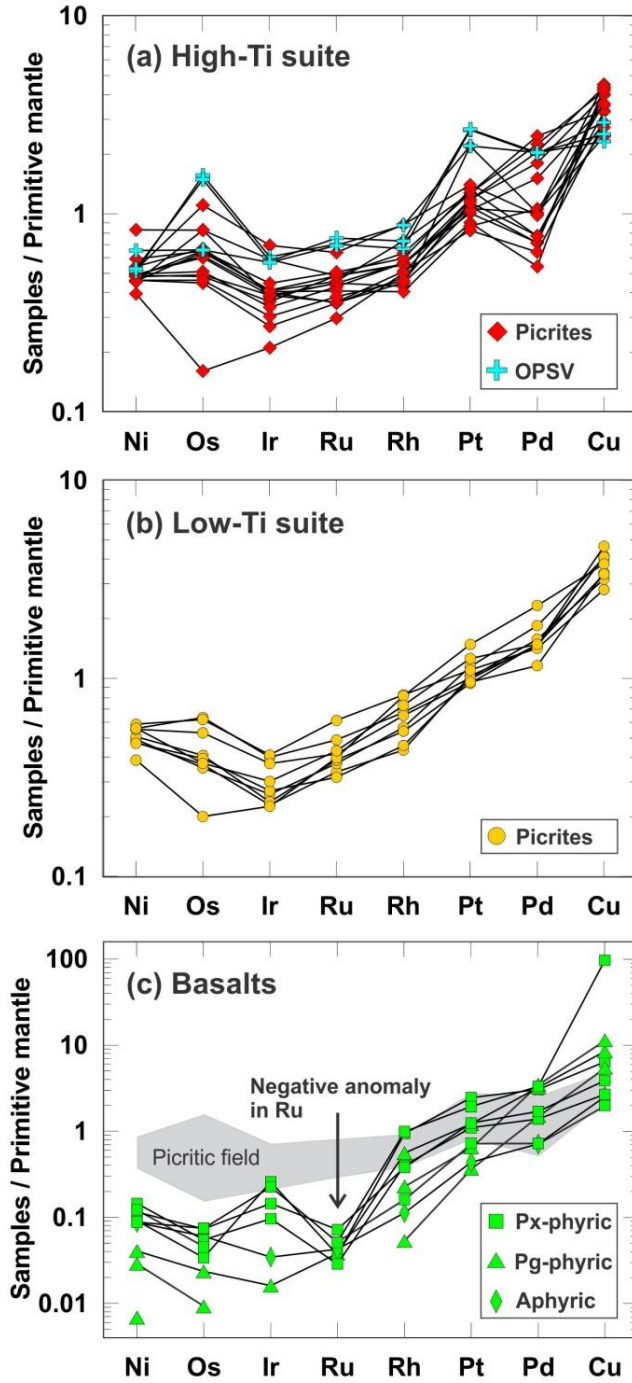


Figure 2.6 Primitive mantle-normalized Ni–PGE–Cu patterns for: (a) the high-Ti picrites and the OPSV rocks; (b) the low-Ti picrites; and (c) the flood basalts reported in this study. The negative Ru anomaly shown by the pyroxene-phyric basalts is indicated. The primitive mantle values are from McDonough & Sun (1995).

In contrast to IPGE, whole-rock PPGE do not correlate with whole-rock Cr (Fig. 2.7d, e and f). The samples display wide variations of PPGE which are more pronounced for the flood basalts, some of which appear to be PPGE-depleted. As will be seen below, several factors may be responsible for whole-rock PPGE variations in the Emeishan volcanic rocks, such as the segregation of a very small amount of sulphide from the magma and the crystallization of PPGE-bearing phases like chromite (only in the case of Rh) and PGM.

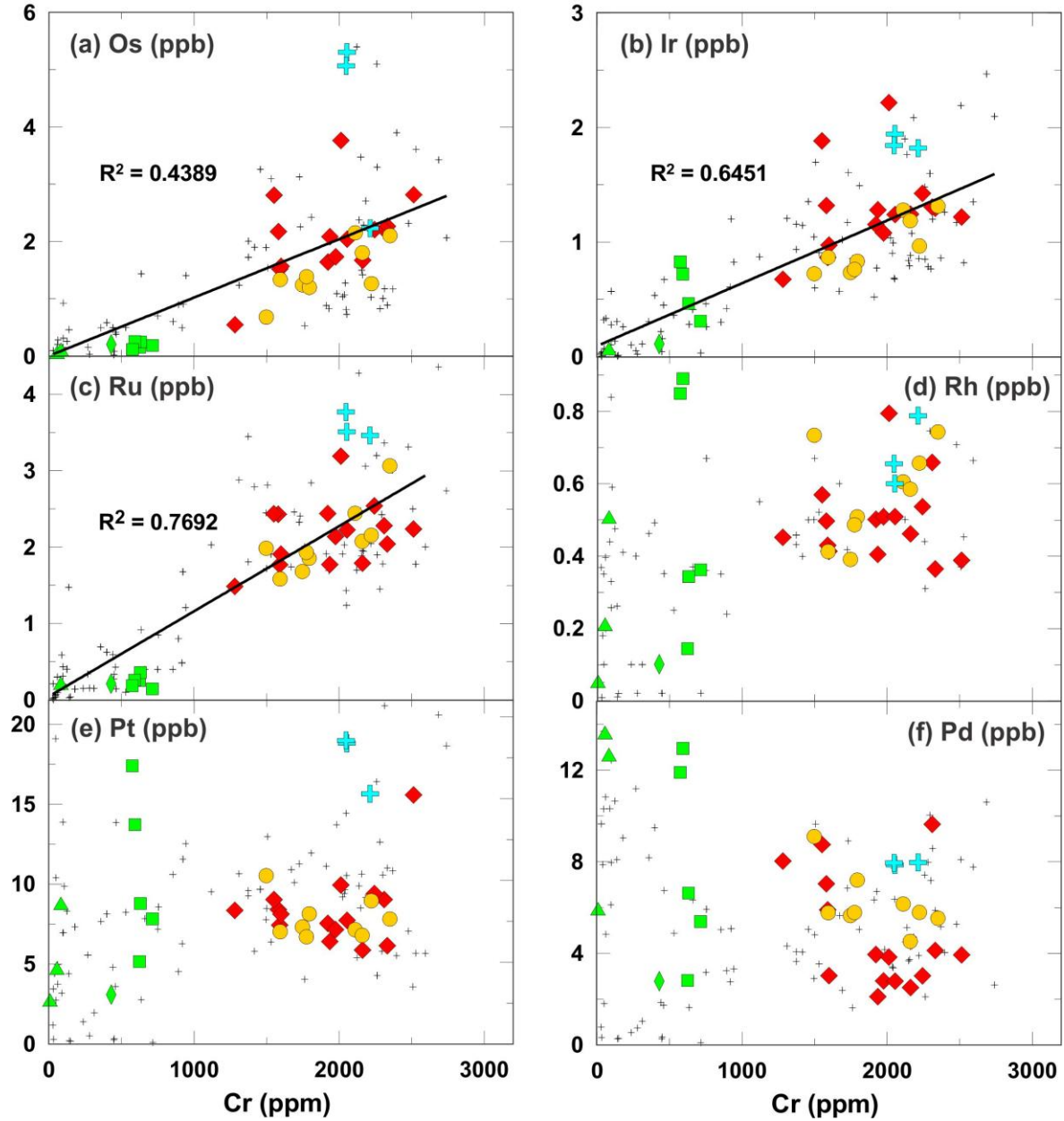


Figure 2.7 Whole-rock PGE plotted against Cr for the studied samples. Symbols as in Fig. 2.4. Compiled data for other Emeishan picrites and flood basalts (small crosses) are from Zhang et al. (2005), Li et al. (2012), Bai et al. (2013) and Li et al. (2014). The solid lines illustrate the positive correlations between IPGE and Cr for the whole dataset. These correlations, as well as the negative anomaly in Ru shown by the PGE patterns of the flood basalts (Fig. 2.6c), suggest that chromite plays a role in the fractionation of these elements.

2.5.4 PRIMARY MINERAL ASSEMBLAGE

2.5.4.1 OLIVINE

The olivine phenocrysts in the picrites and the OPSV rocks exhibit a variable Fo content with the highest values for the high- and low-Ti series of 91.1 and 92.9 mol. %, respectively. In general, the olivine phenocrysts from the low-Ti picrites tend to have a relatively higher Fo content than the phenocrysts from the high-Ti suite ($\text{Fo} = 84.0\text{--}92.9$ and 82.3–91.1 mol. %, respectively; see Table 2 and Electronic Appendix 2). As shown in Figure 2.8, significant ranges in Fo in a single sample suite are accompanied by changes in MnO and NiO contents, which seem to reflect the removal of olivine during crystal fractionation of the primitive melts. Consequently, because the values of MnO increase with decreasing Fo in olivine (Fig. 2.8a), phenocrysts from the low-Ti picrites tend to have a higher MnO content than those from the high-Ti suite. On the other hand, the weak correlation observed between Fo and NiO in olivine (Fig. 2.8b) does not allow us to subdivide the olivine phenocrysts in terms of NiO relative to their magmatic affinity.

A reduction in Fo content from the core to the outermost rim of the olivine phenocrysts, with a maximum core–rim variation value of 5.6 mol. %, suggests that the composition of olivine changed with time as the magma evolved, and therefore that the cores of the phenocrysts are not in equilibrium with the final composition of the melt. Li *et al.* (2012) observed core–rim variation values up to 7 mol. % in olivine phenocrysts from the Daying and Wumulaka areas. Conversely, the lack of compositional zoning in olivine microphenocrysts combined with their relatively low Fo content ($\text{Fo} \leq 85.0$; see Fig. 2.8)

suggest that they represent a late-formed population of olivine that crystallized in equilibrium with compositions close to the final composition of the melt. However, it appears that these microphenocrysts could also correspond to sections cut through the Fo-poor rims of olivine phenocrysts, and consequently not to a late-formed population, but instead to a late overgrowth.

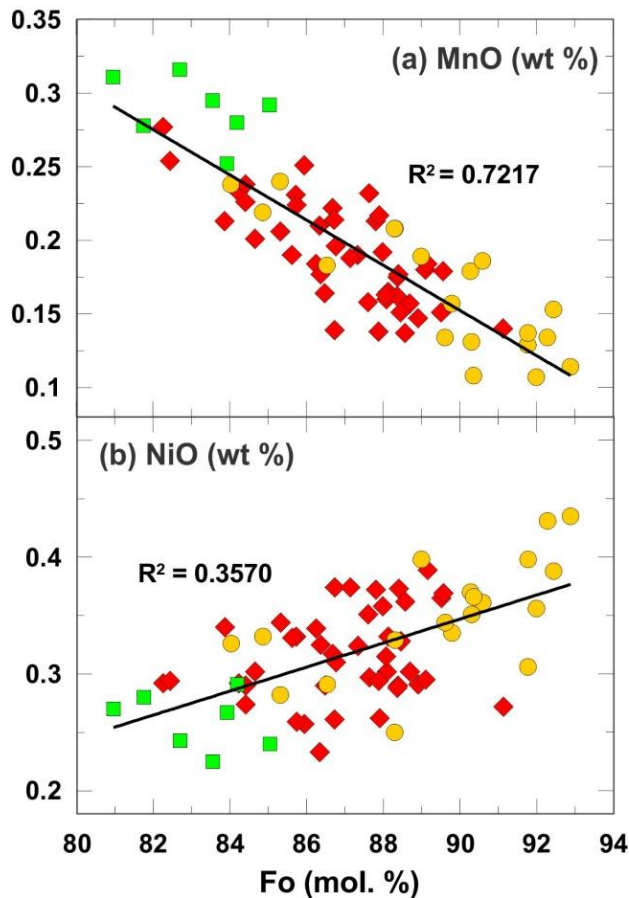


Figure 2.8 Diagrams showing variation of (a) MnO and (b) NiO against Fo for the olivine phenocrysts from the Emeishan high-Ti (diamonds, including OPSV samples) and low-Ti (circles) picritic rocks, and olivine microphenocrysts (squares) from both suites. The correlations shown in the diagrams appear to reflect the chemical evolution of the magmas during fractional crystallization of the primitive melts.

2.5.4.2 CHROMITE

Chromites in the Emeishan volcanic rocks are present as isolated microphenocrysts in the groundmass and as olivine-hosted inclusions. In general, the chromites from the groundmass exhibit a lower Mg# (where $Mg\# = 100 * Mg / (Mg + Fe^{2+})$) than the olivine-hosted chromites, with an intra-sample variation between both populations of up to 20, probably in response to a stronger Fe–Mg exchange between the microphenocrysts from the groundmass and the surrounding melt than between the chromite inclusion and its olivine host. The positive correlation observed between the average Mg# of the chromite inclusions and the average Fo of the olivine phenocrysts from each sample ($R^2 = 0.3878$ ($n = 27$); not shown), as well as the presence of sharp chromite–olivine interfaces (Fig. 2.2c), suggest that chromite inclusions are in equilibrium with the host olivine phenocrysts (Kamenetsky *et al.*, 2012). On the other hand, the occurrence of Ti-rich overgrowth rims surrounding the microphenocrysts from the groundmass does not imply only that chromites are not in equilibrium with the composition of the evolved melts, but also suggests a change in the rate and style of crystal growth happening when the magma is relatively close to the Earth's surface (Fig. 2.2b; see Roeder *et al.* (2001) for more details about growth forms of chromite).

The microprobe data allowed us to demonstrate that the compositions of chromites strongly reflect the composition of the magma from which they crystallize. For example, chromites from the high-Ti suite have a significantly higher TiO_2 content with a wider range than chromites from the low-Ti picrites ($TiO_2 = 0.77\text{--}5.63$ and $0.26\text{--}1.62$ wt %,

respectively). In response to the good correlations between TiO_2 and the major elements, the most Ti-rich chromites tend to be slightly depleted in Al_2O_3 , Cr_2O_3 and Mg# relative to the chromites from the low-Ti suite (Fig. 2.9). These chemical differences are also reflected by the fact that the high-Ti chromites have relatively higher Cr# ($\text{Cr\#} = 100 * \text{Cr} / (\text{Cr} + \text{Al})$) than the low-Ti chromites ($\text{Cr\#} = 60\text{--}78$ and $57\text{--}74$, respectively; see Table 2 and Electronic Appendix 2). The obvious compositional differences in terms of TiO_2 , Al_2O_3 and Mg# between the high- and low-Ti chromites are consistent with the differences observed between both magma types from the whole-rock compositions (see Fig. 2.4). Similar observations have also been reported by Hanski *et al.* (2010) and Kamenetsky *et al.* (2012), both of whom have worked on the composition of the picrites in the ELIP.

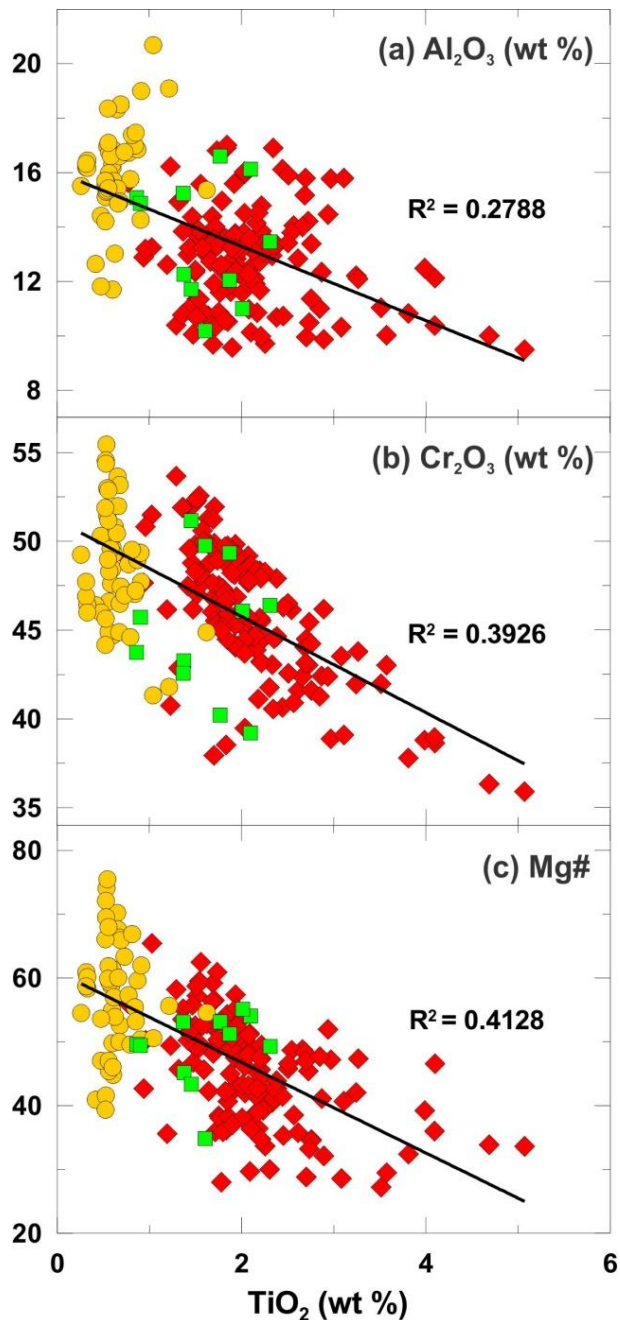


Figure 2.9 Diagrams showing variation of Al_2O_3 , Cr_2O_3 and Mg# against TiO_2 contents of chromites from the Emeishan high-Ti (diamonds, including OPSV samples) and low-Ti (circles) picritic rocks, and from the aphyric basalt (squares; sample 13-DJ-02). Variation of these geochemical parameters reflects the compositions of the magma types (i.e. high- and low-Ti) from which the chromite crystallized.

2.5.4.3 CLINOPYROXENE

Most of the clinopyroxene in the samples are Fe-poor diopside. However, microprobe data suggest that a few crystals of augite are also present in picritic samples from the Daju, Jianchuan and Ertan areas. As also observed for the chromite, the compositions of clinopyroxenes in terms of major elements, and particularly Al_2O_3 , reflect the compositions of the magmas from which they crystallized (see Table 2 and Electronic Appendix 2). Furthermore, it has been demonstrated by Kamenetsky *et al.* (2012) that the clinopyroxene phenocrysts from high- and low-Ti suites can also be distinguished by their trace element content.

2.5.5 IPGE AND RH IN CHROMITES DETERMINED BY LA-ICP-MS

As previously discussed, it is well known that PGE are commonly present as micrometric-sized inclusions of PGM in chromite from sulphide-undersaturated plutonic rocks. In sulphide-undersaturated volcanic rocks, PGE can be present as hosted-chromite PGM, but it has recently been demonstrated that IPGE and Rh can also be present in solid solution in the chromite structure (Locmelis *et al.*, 2011; Pagé *et al.*, 2012; Park *et al.*, 2012). Both PGM inclusions and IPGE and Rh solid solutions were detected in chromites from the Emeishan samples after performing *in situ* LA-ICP-MS analyses. Figure 2.10a shows an example of Cr, V, Zn, IPGE and Rh signals for an ablation on a chromite grain from one of the picrite samples. The time-resolved IPGE and Rh signals do not show any peaks, thus

indicating that these elements are present in solid solution in the chromite structure (for this example the signals correspond to ~ 29 ppb Os, ~23 ppb Ir, ~337 ppb Ru and ~56 ppb Rh). The strong uniformity of the signals indicates that these elements are generally not present as PGM inclusions or PGE clusters in the chromite. However, Figure 2.10b shows an example of peaks of Os–Ir (\pm Ru) that indicates that these elements are locally present in the chromite as Os–Ir-rich phase inclusions; moreover, peaks of Pt (\pm IPGE and Rh) also suggest the presence of chromite-hosted Pt-rich phases. These inclusions are suspected to be Os–Ir and Pt–Fe alloys, respectively.

The concentrations of PGE in chromites from the Emeishan volcanic rocks indicate that Ru is the most abundant PGE in the chromite structure with concentrations ranging from 52 to 448 ppb (median (med.) = 248), followed by Os, Ir and Rh with concentrations ranging from 8 to 151 ppb (med. = 30), 6 to 56 ppb (med. = 23), and 2 to 93 ppb (med. = 21), respectively (see Table 3 for representative concentrations of IPGE and Rh in chromites, and Electronic Appendix 4 for all LA-ICP-MS analyses). The concentrations of Pt and Pd in chromites are below the detection limit (DL) for all samples (DL = 17 and 10 ppb, respectively). As shown in Figure 2.11a (high-Ti picrites and OPSV) and 2.11b (low-Ti picrites), chromites from each picritic rock type have broadly similar primitive mantle-normalized IPGE–Rh patterns, which are depleted in Os, Ir and Rh relative to Ru. The patterns are characterized by the following particularities: (1) Ru does not show a significant inter-sample variation; (2) Os and Ir show a greater variability than Ru, which is expressed by simultaneous variations of both elements; (3) chromites from the OPSV rocks are clearly enriched in Os and Ir relative to the picrite range; and (4) Rh shows a greater

variability than IPGE (up to 1 order of magnitude). Although the IPGE–Rh pattern for the chromites from the only basalt sample on which we performed ablations (sample 13-DJ-02; Fig. 2.11c) is depleted in Ir relative to the picritic chromite range, values for Os, Ru and Rh are still included in this range.

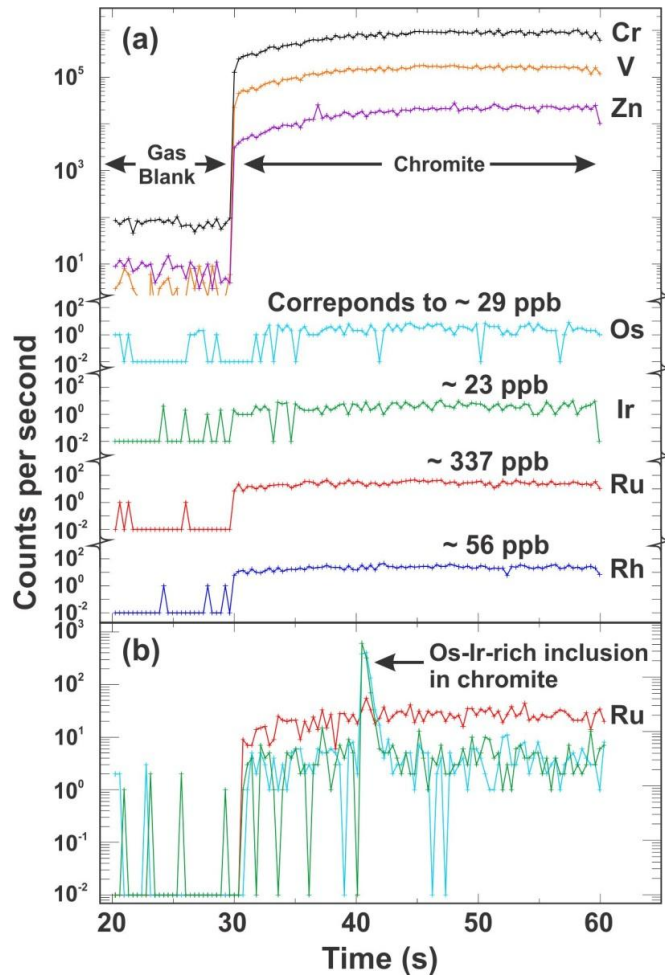


Figure 2.10 Chemical profiles (Cr, V, Zn, Os, Ir, Ru and Rh), in counts per second vs. time (in seconds), from in situ LA-ICP-MS analyses of chromites from the Emeishan picrites: (a) shows an example of uniform IPGE and Rh concentrations in chromite, indicating that these elements are present in solid solution in the chromite structure (chromite #Jc6e-Cb1); and (b) shows an example of peaks in Os and Ir (\pm Ru) due to the presence of a micrometric-sized Os–Ir-rich phase included within chromite (chromite #Jc6c-Ci1).

As shown in Figure 2.12a, the good positive correlation between the concentrations of Os and Ir in chromites suggests that both elements have a very similar behaviour during the crystallization of chromite. In contrast, Ru in chromites weakly correlates with Os and Ir for the picrites, but only with Ir for the OPSV rocks (Fig. 2.12b and c). While Rh does not show correlation with Ru (Fig. 2.12d) nor with the other IPGE (not shown), it appears that this element is more sensitive to the major element composition of chromite. Indeed, in contrast to IPGE, Rh shows good correlation with most of the major elements in chromites, including a positive correlation with the $\text{Fe}^{3+}/\text{R}^{3+}$ ratio ($\text{R}^{3+} = \text{Cr} + \text{Al} + \text{Fe}^{3+}$), and therefore with the degree of inversion of the chromite structure. As discussed below, this observation is consistent with the experimental results of Brenan *et al.* (2012), who proposed that the incorporation of Rh (but also Ir and Ru) could be enhanced by an increase of the degree of inversion of the spinel structure.

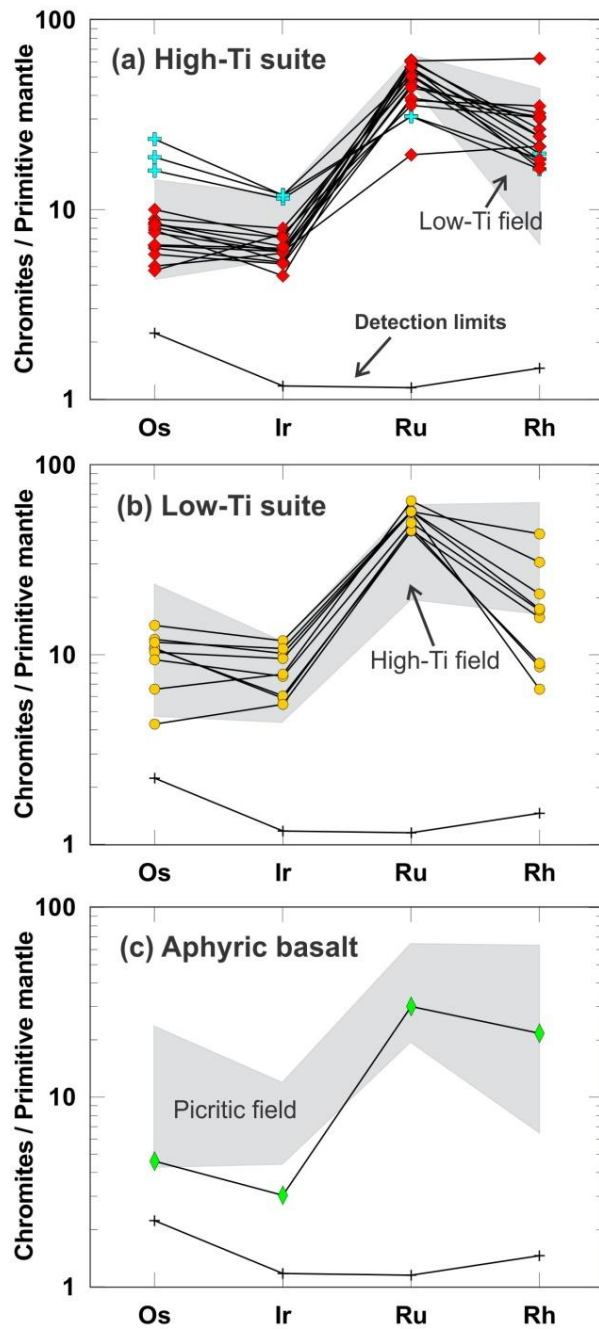


Figure 2.11 Primitive mantle-normalized IPGE–Rh patterns for chromites from (a) the high-Ti and (b) low-Ti suites, and (c) the aphyric basalt. The patterns represent the median values of IPGE and Rh concentrations in chromites determined for each sample. The pattern for the median limits of detection is shown in each diagram. The normalizing primitive mantle values are from McDonough & Sun (1995).

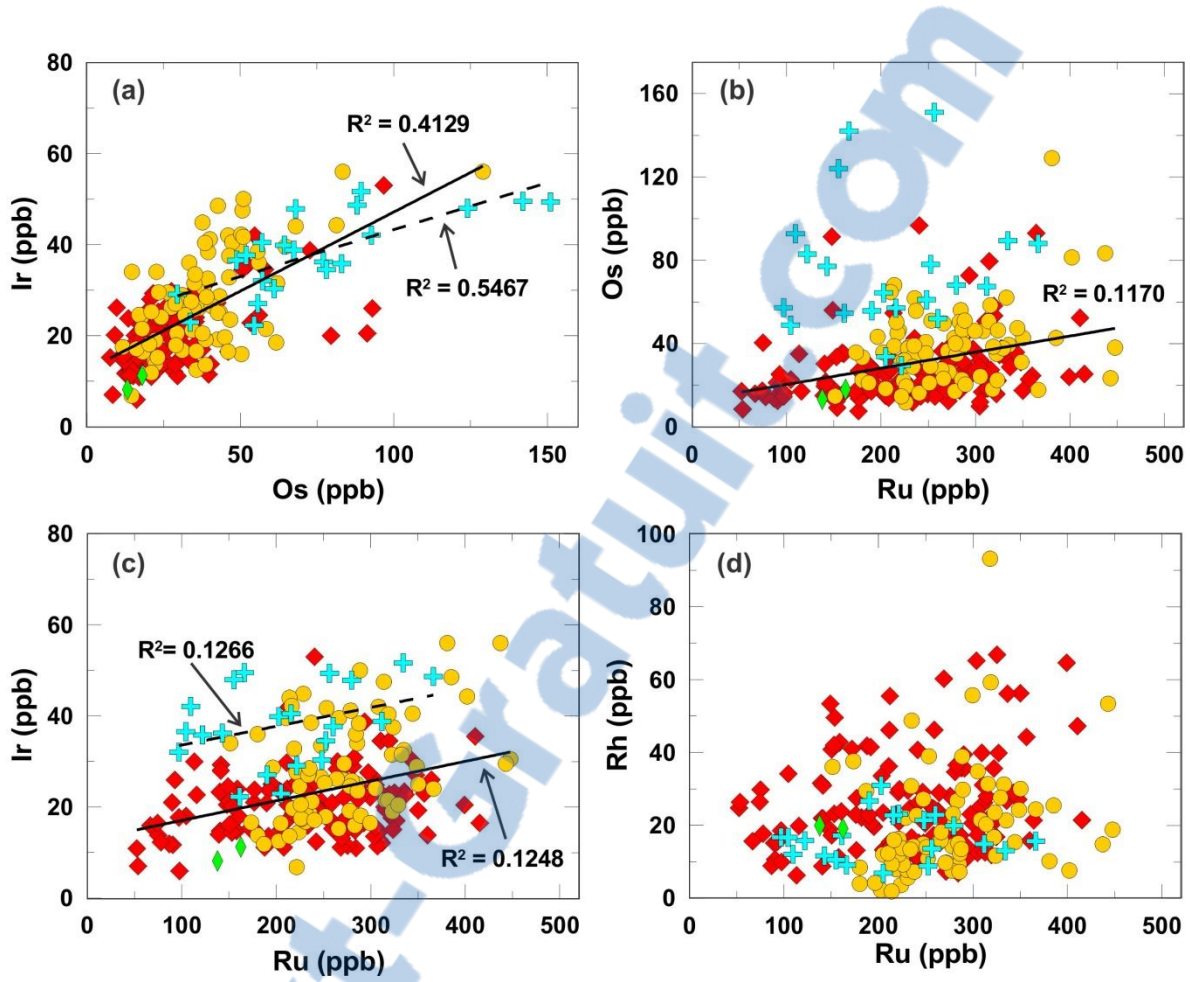


Figure 2.12 Diagrams showing variation of (a) Ir against Os, and (b, c, d) Os, Ir and Rh against Ru, respectively, for individual chromites from the Emeishan picritic rocks and the aphyric basalt. Symbols as in Fig. 2.4. Solid lines and dashed lines represent the trend of chromites from the picrites and the OPSV rocks, respectively.

2.5.6 PRESENCE OF PGM GRAINS RELATED TO THE EMEISHAN CHROMITES

As discussed above, time-resolved signals allowed us to observe the occurrence of Os–Ir and Pt–Fe alloy inclusions in the Emeishan chromites. About 50 inclusions have been listed

in this way. In order to confirm their presence, chromites from three picrite samples were studied by SEM at the IOS Services Géoscientifiques Inc. Laboratory in Chicoutimi (Québec). Five micrometric-sized PGM grains were observed in association with chromite crystals. Backscattered electron (BSE) images show that PGM micro-grains are mainly euhedral and range from ~0.3 to 0.7 µm in size (Fig. 2.13). Three of the five grains were observed at the margin of chromite crystals (Fig. 2.13a and b), in some cases within the reaction product formed at the boundary layer (Fig. 2.13c), whereas the other two were found as inclusions into chromites (Fig. 2.13d).

The compositions of PGM measured by semi-quantitative analyses are given in Table 4. Our results indicate that these PGM correspond to Pt–Fe alloys ($n = 3$; Fig. 2.13a and d), laurite (RuS_2 ; $n = 1$; Fig. 2.13b) and sperrylite (PtAs_2 ; $n = 1$; Fig. 2.13c). Most of them contain a certain amount of Os and Ir, whereas only one PGM, identified as a Pt–Fe alloy, contains Rh. The Fe content in the Pt–Fe alloys could not be determined owing to the secondary fluorescence from the adjacent chromites. However, the fact that their composition in terms of PGE is remarkably similar to the composition of chromite-hosted Pt–Fe alloys reported by Park *et al.* (2012) in the Ambae lavas (Vanuatu) leaves no doubt about their nature (compositions of PGM reported by Park *et al.* (2012) are also given in Table 4). Unfortunately, no Os–Ir alloys have yet been found by SEM.

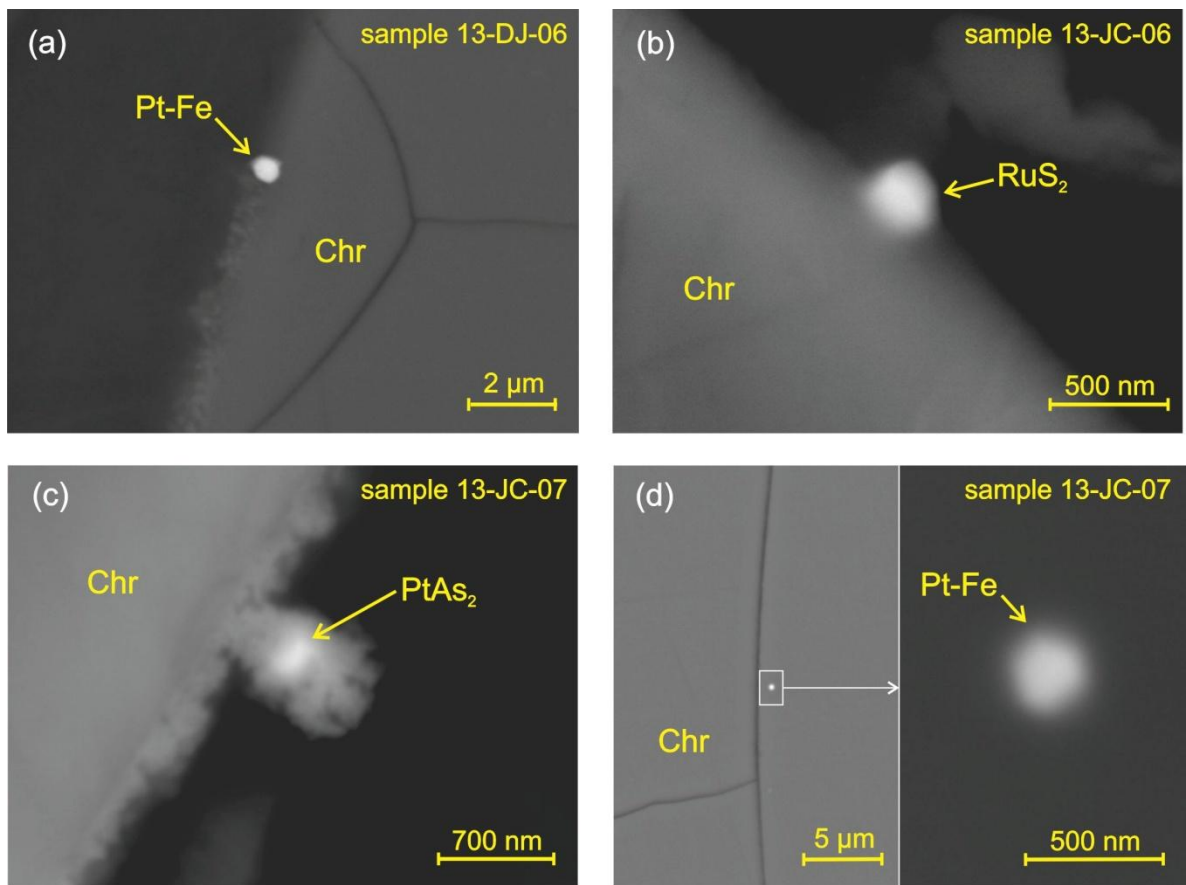


Figure 2.13 BSE images showing: (a) a euhedral Pt–Fe alloy grain at the margin of a chromite crystal; (b) a euhedral laurite (RuS_2) at the margin of a chromite crystal; (c) an indistinctly shaped sperrylite (PtAs_2) included within the reaction product formed at the boundary layer of a chromite grain; and (d) a euhedral Pt–Fe alloy grain included within a chromite crystal. All images are taken from picrite samples.

Table 4: Compositions of PGM from the Emeishan picrites determined by semi-quantitative analyses

Sample	PGM	Os (wt %)	Ir	Ru	Rh	Pt	S	As	Fe	Total
<i>Emeishan picrites</i>										
13-JC-06	Laurite	2.93	6.03	57.29			33.75			100.00
13-DJ-06	Pt–Fe alloy	12.12	6.78	2.35		78.74				100.00
	Pt–Fe alloy			4.11			95.89			100.00
13-JC-07	Pt–Fe alloy	2.00	2.98	2.88	2.62	89.52				100.00
	Sperrylite					52.29		47.71		100.00
<i>Ambae lavas *</i>										
68591-H01	Pt–Fe alloy	1.60	3.00		0.81	89.00			5.30	
	Pt–Fe alloy	7.70	5.40		0.90	81.10			4.90	

Compositions of PGM in this study were measured by energy dispersive X-ray spectroscopy (EDS).

* Compositions of Pt–Fe alloys in the Ambae lavas are from Park *et al.* (2012).

2.6 DISCUSSION

2.6.1 THE EFFECTS OF SULPHIDE REMOVAL ON PGE CONCENTRATIONS IN WHOLE ROCK

Platinum-group elements and Cu variations in the Emeishan volcanic rocks appear to be partly due to sulphide liquid segregation from the magma as suggested by the occurrence of Cu–PPGE-depleted basalts (see Figs 2.5c and 2.7d, e and f). Because Pd and Cu are both considered as incompatible elements, and the partition coefficients between silicate and sulphide liquid are higher for Pd than Cu (e.g. Vogel & Keays, 1997; Barnes & Maier, 1999; Barnes & Lightfoot, 2005), depletion of Pd relative to Cu can provide an estimation of the percentage of crystal fractionation under sulphide-saturated conditions required to deplete the magma in PGE and other chalcophile elements.

In a diagram of Cu/Pd vs. Pd (Fig. 2.14), we plotted a curve representing the crystal fractionation with removal of sulphide liquid in approximately cotectic proportions. Assuming a partition coefficient for Pd and Cu between silicate and sulphide liquid of 50,000 and 1000, respectively, the concentrations of both elements in the fractionated liquid (C_f) was calculated according to the Rayleigh fractionation as follows:

$$C_f = C_i \times F^{((D_{Sul} \times F_{Sul})-1)} \quad (1)$$

where C_i = concentration of the element in the initial liquid, F = the weight fraction of remaining liquid, D_{Sul} = partition coefficient of the element between silicate and sulphide liquid, and F_{Sul} = the weight fraction of sulphide removed in cotectic proportions determined according to a S content of 1000 ppm under sulphide-saturated conditions (see Li & Ripley, 2005) and to the average S content in magmatic sulphides (~35 wt %). We assume that Pd and Cu concentrations in the least Pd-depleted picrite correspond approximately to the concentrations in the initial silicate liquid (i.e. 9.63 ppb Pd and 99.2 ppm Cu), making no specific distinction between Pd and Cu concentrations in the high- and low-Ti initial liquids because Ni–PGE–Cu normalized patterns indicated that both magma types appear to be compositionally similar in terms of these elements (see Fig. 2.6a and b). Our results show that the removal of sulphide liquid caused by 1% of crystal fractionation will reduce the Pd concentration in the magma by a factor of 0.24; in contrast, Cu will be marginally depleted by 0.99. Assuming that the partition coefficient into sulphide liquid is the same for all PGE (i.e. 50,000), depletion of Pd relative to Cu suggests that most of the picrites are slightly PGE-depleted, and that this depletion is generally caused by less than

1% of crystal fractionation under sulphide-saturated conditions with a depletion factor varying between 0.91 and 0.22. However, to obtain the observed level of IPGE and Rh concentrations in our samples, the crystallization of chromite and PGM has necessarily occurred prior to the timing of sulphide liquid segregation, thus limiting the effects of sulphide on the partitioning of these elements into chromite and on the formation of PGM (see Barnes & Lightfoot, 2005). Furthermore, the negative Pd anomaly shown by the PGE patterns of some picrites strongly reflects the late timing of sulphide segregation (see Fig. 2.6a), because Pt is not as depleted in response to the early crystallization of Pt-rich phases, such as Pt–Fe alloys and sperrylite.

The occurrence of native copper in serpentinized olivine phenocrysts from the Emeishan volcanic rocks (Fig. 2.2e) can lead to a Cu enrichment, as was mainly observed for the basalt sample 13-SM-01 whose Cu concentration is above the upper limit of detection (i.e. >2900 ppm Cu; empty square in Fig. 2.14). The observation of native copper as micro-nuggets in small serpentinized veinlets suggests the introduction of post-magmatic, Cu-bearing hydrothermal fluids (Schwarzenbach *et al.*, 2014), thus leading to the addition of this native metal after sulphide segregation. In contrast, Zhang *et al.* (2006b) proposed that native copper can also be derived from a deep mantle source in the form of xenocrysts, promoting its incorporation prior to sulphide segregation.

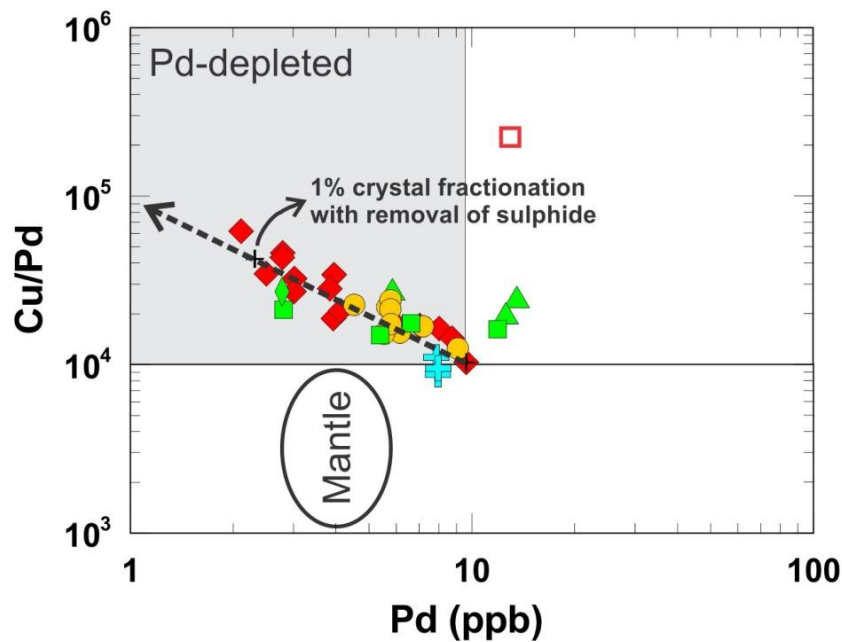


Figure 2.14 Relationships between Cu/Pd ratios and Pd concentrations for the studied samples. Symbols as in Fig. 2.4. The dashed line corresponds to the product of Rayleigh fractional crystallization with removal of sulphide liquid in approximately cotectic proportions from an initial silicate liquid containing 9.63 ppb Pd and 99.2 ppm Cu. The model suggests that most of the samples are depleted in Pd in response to less than 1% of crystal fractionation with removal of sulphide. The diagram also shows that one of the basalt samples is strongly enriched in Cu (empty square; >2900 ppm) owing to the abundance of native copper grains (see Results section: ‘Petrography of picrites and associated rocks’).

2.6.2 THE ENRICHMENT OF IPGE AND RH IN CHROMITES

Recently, researchers seeking to improve their understanding of PGE behaviour during crystal fractionation of sulphide-undersaturated magmas, have focussed their attention on the reason for the presence of these elements in solid solution in chromites (Righter *et al.*, 2004; Brenan *et al.*, 2012; Pagé *et al.*, 2012; Park *et al.*, 2012). The experimental work of

Righter *et al.* (2004) and Brenan *et al.* (2012) indicates that the incorporation of IPGE and Rh in spinel appears to be strongly affected by fO_2 . Brenan *et al.* (2012) demonstrated that with increasing fO_2 , Fe changes its speciation in the melt, from Fe^{2+} to Fe^{3+} , promoting the incorporation of Ir, Ru and Rh into chromite in response to the increase of the degree of inversion of the spinel structure. Moreover, it is known that the solubility of PGE is higher at elevated fO_2 (Borisov & Palme, 2000), increasing their concentration in the melt and their availability for crystallizing chromite. Park *et al.* (2012) provided the first evidence from natural rocks (the Ambae lavas) that IPGE and Rh are more compatible in chromites when they crystallize under oxidized conditions ($fO_2 = QFM + 2.5$). They used the Fe^{3+}/R^{3+} ratio to illustrate the variation of the degree of inversion of the chromite structure, and by extension, the variation of fO_2 in their studied sample suite. Park *et al.* (2012) found that Os, Ru and Rh show positive correlation with Fe^{3+}/R^{3+} , which is interpreted as an increase of the partition coefficient of these three elements as the degree of inversion increases. In our case, only Rh showed positive correlation with Fe^{3+}/R^{3+} , suggesting that this element is more sensitive to the inversion degree variations. Figure 2.15 suggests that the incorporation of Rh in chromite is promoted by the increase of the inversion degree, and that the higher level of Rh concentrations in chromites from the Ambae lavas (Park *et al.*, 2012: ~74 ppb Rh on average; this study: ~23 ppb Rh on average) could be attributed to higher partition coefficients for Rh between chromite and silicate melt under oxidizing conditions, since in our case, tholeiitic magmas derived from a mantle plume are not considered as particularly oxidized (~QFM; Carmichael & Ghiorso, 1986). In contrast to Rh, the lack of correlation between IPGE and Fe^{3+}/R^{3+} suggests that the incorporation of

these elements into chromite is not controlled by the inversion degree, or $f\text{O}_2$, and that the temperature of the magmatic system could have a greater influence than expected on their solubility in melt (Pagé *et al.*, 2012).

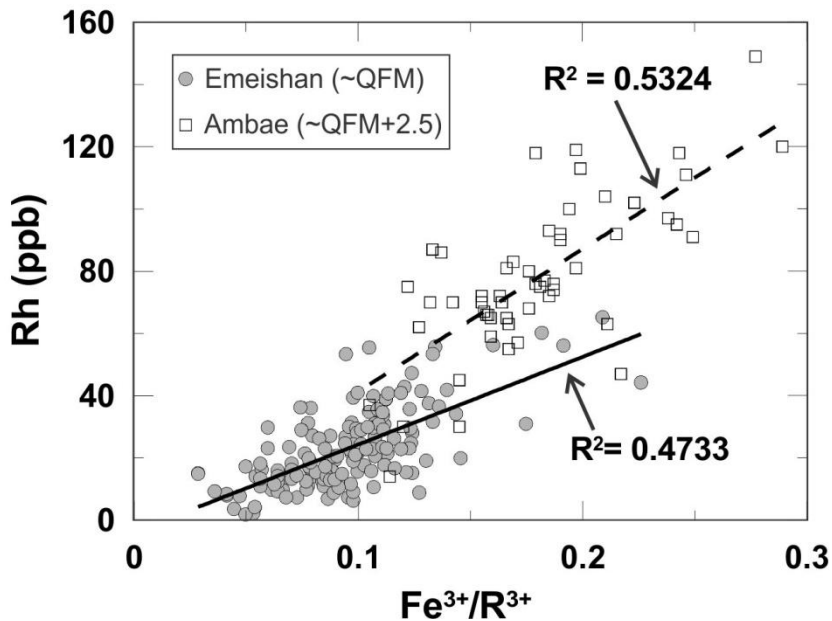


*Figure 2.15 Variation of Rh against $\text{Fe}^{3+}/\text{R}^{3+}$ in chromites from the Emeishan volcanic rocks and the Ambae lavas. Solid line represents linear regression for the Emeishan samples and dashed line represents linear regression for the Ambae samples. The positive correlations shown by the two geochemical parameters suggest that the partition coefficient for Rh between chromite and silicate melt are higher under oxidizing conditions. Compositions of chromites in the Ambae lavas are from Park *et al.* (2012).*

It is well known that high temperature will also increase the solubility of IPGE in the silicate melt (Borisov & Palme, 2000). Because the solubility of Ru rises more rapidly with temperature than for Ir (Borisov & Palme, 2000), Pagé *et al.* (2012) proposed that the preferential incorporation of Ru in komatiitic chromite could be enhanced by high-

temperature conditions. In this case, Ru would be soluble and could not crystallize as PGM, making it more available to enter as solid solutions in chromite, whereas Ir and Os could form PGM earlier during the cooling history (Barnes & Fiorentini, 2008). Since the first eruptive products of the ELIP is expected to be dominated by high-temperature magmas in response to the thermal anomaly caused by the mantle-plume ascension (~ 240°C hotter than the ambient mantle temperature; Li *et al.*, 2012), the incorporation of IPGE into the Emeishan chromites could be explained by high-temperature conditions. Furthermore, the common presence of Os–Ir alloy inclusions in chromites and the higher level of Ru concentration in solid solution (~10 times higher than Os and Ir) could result from the difference in solubility between Ru and both Os and Ir at elevated temperatures (Borisov & Palme, 2000).

It is not clear which of the parameters $f\text{O}_2$ and temperature has the greater influence on the solubility of IPGE and Rh in picritic melts and on the partitioning of these elements into chromite. Two other options should also be considered to explain the concentration of these elements in chromite: (1) the high concentrations of IPGE and Rh in the magma could explain the enrichment of these elements in chromite, as suggested by the enrichment of Os and Ir in chromites from the OPSV rocks (Fig. 2.11); and (2) post-crystallization modification (exsolution or diffusion) could also explain the lack of correlation between IPGE and $\text{Fe}^{3+}/\text{R}^{3+}$, as has been proposed to explain the very low level of IPGE concentration in plutonic chromite (Pagé *et al.*, 2012 and references therein).

2.6.3 CHROMITE-HOSTED PGM: EVIDENCE OF A SYN-CHROMITE CRYSTALLIZATION ORIGIN

There has been a longstanding interest in the presence of chromite-hosted PGM in plutonic rocks, from layered mafic to ultramafic intrusions through to ophiolitic sequences, but chromite-hosted PGM in volcanic rocks have received relatively little attention. Until recently, the evidence for their presence in volcanic chromites was limited to the observation of peaks in time-resolved PGE signals from *in situ* LA-ICP-MS analyses (this study; Fiorentini *et al.*, 2004; Locmelis *et al.*, 2011; Park *et al.* 2012). The observations of peaks of Os–Ir (\pm Ru), and peaks of Pt (\pm IPGE and Rh), suggested the presence of chromite-hosted PGE alloys which were suspected to be Os–Ir and Pt–Fe alloys. Park *et al.* (2012) have already confirmed the presence of Pt–Fe alloy inclusions in chromites from the Ambae lavas by SEM. In addition to confirming the presence of this type of chromite-hosted alloy in our samples, SEM observations have allowed us to provide the first evidence of the presence of laurite (RuS_2) and sperrylite (PtAs_2) in association with volcanic chromites.

Gijbels *et al.* (1974) and Capobianco *et al.* (1994) have proposed that the PGM inclusions have a post-magmatic origin. They have suggested that these PGE-rich phases could form by exsolution of PGE from the spinel structure during the slow cooling of plutonic rocks. Indeed, the very low level of IPGE concentrations in plutonic chromites could support the fact that the formation of PGM may be the result of post-crystallization exsolution (Pagé *et al.*, 2012 and references therein). However, as has also been pointed out

by Park *et al.* (2012), PGM in the lavas cannot be the result of exsolution for two reasons: (1) the lavas cooled rapidly making exsolution unlikely; and (2) Pt is strongly incompatible with chromite (this study; Brenan *et al.*, 2012; Pagé *et al.*, 2012; Park *et al.*, 2012). Furthermore, since IPGM coexist with high levels of IPGE concentrations in volcanic chromites, post-crystallization exsolution can hardly explain the formation of hosted-chromite IPGM. Thus, the low solubility of PGE under specific conditions in the magma (i.e. at low to moderate fO_2 or low temperature; Borisov & Palme, 2000) could be responsible for the precipitation of PGM. In this case, how are PGM trapped within chromite?

Finnigan *et al.* (2008) experimentally demonstrated that the crystallization of chromite, or its re-equilibration with the surrounding melt, can trigger the precipitation of PGM at the chromite–melt interface. They suggest that the preferential incorporation in chromite of the oxidized species Cr³⁺ and Fe³⁺ relative to divalent species is responsible for the creation of a reduced boundary layer at the chromite–melt interface, causing a local reduction of the PGE solubility. According to their experiments, a decrease in fO_2 of 0.12 log units causes a drop in the solubility of Pt and Rh by ~15% and reduces the solubility of both Os and Ru by ~22%. Consequently, even if the host magma is undersaturated in PGM, the change in metal solubility, as a result of a local reduction of fO_2 and a global decrease of temperature, is expected to trigger the formation of these minerals at the margin of precipitating or growing chromite crystals. During further crystal growth, PGM will then be incorporated into chromite as micrometric-sized inclusions.

Our observations are consistent with the experiments carried out by Finnigan *et al.* (2008), providing evidence of a syn-chromite magmatic origin for PGM inclusions. Indeed, the presence of micrometric-sized PGM grains along the margin of chromite crystals (see Fig. 2.13a, b and c) could represent the first stage of the PGM entrapment mechanism which corresponds to the precipitation of PGM particles at the chromite–melt interface, whereas the occurrence of Os–Ir and Pt–Fe alloys trapped within the chromites (see Figs 2.10b and 2.13d) could represent a late stage corresponding to the incorporation of PGM into chromite with further crystal growth.

2.6.4 DETERMINATION OF THE FRACTION OF CHROMITE IN THE EMEISHAN VOLCANIC ROCKS

In order to better understand the contribution of chromite to the PGE whole-rock budgets we estimated in this section the proportion of chromite in our samples. Because chromite is present in very small amounts in volcanic mafic to ultramafic rocks (generally ≤ 1 vol. %), it is difficult to quantify precisely the fraction of chromite present with a traditional optical microscope, even using an area-measurement software. Consequently, it is essential to use whole-rock and mineral chemistry to determine a realistic fraction of chromite. Pagé *et al.* (2012) combined whole-rock Cr with chromite composition to calculate the weight fraction of chromite in chromitites, assuming that all the Cr is contained in chromite. However, to do so for chromite-poor volcanic rocks can result in a significant overestimation of the chromite fraction due to presence of Cr in the large silicate component.

Recently, Li *et al.* (2012) have described the Emeishan picrites as a mixture of olivine phenocrysts crystallized at depth, and the transporting melt, which the quenched product corresponds to the groundmass. According to them, the interaction between olivine phenocrysts and the transporting melt during magma ascent formed Fo-poor rims of olivine phenocrysts. Our microprobe results are consistent with those from Li *et al.* (2012) and further suggest that the olivine microphenocrysts crystallized together with the outermost rims of olivine phenocrysts, and are therefore in equilibrium with the final composition of the transporting melt. Based on a picrite sample containing 42 wt % of olivine phenocrysts, Li *et al.* (2012) estimated that the transporting melt in equilibrium with the average outermost rim composition of olivine phenocrysts is compositionally similar to the basalts that are among the least evolved in the ELIP. In order to estimate the major element compositions of the quenched product of the transporting melts of the studied picrites, and consequently remove from the whole rock the amount of Cr accounted for by the olivine phenocrysts, we subtracted the olivine component from the whole-rock composition as follows:

$$C_{RV} = (C_{WR} - C_{Ol} \times F_{Ol}) / 1 - F_{Ol} \quad (2)$$

where C_{RV} = concentration of the element in the remaining volume, C_{WR} = concentration of the element in whole rock, C_{Ol} = the average concentration of the element in olivine phenocrysts, and F_{Ol} = the weight fraction of olivine phenocrysts. Based on samples that are free of clinopyroxene phenocrysts and serpentinized olivine phenocrysts ($n = 10$), we calculated from equation 2 the average composition of the quenched product of the

transporting melt for both high- and low-Ti picrites, assuming that the amount of transported chromite does not have much influence on the major element content of the calculated compositions. Our results suggest that the quenched product of the transporting melts from both types of picrites contain 7.4 and 7.1 wt % MgO, respectively. Furthermore, by subtracting the olivine component from the picrites (i.e. between 22 and 55 wt % of olivine phenocrysts; see Table 5), we calculated the proportion of whole-rock Cr accounted for by the olivine phenocrysts (F_{Ol}^{Cr}) using the following mass balance equation:

$$F_{Ol}^{Cr} = (C_{Ol}^{Cr} \times F_{Ol}) / C_{WR}^{Cr} \quad (3)$$

where C_{Ol}^{Cr} = the average Cr content of olivine phenocrysts, F_{Ol} = the weight fraction of olivine phenocrysts, and C_{WR}^{Cr} = the Cr content of the whole rock. Our results suggest that the proportion of whole-rock Cr removed by subtracting the olivine component ranges from 0.03 to 0.17.

Because the quenched products of the transporting melts appear to be compositionally similar to the Emeishan flood basalts, it is possible to estimate the Cr content accounted for by the silicate components in the remaining volumes (i.e. free of olivine phenocrysts). We used the trend of the basalts in the diagram of MgO vs. Cr (Fig. 2.5b) as a reference for the Cr content of the quenched product of the transporting melts. For remaining volumes containing between 4.8 and 10.9 wt % MgO, the linear equation determined from this trend allowed us to estimate that the Cr content accounted for by the silicate components ranges from 172 to 690 ppm (Table 5). We then reused equation 2 to estimate the weight fraction of chromite microphenocrysts in the picrite samples by

incrementally subtracting the chromite component from the remaining volumes until the Cr content determined from the linear equation was reached. Our results are expressed as weight percent of chromite in Table 5 (see method 1).

Based on natural volcanic rocks and experimental glasses containing more than 6 wt % MgO, Roeder *et al.* (2006) demonstrated that volcanic rocks containing more than 0.02 vol. % spinel (Cr-spinel and chromite) tend to have olivine to spinel ratios of approximately 100:1. They conclude that this ratio corresponds approximately to the cotectic proportions of olivine and spinel. However, Roeder *et al.* (2006) suggest that rocks containing added olivine phenocrysts should always lie above the cotectic ratio of olivine to spinel. As shown in the diagram of volume percent olivine phenocryst vs. volume percent chromite, (Fig. 2.16), the olivine to spinel ratios of the picrites are generally above the 100:1 line when the fraction of chromite is determined according to the method previously explained (method 1, circles in Fig. 2.16). This observation is consistent with the prediction of Roeder *et al.* (2006) in considering the presence of added olivine phenocrysts in the Emeishan picrites. On the other hand, when the fraction of chromite is determined assuming that all the Cr is contained in chromite (method 2, squares in Fig. 2.16; Table 5), the ratios are below the 100:1 line, and therefore do not allow us to reproduce the predicted proportions of olivine and spinel. Thus, it is concluded that the chemical method based on the subtraction of silicate components containing Cr provides a more realistic estimation of the fraction of chromite, which allowed us to obtain olivine to spinel ratios close to those predicted in rocks containing added olivine phenocrysts.

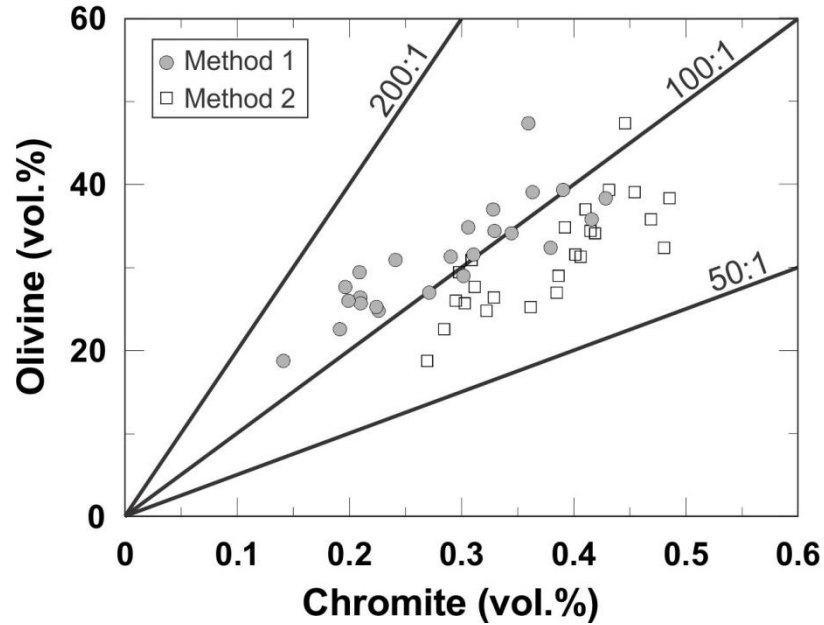


Figure 2.16 Volume percent of olivine phenocryst vs. volume percent of chromite for the picrite samples. The fraction of chromite was determined according to two chemical methods. Method 1 (filled circles) is based on the subtraction of the silicate components containing Cr (see text for details), and method 2 (empty squares) is based on the assumption that all the Cr is contained in chromite. The diagram suggests that method 1 provides a more precise estimation of the fraction of chromite according to the olivine to spinel ratios in rocks containing added olivine phenocrysts (i.e. between 300:1 and 100:1; see Roeder et al., 2006).

Table 5: Weight and volume percent chromite present in each sample

Series	Sample	MgO _{WR} ^a	Method 1 (as described in the text)			Method 2 ^f			
			Ol (vol. %) ^b	Cpx (vol. %) ^b	Ol (wt %) ^c	Chr (wt %) ^d	Chr (vol. %) ^e	Chr (wt %) ^d	
High-Ti	13-DJ-03	30.45	47.4		55.0 (9.14)	0.58 (542)	0.36	0.72	0.45
	13-DJ-04	21.43	27.0	0.5	31.3 (9.78)	0.44 (599)	0.27	0.62	0.38
	13-DJ-05	21.99	34.4		39.9 (6.06)	0.53 (278)	0.33	0.67	0.41
	13-DJ-06	21.65	29.0	0.6	33.7 (8.98)	0.48 (529)	0.30	0.62	0.39
	13-DJ-08	22.36	31.6	0.2	36.7 (8.10)	0.50 (454)	0.31	0.65	0.40
	13-DJ-09	24.67	38.3		44.5 (7.01)	0.69 (361)	0.43	0.78	0.49
	13-SM-02	23.32	35.8	1.2	41.6 (6.99)	0.67 (359)	0.42	0.75	0.47
	13-SM-03	23.85	34.1	1.9	39.6 (8.36)	0.55 (476)	0.34	0.67	0.42
	13-JC-01	20.60	30.9	2.5	35.9 (6.40)	0.39 (308)	0.24	0.50	0.31
	13-JC-02	23.35	32.4		37.6 (8.92)	0.61 (524)	0.38	0.77	0.48
	13-JC-03	23.99	31.3	2.7	36.3 (10.86)	0.47 (690)	0.29	0.65	0.41
	13-JC-04	20.46	29.4	1.8	34.1 (7.09)	0.34 (367)	0.21	0.48	0.30
	13-JC-06	20.64	25.3	4.9	29.4 (10.47)	0.36 (656)	0.22	0.58	0.36
	13-JC-07	20.26	26.0	1.6	30.2 (8.63)	0.32 (499)	0.20	0.47	0.29
	13-ET-02 ^h	21.86				0.49		0.66	0.41
	13-ET-03 ^h	22.22				0.48		0.64	0.40
	13-ET-04 ^h	26.59				0.47		0.63	0.39
	13-DJ-02	5.93	0		0	0.05 (274)	0.03	0.15	0.09

Table 5: Continued

Series	Sample	MgO _{WR} ^a	Method 1 (as described in the text)			Method 2 ^f		
			Ol (vol. %) ^b	Cpx (vol. %) ^b	Ol (wt %) ^c	Chr (wt %) ^d	Chr (vol. %) ^e	Chr (wt %) ^d
Low-Ti	13-DL-02	19.70	24.8		28.8 (8.02)	0.36 (447)	0.23	0.52
	13-DL-03	20.68	26.4		30.6 (9.58)	0.34 (581)	0.21	0.53
	13-DL-04 ^g	15.82	27.7		32.2 (9.71)	0.32 (591)	0.20	0.50
	13-DL-06	20.15	25.7		29.8 (8.34)	0.34 (475)	0.21	0.49
	13-BC-02	24.24	35.8		41.6 (5.58)	0.49 (238)	0.31	0.63
	13-BC-04	25.78	39.1	0.4	45.4 (6.00)	0.59 (274)	0.36	0.73
	13-BC-05	24.11	37		42.9 (4.80)	0.53 (172)	0.33	0.66
	13-BC-06	18.87	22.6		26.2 (7.98)	0.31 (444)	0.19	0.46
	13-BC-07	24.55	39.3		45.6 (5.52)	0.63 (233)	0.39	0.69

^a MgO_{WR} = MgO content (wt %) in whole-rock.^b Ol, olivine phenocrysts; Cpx, clinopyroxene phenocrysts; the volume percent of olivine and clinopyroxene phenocrysts was estimated using an area-measurement software.^c Ol wt % = Ol vol. % / (d_{pic} / d_{ol}); d_{pic}, density of picrite (~2.8); d_{ol}, density of olivine (~3.25); numbers in brackets represent the MgO content (wt %) in the remaining volumes after subtracting the olivine component from the whole-rock compositions (see C_{RV} in equation 2).^d Chr, chromite; numbers in brackets represent the predicted Cr content (ppm) in the remaining volumes (see linear equation in Fig. 2.5b).^e Chr vol. % = Chr wt % * (d_{pic} / d_{chr}); d_{chr}, density of chromite (~4.5).^f See equation 2 in Pagé *et al.* (2012); this method is based on the assumption that all the Cr is present in chromite.^g Olivine phenocrysts in this sample are strongly serpentinized (see Electronic Appendix 2).^h The weight percent of chromite in these samples was estimated according to the average proportion of the whole-rock Cr accounted for by the chromite in the picrite samples (~0.75; see equation 3).

2.6.5 PARTITION COEFFICIENTS FOR IPGE AND RH BETWEEN CHROMITE AND PICRITE, AND MASS BALANCE CALCULATIONS

Although the Emeishan picrites are defined as a mixture of transported phenocrysts (e.g. olivine and chromite) and the transporting melt, many authors suggest that they represent compositions close to the primitive melts of the ELIP (e.g. Chung & Jahn, 1995; Ali *et al.*, 2005; Hanski *et al.*, 2010; Zhou *et al.*, 2013). Because chromite appears to have crystallized in equilibrium with the core of the olivine phenocrysts, and therefore in equilibrium with compositions close to the primitive melt, we calculated the empirical partition coefficients (D) for IPGE and Rh between chromite and picrite using our measured IPGE and Rh concentrations in chromite and whole rock. Our results are as follows: $D_{Os}^{Chr/Pic} = 5\text{--}33$, $D_{Ir}^{Chr/Pic} = 7\text{--}37$, $D_{Ru}^{Chr/Pic} = 48\text{--}178$ and $D_{Rh}^{Chr/Pic} = 14\text{--}136$.

As shown in Figure 2.17, the values of the low end of our range are similar to those published by Pagé *et al.* (2012) for Os, Ir and Ru after performing *in situ* LA-ICP-MS analyses on chromites from a sulphide-undersaturated komatiite from Alexo in the Abitibi greenstone belt. By using a similar approach, Park *et al.* (2012) obtained much higher partition coefficients for Ir, Ru and Rh into chromites from the oxidized Ambae lavas than those determined in this study (~1 order of magnitude higher). Despite the fact that the partitioning of IPGE and Rh into the chromite seems to be variable in natural rocks, the compatibility of these elements with the chromite is still similar when the partition coefficients are determined using *in situ* analyses (i.e. $D_{Ru}^{Chr/Pic} > D_{Rh}^{Chr/Pic} > D_{Ir}^{Chr/Pic} \geq D_{Os}^{Chr/Pic}$). In contrast, the results obtained by Puchtel & Humayun (2001) strongly

suggested that the compatibility of Os, Ir and Ru with chromites from a komatiitic olivine-chromite cumulate in the Vetryny belt (Baltic Shield) is comparable with each other. However, because these values were determined from chromite concentrate analyses, these results probably reflect the presence of chromite-hosted PGM such as Os–Ir alloys within the chromite from their concentrates.

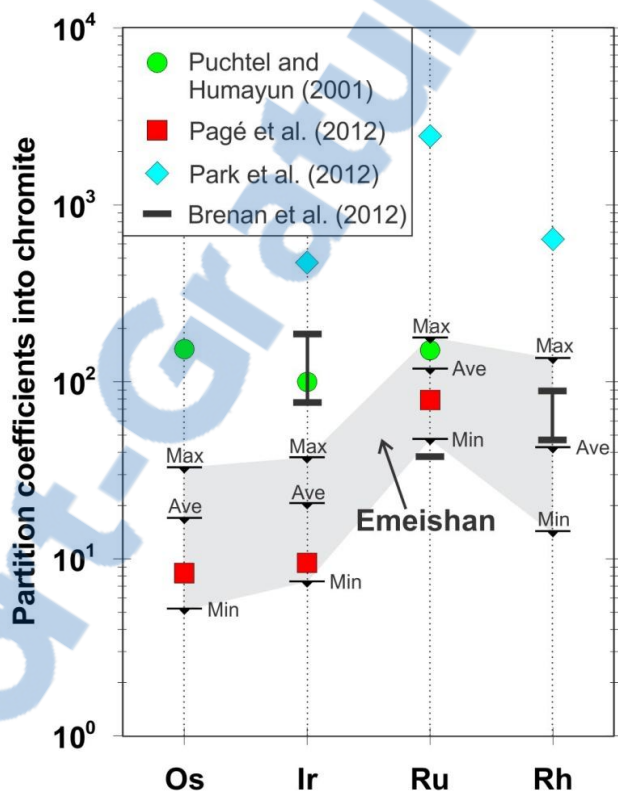


Figure 2.17 Partition coefficients for IPGE and Rh between chromite and silicate melt established empirically from natural rocks and from experimental petrology. The grey field represents the range of values determined in this study (our results are also given in Table 6). Values from other volcanic rocks, including a komatiitic olivine–chromite cumulate from the Venetry belt, a komatiite from Alexo in the Abitibi greenstone belt and lavas from the Ambae volcano are from Puchtel & Humayun (2001), Pagé et al. (2012) and Park et al. (2012), respectively. Experimental results correspond to the range obtained from experiments conducted at 1400 to 1500 °C and ~IW + 6.2 to IW + 7.2 (~QFM + 2.4 to QFM + 3.5) by Brenan et al. (2012).

Partition coefficients for IPGE and Rh between spinel (hercynite, magnetite, Cr-bearing Fe-rich spinel and chromite) and silicate melt have also been reported by some experimentalists (Capobianco & Drake, 1990; Capobianco *et al.*, 1994; Righter *et al.*, 2004; Brenan *et al.*, 2012, respectively). However, the high $f\text{O}_2$ and high temperatures under which most of the experiments were conducted do not seem to reflect terrestrial conditions, and the composition of spinel in these experiments generally differs from the composition of a typical chromite. Empirical results determined from natural rocks are compared here only with the recent partition coefficients from experimental work run at temperatures similar to picrite liquidus temperatures (1400–1500 °C) and $f\text{O}_2$ at a little above QFM (+2.4 to +3.5). Our Rh values are similar to the experimental values obtained under these conditions, our Ir values are slightly lower and our Ru values are slightly higher than the single Ru value available (see Fig. 2.17 and Table 6). Given the difficulty of the experiments and our uncertainties in estimating the composition of the liquid we feel that the difference between the experimental results and ours is reasonable.

Table 6: Empirical partition coefficients for IPGE and Rh into chromite

Rock type	Os	Ir	Ru	Rh
<i>Empirical determination from natural rocks</i>				
Emeishan picrites				
HT pic ^a	5–18	7–22	48–173	26–136
LT pic ^b	11–33	19–37	81–178	14–59
Ave. ^c	17 (49)	21 (38)	119 (28)	43 (57)
Komatiitic olivine-chromite cumulate (Vetreny) ^d	153	100	151	
Alexo komatiite (Abitibi greenstone belt) ^d	8.3	9.5	79.0	
Ambae lavas (Vanuatu) ^d		472	2448	641
<i>Experimental determination</i>				
Chromite /melt ^e		77–187	38	47–89

The results obtained from the Emeishan picrites are based on the median values of IPGE and Rh concentrations in chromites for each sample.

^a HT pic, high-Ti picrites (n = 14).

^b LT pic, low-Ti picrites (n = 9).

^c Numbers in brackets represent one standard deviation (1σ) expressed in relative percent to the average.

^d Empirical partition coefficients determined from other volcanic rocks are sourced from Puchtel & Humayun (2001), Pagé *et al.* (2012) and Park *et al.* (2012), respectively.

^e Experimental results correspond to the range obtained from experiments conducted at 1400 to 1500 °C and ~IW + 6.2 to IW + 7.2 (~QFM + 2.4 to QFM + 3.5) by Brenan *et al.* (2012).

Mass balance calculations can be used in order to evaluate the role of chromite in the fractionation of PGE. By calculating the proportion of IPGE in whole rock that could be accounted for in solid solution by the chromite, Pagé *et al.* (2012) indicated that ~100% of the whole-rock Ru budget, but less than 20% of the whole-rock Os and Ir budgets, could be accounted for by the chromite in the Alexo komatiite. They proposed that Os and Ir require the presence of some other phase(s), possibly IPGM, to account for their mass balance. Similar conclusions have also been proposed for Australian komatiites (Barnes & Fiorentini, 2008; Fiorentini *et al.*, 2008).

By reusing equation 3, we calculated the proportion of IPGE and Rh accounted for by the chromite. Our results indicate that the chromites from the picrites control up to 84% of the whole-rock Ru budget, but less than 49% of the whole-rock Rh budget and less than 22% and 20% of the whole-rock Ir and Os budgets, respectively (Figs 2.18a and b), whereas the chromites from the OPSV rocks and the aphyric basalt tend to account for a lesser proportion of the whole-rock IPGE and Rh budgets (Fig. 2.18c and d). The presence of chromite-hosted Os–Ir alloys could explain the remaining proportion of Os and Ir in the Emeishan volcanic rocks, as suggested by Pagé *et al.* (2012) for the Alexo komaiite. However, this hypothesis cannot explain the remaining proportions of Ru and Rh which necessarily require the occurrence of other phases enriched in these elements, such as laurite for Ru, to account for their mass balance. Furthermore, if we assume that IPGE and Rh are moderately compatible with olivine as suggested by Brenan *et al.* (2003, 2005), it is possible that olivine phenocrysts play a role in controlling these elements.

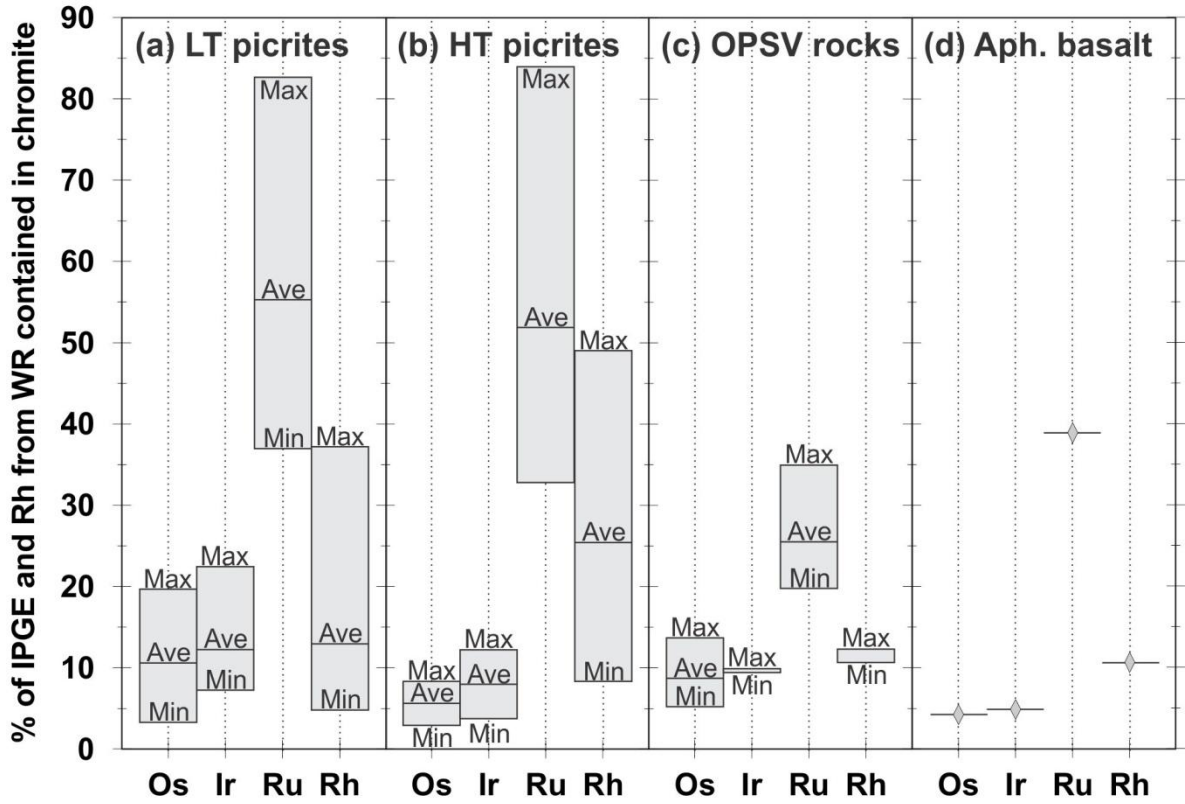


Figure 2.18 Diagrams of mass balance calculations (see equation 3 in text) showing the proportion of whole-rock (WR) IPGE and Rh accounted for by the chromite in (a) the low- and (b) the high-Ti picrites; (c) the OPSV rocks; and (d) the aphyric basalt. For the calculations we used the median values of the IPGE and Rh concentrations in chromites for each sample. Our results suggest that the presence of PGM is required to account for the mass balance of IPGE and Rh. HT, high-Ti; LT, low-Ti; OPSV, olivine-phyric subvolcanic rocks; Aph., aphyric.

2.6.6 THE EFFECTS OF CHROMITE CRYSTALLIZATION ON IPGE AND RH CONCENTRATIONS IN WHOLE ROCK: A MODEL FOR THE ELIP

In this section, we report on our modelling of two processes that might be responsible for the IPGE and Rh variations observed in the Emeishan volcanic rocks: (1) the crystallization

of olivine and chromite in cotectic proportions (step 1); and (2) the late sulphide liquid segregation (step 2). The main purpose of this modelling is to investigate whether or not the removal of chromite from a picritic primitive magma can cause the negative Ru anomaly observed from the PGE patterns of the Emeishan flood basalts (see Fig. 2.6c). Furthermore, the modelling also allows us to check whether the removal of both olivine+chromite and sulphide liquid is enough to deplete the magma sufficiently in order to obtain the observed level of IPGE and Rh concentrations in the basalts.

Step 1 (Fig. 2.19) is based on the removal of olivine and chromite in approximately cotectic proportions (i.e. olivine to chromite weight ratio of ~100:1.5, equivalent to 100:1 volume ratio; see Roeder *et al.*, 2006) from a primitive magma of the ELIP with ~21 wt % MgO and 1.96 ppb Ru (see Li *et al.*, 2012). Here, we used our average partition coefficient for Ru between chromite and picrite ($D_{Ru}^{Chr/Pic} = 119$; Table 6) and the partition coefficient for IPGE and Rh between olivine and melt experimentally determined by Brenan *et al.* (2003, 2005) ($D_{IPGE-Rh}^{Ol/Melt} \sim 2$) in order to model the concentration of Ru in the silicate liquid, assuming that this element is incompatible with the other silicates. Step 1 shows that the co-crystallization of olivine and chromite could produce a positive correlation between Ru and MgO, and by extension between Ru and Cr as observed for many sulphide-poor mafic to ultramafic rocks (Pagé *et al.*, 2002 and references therein), including those from the ELIP. However, it appears that the removal of both olivine and chromite is not sufficient to explain the low level of Ru concentration observed in most of the Emeishan flood basalts, which should require another depletion process.

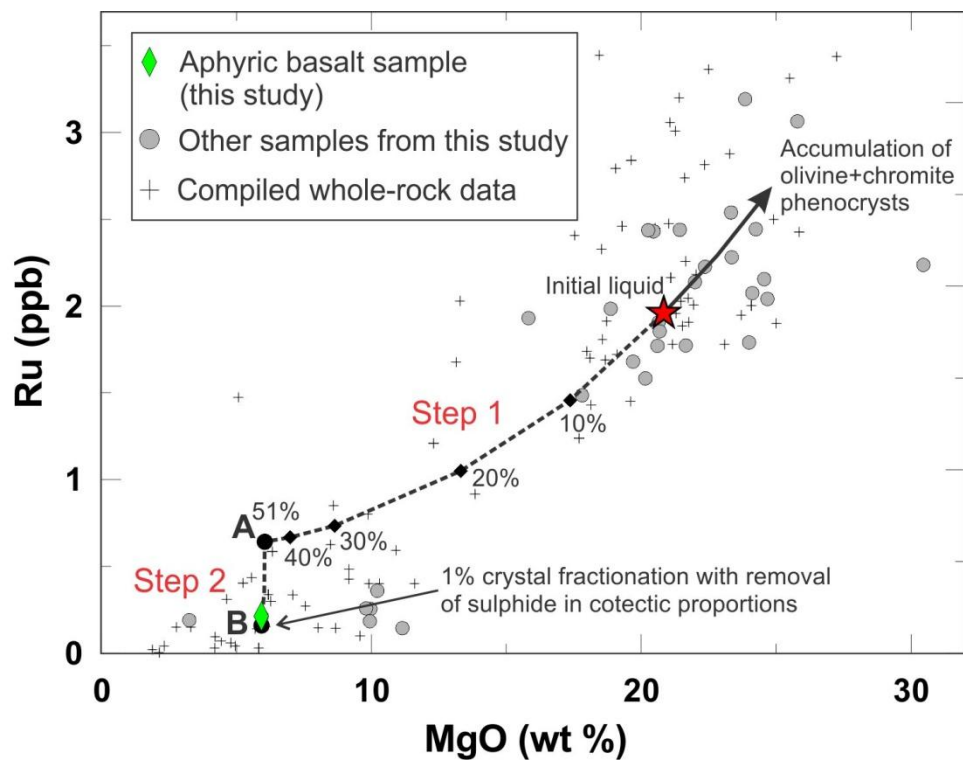


Figure 2.19 Modelling of the combined effects of (step 1) olivine and chromite crystallization (olivine to chromite weight ratio of ~100:1.5, equivalent to 100:1 volume ratio; see Roeder et al., 2006) and (step 2) the late timing of sulphide liquid segregation on Ru concentrations in the silicate liquid. The dashed lines illustrate the evolution path of the melt composition during the fractional crystallization. Ruthenium concentrations in the fractionated liquid were calculated according to Rayleigh fractionation (see equation 1 in text), whereas MgO contents were calculated using Pele 7.07. The initial liquid used in step 1 is based on the composition of the primitive magma of the ELIP determined by Li et al. (2012) as ~21 wt % MgO and 1.96 ppb Ru. Step 2 adds 1% of crystal fractionation with removal of sulphide liquid in cotectic proportions from a fractionated liquid produced by ~51% of crystal fractionation from step 1 (point A) in order to approximate the composition of the aphyric basalt (diamond). Point B corresponds to the predicted final composition of the liquid. Compiled data for other Emeishan picrites and flood basalts (small crosses) are from Zhang et al. (2005), Li et al. (2012), Bai et al. (2013) and Li et al. (2014). Our results suggest that the combined effects of the olivine and chromite crystallization and the late timing of sulphide liquid segregation can explain the low level of Ru in the aphyric basalt, and by extension, in most of the Emeishan basalts. The thick solid arrow represents the expected path of the accumulation of olivine and chromite phenocrysts.

Step 2 (Fig. 2.19) is based on ~1% of crystal fractionation with removal of sulphide liquid in approximately cotectic proportions (see F_{Sul} in equation 1) from a fractionated liquid produced by ~51% of crystallization (point A in Fig. 2.19). Here, we assumed a partition coefficient for PGE into sulphide of 50,000, and we considered that the composition of the aphyric basalt (diamond in Fig. 2.19), which would be produced by ~52% of crystal fractionation, corresponds to the composition of the final liquid. Step 2 shows that the combined effects of 51% of crystal fractionation of the silicate liquid with removal of chromite and olivine (+clinopyroxene+plagioclase), followed by 1% of fractionation with removal of sulphide liquid, reduce the Ru concentration in the silicate liquid by a factor of 0.08 (point B in Fig. 2.19), which is sufficient to achieve the low level of Ru concentration in the aphyric basalt.

Steps 1 and 2 were also applied to Os, Ir and Rh in order to predict the primitive mantle-normalized IPGE–Rh patterns corresponding to compositions of the fractionated liquid at points A and B in Figure 2.19 (the concentrations of Ir and Rh in the initial liquid are also from Li *et al.* (2012); 1.32 ppb Ir and 0.65 ppb Rh). We considered that the concentration of Os in the initial liquid is the same as for Ir, owing to similar concentrations of both elements in the primitive mantle (McDonough & Sun, 1995; Barnes & Maier, 1999), and to comparable bulk partition coefficients for them into the mantle (Barnes & Lightfoot, 2005 and references therein). Figure 2.20 shows that the removal of chromite from the primitive magma tends to create the negative Ru anomaly in response to the preferential incorporation of this element into chromite relative to Ir and Rh (composition at point A, ~51% of fractionation). It also shows that the late timing of sulphide liquid

segregation is critical for the depletion of IPGE and Rh (composition at point B, ~52% of fractionation). However, it does not match the depletion of Ir observed in the most evolved basalts relative to those that are least evolved; this could possibly be caused by the removal of IPGM enriched in this element. On the other hand, the role in the fractionation of IPGE and Rh played by the PGM that we observed in our samples does not appear to be critical to explain most of the whole-rock IPGE and Rh signatures, provided that IPGE and Rh are compatible with olivine.

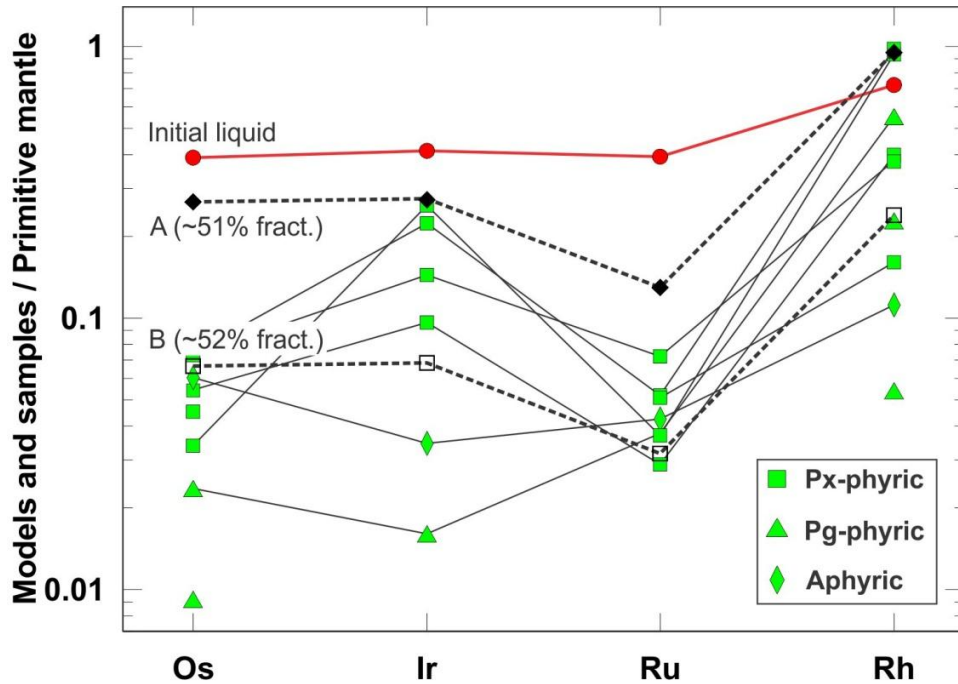


Figure 2.20 Primitive mantle-normalized IPGE–Rh patterns for the studied flood basalts and for the predicted liquid from steps 1 and 2 of the numerical modelling (A and B refer to composition at points A and B in Fig. 2.19). The composition of the initial liquid in terms of Ir and Rh corresponds to the composition of the primitive magma of the ELIP determined by Li *et al.* (2012) as 1.32 ppb Ir and 0.65 ppb Rh. The concentration of Os in the initial liquid is set to be equivalent to Ir. Our results suggest that the negative Ru anomaly shown by the pyroxene-phyric basalts is created by the preferential incorporation of Ru into chromite. The primitive mantle values are from McDonough & Sun (1995).

In summary, the chromite crystallization is responsible for the development of negative Ru anomalies observed in the PGE patterns of the flood basalts in response to the preferential incorporation of Ru into the chromite structure. However, the IPGE and Rh depletion during crystal fractionation is too large to be accounted for by chromite crystallization alone. The other phases controlling these elements could be olivine and/or PGM. Control by olivine may be possible if IPGE and Rh are moderately compatible with olivine, in which case the PGM have little influence. However, if the partition coefficients into olivine are lower, the role of PGM may be important. In order to explain the depletion of all the PGE in most of the Emeishan flood basalts, we suggest base metal sulphide segregation occurred late in the crystallization history of the lavas.

2.7 CONCLUSIONS

In addition to new whole-rock PGE data and primary mineral compositions for the Emeishan volcanic rocks, including picritic and basaltic samples from the high- and low-Ti magmatic series, we have reported in this paper the analytical results of IPGE and Rh concentrations in chromites determined by *in situ* LA-ICP-MS. Our results show that the Emeishan chromites contain uniform IPGE and Rh concentrations ranging from 8 to 151 ppb Os, 6 to 56 ppb Ir, 52 to 448 ppb Ru, and 2 to 93 ppb Rh (Table 3 and Electronic Appendix 4). Moreover, the observation of peaks in time-resolved PGE spectra from the LA-ICP-MS analyses (Fig. 2.10b) suggests the presence of micrometric-sized PGM grains included into chromite, which was then confirmed by SEM observations. In addition to the

presence of chromite-hosted Os–Ir and Pt–Fe alloys suggested by the PGE spectra from the *in situ* analyses of chromites, semi-quantitative EDS analyses of PGM also revealed the occurrence of laurite and sperrylite (Fig. 2.13) at the margin of chromite crystals, reinforcing the mechanism of PGM crystallization proposed by Finnigan *et al.* (2008) and by Brenan *et al.* (2012).

As also pointed out by Park *et al.* (2012), Rh enrichment in chromite seems to be promoted by the increase of the inversion degree of the chromite structure, and by extension by the increase of $f\text{O}_2$, as suggested by the positive correlation observed between $\text{Fe}^{3+}/\text{R}^{3+}$ and Rh in chromites (Fig. 2.15). On the other hand, it appears that other parameters would need to be involved to explain the incorporation of Os, Ir and Ru in the chromite structure, such as a high temperature of the magmas, and/or a greater concentration of PGE in the magmas. In the case of chromite-hosted PGM, petrological and geochemical evidence supports a syn-chromite crystallization (or re-equilibration) origin as suggested by Finnigan *et al.* (2008), rather than a post-chromite crystallization origin, which implies exsolution of PGE initially in solid solutions, as previously proposed for plutonic spinels by Gijbels *et al.* (1974) and Capobianco *et al.* (1994).

Empirical determination of partition coefficients for IPGE and Rh between chromite and picrite reveals that Ru is the most compatible PGE with chromite followed by Rh, Ir and Os (Table 6; Fig. 2.17). The results are as follows: $D_{\text{Ru}}^{\text{Chr}/\text{Pic}} = 48\text{--}178$, $D_{\text{Rh}}^{\text{Chr}/\text{Pic}} = 14\text{--}136$, $D_{\text{Ir}}^{\text{Chr}/\text{Pic}} = 7\text{--}37$ and $D_{\text{Os}}^{\text{Chr}/\text{Pic}} = 5\text{--}33$. Our mass balance calculations suggest that chromites from the picrite samples control up to 84% of the whole-rock Ru budget, but less

than 49% of the whole-rock Rh budget and less than 22 and 20% of the whole-rock Ir and Os budgets, respectively. The chromite from the OPSV rocks and the aphyric basalt tend to account for a lesser proportion of the whole-rock IPGE and Rh budgets than the chromites from the picrites. As also proposed by Pagé *et al.* (2012) for the Alexo komatiite, the presence of PGM, such as laurite, Os–Ir alloys, Pt–Fe alloys (containing Rh), and possibly other non-identified phase(s) in the case of the Emeishan volcanic rocks, may be required to account for the IPGE and Rh mass balance. However, if we assume that IPGE and Rh are compatible with olivine, this latter phase may also play a role in controlling these elements.

Numerical modelling of the IPGE and Rh distribution suggests that chromite, olivine and PGM all contributed to the fractionation of these elements during the early stages of crystal fractionation of the Emeishan picritic magmas (Figs 2.19 and 2.20). In addition, we conclude that the crystallization of chromite causes the Ru anomalies observed in the PGE patterns of the basalts in response to the preferential incorporation of Ru into the chromite structure. On the other hand, the relative importance of olivine and PGM in controlling IPGE and Rh remains to be established, owing to the uncertainty of the compatibility of these elements with olivine and to the unknown number and size of PGM in our samples. Furthermore, we suggest that the depletion of all the PGE in most of the flood basalts is due to late sulphide liquid segregation.

2.8 ACKNOWLEDGEMENTS

This work is the principal part of the MSc thesis of Jean-Philippe Arguin. Dany Savard and Sadia Mehdi are thanked for their assistance and advice during whole-rock PGE and LA-ICP-MS analysis. Travelling and field work in China were supported by an Open Research Fund of the State Key Laboratory of Ore Deposit Geochemistry of China: SKLODG grant #201204 to Philippe Pagé. Other expenses were supported by the Canadian Research Chair in Magmatic Metallogeny.

2.9 REFERENCES

- Ali, J. R., Thompson, G. M., Zhou, M.-F. & Song, X.-Y., 2005. Emeishan large igneous province, SW China. *Lithos* 79, 475-489.
- Argiorgitis, G. & Wolf, R., 1978. Aspects of osmium, ruthenium and iridium contents in some Greek chromites. *Chemical Geology* 23, 267-272.
- Augé, T., 1985. Platinum-group-mineral inclusions in ophiolitic chromitite from the Vourinos Complex, Greece. *Canadian Mineralogist* 23, 163-171.
- Augé, T. 1988. Platinum-group minerals in the Tiebaghi and Vourinos ophiolitic complexes: Genetic implications. *Canadian Mineralogist* 26, 177-192.
- Bai, M., Zhong, H., Zhu, W., Bai, Z. & He, D., 2013. Platinum-Group Element Geochemical Characteristics of the Picrites and High-Ti Basalts in the Binchuan Area, Yunnan Province. *Acta Geologica Sinica* 87, 158-840.

- Barnes, S.-J., Naldrett, A. J. & Gorton, M. P., 1985. The origin of the fractionation of Platinum-Group Elements in terrestrial magmas. *Chemical Geology* 53, 303-323.
- Barnes, S.-J. & Maier, W. D., 1999. The fractionation of Ni, Cu and the noble metals in silicate and sulphide liquids. *Geological Association of Canada Short Course Notes* 13, 69-106.
- Barnes, S.-J. & Lightfoot, P. C., 2005. Formation of magmatic nickel sulfide deposits and processes affecting their copper and platinum group element contents. *Society of Economic Geologist 100th anniversary volume*, 179-213.
- Barnes, S.-J., Prichard, H. M., Cox, R. A., Fisher, P. C. & Godel, B., 2008. The location of the chalcophile and siderophile elements in platinum-group element ore deposits (a textural, microbeam and whole rock geochemical study): implications for the formation of the deposits. *Chemical Geology* 248, 295-317.
- Barnes, S.-J., Pagé, P., Zientek, M. L., Prichard, H. M. & Fisher, P. C., 2015. Chalcophile and siderophile element distributions in the ultramafic series of the Stillwater Complex, Montana, U.S.A.. *Mineralium Deposita*, Accepted.
- Barnes, S. J. & Roeder, P. L., 2001. The range of spinel compositions in terrestrial mafic and ultramafic rocks. *Journal of Petrology* 42, 2279-2302.
- Barnes, S. J. & Fiorentini, M. L., 2008. Iridium, ruthenium and rhodium in komatiite: Evidence for iridium alloy saturation. *Chemical Geology* 257, 44-58.
- Bellieni, G., Comin-Chiaromonti, P., Marques, L. S., Melfi, A. J., Piccirillo, E. M., Nardy, A. J. R. & Roisenberg, A., 1984. High- and low-TiO₂ flood basalts from the Paraná

- plateau (Brazil): petrology and geochemical aspects bearing on their mantle origin. *Neues Jahrbuch für Mineralogie – Abhandlungen* 150, 273-306.
- Borisov, A. & Palme, H., 2000. Solubilities of noble metals in Fe-containing silicate melts as derived from experiments in Fe-free systems. *American Mineralogist* 85, 1665-1673.
- Brenan, J. M., McDonough, W. F. & Dalpé, C., 2003. Experimental constraints on the partitioning of rhenium and some platinum-group elements between olivine and silicate melt. *Earth and Planetary Science Letters* 212, 135-150.
- Brenan, J. M., McDonough, W. F. & Ash, R., 2005. An experimental study of the solubility and partitioning of iridium, osmium and gold between olivine and silicate melt. *Earth and Planetary Science Letters* 237, 855-872.
- Brenan, J. M., Finnigan, C. F., McDonough, W. F. & Homolova, V., 2012. Experimental constraints on the partitioning of Ru, Rh, Ir, Pt and Pd between chromite and silicate melt: The importance of ferric iron. *Chemical Geology* 302-303, 16-32.
- Campbell, I. H. & Griffiths, R. W., 1990. Implications of mantle plume structure for the evolution of flood basalts. *Earth and Planetary Science Letters* 99, 79-93.
- Campbell, I. H. & Davies, G. F., 2006. Do mantle plumes exist?. *Episodes* 29, 162-168.
- Campbell, I. H., 2007. Testing the plume theory. *Chemical Geology* 241, 153-176.
- Capobianco, C. J. & Drake, M. J., 1990. Partitioning of ruthenium, rhodium, and palladium between spinel and silicate melt and implications for platinum group element fractionation trends. *Geochimica et Cosmochimica Acta* 54, 869-874.

- Capobianco, C. J., Hervig, R. L. & Drake, M. J., 1994. Experiments on crystal/liquid partitioning of Ru, Rh and Pd for magnetite and hematite solid solutions crystallized from silicate melt. *Chemical Geology* 113, 23-43.
- Carmichael, I. S. E. & Ghioso, M. S., 1986. Oxidation-reduction relations in basic magma: a case for homogeneous equilibria. *Earth and Planetary Science Letters* 78, 200-210.
- Chung, S.-L. & Jahn, B.-m., 1995. Plume-lithosphere interaction in generation of the Emeishan flood basalts at the Permian-Triassic boundary. *Geology* 23, 889-892.
- Crocket, J. H., 2002. Platinum-group elements in basalts from Maui, Hawaii: low abundances in alkali basalts. *The Canadian Mineralogist* 40, 595-609.
- Dare, S. A. S., Barnes, S.-J. & Prichard, H. M., 2010. The distribution of platinum group elements (PGE) and other chalcophile elements among sulfides from the Creighton Ni-Cu-PGE sulfide deposit, Sudbury, Canada, and the origin of palladium in pentlandite. *Mineralium Deposita* 45, 765-793.
- Finnigan, C. S., Brenan, J. M., Mungall, J. E. & McDonough, W. F., 2008. Experiments and model bearing on the role of chromite as a collector of platinum group minerals by local reduction. *Journal of Petrology* 49, 1647-1665.
- Fiorentini, M. L., Stone, W. E., Beresford, S. W. & Barley, M. E., 2004. Platinum-group element alloy inclusions in chromites from Archaean mafic-ultramafic units: evidence from the Abitibi and the Agnew-Wiluna Greenstone Belts. *Mineralogy and Petrology* 82, 341-355.

- Fiorentini, M. L., Beresford, S. W. & Barley, M. E., 2008. Ruthenium-chromium variation: a new lithogeochemical tool in the exploration for komatiite-hosted Ni-Cu-(PGE) deposits. *Economic Geology* 103, 431-437.
- Fodor, R. V., 1987. Low- and high-TiO₂ flood basalts of southern Brazil: origin from picritic parentage and a common mantle source. *Earth and Planetary Science Letters* 84, 423-430.
- Ghiorso, M. S., 1985. Chemical mass transfer in magmatic processes I. Thermodynamic relations and numerical algorithms. *Contributions to Mineralogy and Petrology* 90, 107-120.
- Ghiorso, M. S. & Sack, R. O., 1995. Chemical mass transfer in magmatic processes IV. A revised and internally consistent thermodynamic model for the interpolation and extrapolation of liquid-solid equilibria in magmatic systems at elevated temperatures and pressures. *Contributions to Mineralogy and Petrology* 119, 197-212.
- Gibson, S. A., Thompson, R. N., Dickin, A. P. & Leonardos, O. H., 1995. High-Ti and low-Ti mafic potassic magmas: Key to plume-lithosphere interactions and continental flood-basalt genesis. *Earth and Planetary Science Letters* 136, 149-165.
- Gijbels, R. H., Millard, H. T., Desborough, G. A. & Bartel, A. J., 1974. Osmium, ruthenium, iridium and uranium in silicates and chromite from the eastern Bushveld Complex, South Africa. *Geochimica et Cosmochimica Acta* 38, 319-337.
- Gonzalez-Jiménez, J. M., Gerville, F., Proenza, J. A., Augé, T. & Kerestedjian, T., 2009. Distribution of platinum-group minerals in ophiolitic chromitites. *Transactions of the*

Institution of Mining and Metallurgy, Section B (Applied Earth Sciences) 118, 101-110

Hanski, E., Kamenetsky, V. S., Luo, Z.-Y., Xu, Y.-G. & Kuzmin, D. V., 2010. Primitive magmas in the Emeishan Large Igneous Province, southwestern China and northern Vietnam. *Lithos* 119, 75-90.

Hao, T. T., Izokh, A. E., Polyakov, G. V., Borisenco, A. S., Anh, T. T., Balykin, P. A., Phuong, N. T., Rudnev, S. N., Van, V. V. & Nien, B. A., 2008. Permo-Triassic magmatism and metallogeny of Northern Vietnam in relation to the Emeishan plume. *Russian Geology and Geophysics* 49, 480-491.

Hawkesworth, C. J., Lightfoot, P. C., Fedorenko, V. A., Blake, S., Naldrett, A. J., Doherty, W. & Gorbachev, N. S., 1995. Magma differentiation and mineralization in the Siberian continental flood basalts. *Lithos* 34, 61-88.

He, B., Xu, Y.-G., Chung, S.-L., Xiao, L. & Wang, Y., 2003. Sedimentary evidence for a rapid, kilometer-scale crustal doming prior to the eruption of the Emeishan flood basalts. *Earth and Planetary Science Letters* 213, 391-405.

Kamenetsky, V. S., Chung, S.-L., Kamenetsky, M. B. & Kuzmin, D. V., 2012. Picrites from the Emeishan Large Igneous Province, SW China: a Compositional Continuum in Primitive Magmas and their Respective Mantle Sources. *Journal of Petrology* 53, 2095-2113.

- Li, C. & Ripley, E. M., 2005. Empirical equations to predict the sulfur content of mafic magmas at sulfide saturation and applications to magmatic sulfide deposits. *Mineralium Deposita* 40, 218-230.
- Li, J., Xu, J.-F., Suzuki, K., He, B., Xu, Y.-G. & Ren, Z.-Y., 2010. Os, Nd and Sr isotope and trace element geochemistry of the Muli picrites: insights into the mantle source of the Emeishan Large Igneous Province. *Lithos* 119, 108-122.
- Li, C., Tao, Y., Qi, L. & Ripley, E. M., 2012. Controls on PGE fractionation in the Emeishan picrites and basalts: Constraints from integrated lithophile-siderophile elements and Sr-Nd isotopes. *Geochimica et Cosmochimica Acta* 90, 12-32.
- Li, J., Wang, X.-C., Ren, Z.-Y., Xu, J.-F., He, B. & Xu, Y.-G., 2014. Chemical heterogeneity of the Emeishan mantle plume: evidence from highly siderophile element abundances in picrites. *Journal of Asian Earth Sciences* 79, 191-205.
- Liu, C. & Zhu, R., 2009. Geodynamic Significances of the Emeishan Basalts. *Earth Science Frontiers* 16, 52-69.
- Locmelis, M., Pearson, N. J., Barnes, S. J. & Fiorentini, M. L., 2011. Ruthenium in komatiitic chromite. *Geochimica et Comoschimica Acta* 75, 3645-3661.
- McDonough, W. F. & Sun, S.-S., 1995. The composition of the Earth. *Chemical Geology* 120, 223-253.
- Mungall, J. E., 2005. Magmatic geochemistry of the platinum-group elements. *Mineralogical Association of Canada Short Course* 35, Oulu, Finland, 1-34.

- O'Neill, H. St. C., Dingwell, D. B., Borisov, A., Spettel, B. & Palme, H., 1995. Experimental petrochemistry of some high siderophile elements at high temperatures and some implications for core formation and the mantle's early history. *Chemical Geology* 120, 255-273.
- Oshin, I. O. & Crocket, J. H., 1982. Noble metals in Thetford Mines ophiolites, Quebec, Canada. Park I: distribution of gold, iridium, platinum, and palladium in the ultramafic and gabbroic rocks. *Economic Geology* 77, 1556-1570.
- Pagé, P., Barnes, S.-J., Bédard, J. H. & Zientek, M. L., 2012. In situ determination of Os, Ir and Ru in chromites formed from komatiite, tholeiite and boninite magmas: Implications for chromite control of Os, Ir and Ru during partial melting and crystal fractionation. *Chemical Geology* 302-303, 1-15.
- Park, J.-W., Campbell, I. H. & Eggins, S. M., 2012. Enrichment of Rh, Ru, Ir and Os in Cr spinels from oxidized magmas: Evidence from the Ambae volcano, Vanuatu. *Geochimica et Cosmochimica Acta* 78, 28-50.
- Pearce, J. A. & Mei, H. J., 1988. Volcanic rocks of the 1985 Tibet Geotraverse: Lhasa and Goldmud. *Transactions of the Royal Society of London A* 327, 169-201.
- Peate, D. W., Hawkesworth, C. J. & Mantovani, M. S. M., 1992. Chemical stratigraphy of the Paraná lavas (South America): classification of magma types and their spatial distribution. *Bulletin of Volcanology* 55, 119-139.

- Prichard, H. M., Potts, P. J. & Neary, C. R., 1981. Platinum group element minerals in the Unst chromite, Shetland Isles. *Transactions of the Institution of Mining and Metallurgy, Section B (Applied Earth Sciences)* 90, B186-B188.
- Prichard, H. M., Neary, C. R., Fisher, P. C. & O'Hara, M. J., 2008. PGE-rich podiform chromitites in the Al'Ays ophiolite complex, Saudi Arabia: an example of critical mantle melting to extract and concentrate PGE. *Economic Geology* 103, 1507-1529.
- Puchtel, I. S. & Humayun, M., 2001. Platinum group element fractionation in a komatiitic basalt lava lake. *Geochimica et Cosmochimica Acta* 65, 2979-2993.
- Righter, K., Campbell, A. J., Humayun, M. & Hervig, R. L., 2004. Partitioning of Ru, Rh, Pd, Re, Ir and Au between Cr-bearing spinel, olivine, pyroxene and silicate melts. *Geochimica et Cosmochimica Acta* 68, 867-880.
- Roeder, P. L., Poustovetov, A. & Oskarsson, N., 2001. Growth forms and composition of chromian spinel in MORB magma: Diffusion-controlled crystallization of chromian spinel. *The Canadian Mineralogist* 39, 397-416.
- Roeder, P. L., Gofton, E. & Thornber, C., 2006. Cotectic Proportions of Olivine and Spinel in Olivine-Tholeiitic Basalt and Evaluation of Pre-Eruptive Processes. *Journal of Petrology* 47, 883-900.
- Savard, D., Barnes, S.-J. & Meisel, T., 2010. Comparison between nickel-sulfur fire assay Te co-precipitation and isotope dilution with high-pressure ash acid digestion for the determination of platinum-group elements, rhenium and gold. *Geostandards and Geoanalytical Research* 34, 281-291.

- Schwarzenbach, E. M., Gazel, E. & Caddick, M. J., 2014. Hydrothermal processes in partially serpentinized peridotites from Costa Rica: evidence from native copper and complex sulfide assemblages. *Contributions to Mineralogy and Petrology* 168, 21 p.
- Shellnutt, J. G., 2013. The Emeishan large igneous province: a synthesis. *Geoscience Frontiers* 5, 369-394.
- Song, X.-Y., Zhou, M.-F., Hou, Z.-Q., Cao, Z.-M., Wang, Y.-L. & Li, Y., 2001. Geochemical Constraints on the Mantle Source of the Upper Permian Emeishan Continental Flood Basalts, Southwestern China. *International Geology Review* 43, 213-225.
- Song, X.-Y., Zhou, M.-F., Cao, Z.-M., Sun, M. & Wang, Y.-L., 2003. Ni-Cu-(PGE) magmatic sulfide deposits in the Yangliuping area, Permian Emeishan igneous province, SW China. *Mineralium Deposita* 38, 831-843.
- Song, X.-Y., Zhou, M.-F. & Cao, Z.-M., 2004. Genetic relationships between base-metal sulfides and platinum-group minerals in the Yangliuping Ni-Cu-(PGE) sulfide deposit, southwestern China. *The Canadian Mineralogist* 42, 469-483.
- Song, X.-Y., Zhou, M.-F., Keays, R. R., Cao, Z.-M., Sun, M. & Qi, L., 2006. Geochemistry of the Emeishan flood basalts at Yangliuping, Sichuan, SW China: implications for sulfide segregation. *Contributions to Mineralogy and Petrology* 152, 53-74.
- Talkington, W., Watkinson, D. H., Whittaker, P. J. & Jones, P. C., 1983. Platinum-group-mineral inclusions in chromite from the Bird River Sill, Manitoba. *Mineralium Deposita* 18, 245-255.

- Talkington, R. W. & Lipin, B. R., 1986. Platinum-group minerals in chromite seams of the Stillwater Complex, Montana. *Economic Geology* 81, 1179-1186.
- Tao, Y., Li, C., Hu, R., Ripley, E. M., Du, A. & Zhong, H., 2007. Petrogenesis of the Pt-Pd mineralized Jinbaoshan ultramafic intrusion in the Permian Emeishan Large Igneous Province, SW China. *Contributions to Mineralogy and Petrology* 153, 321-337.
- Tao, Y., Li, C., Song, X.-Y. & Ripley, E. M., 2008. Mineralogical, petrological, and geochemical studies of the Limahe mafic-ultramafic intrusion and associated Ni-Cu sulfide ores, SW China. *Mineralium Deposita* 43, 849-872.
- Tao, Y., Li, C., Hu, R., Qi, L., Qu, W. & Du, A., 2010. Re-Os isotopic constraints on the genesis of the Limahe Ni-Cu deposit in the Emeishan large igneous province, SW China. *Lithos* 119, 137-146.
- Vogel, D. C. & Keays, R. R., 1997. The application of platinum group geochemistry in constraining the source of basalt magmas: results from the Newer Volcanic Province, Victoria, Australia. *Chemical Geology* 136, 181-204.
- Wang, C. Y., Zhou, M.-F. & Zhao, D., 2005. Mineral chemistry of chromite from the Permian Jinbaoshan Pt-Pd-sulphide bearing ultramafic intrusion in SW China with petrogenetic implications. *Lithos* 83, 47-66.
- Wang, C. Y., Zhou, M.-F. & Keays, R. R., 2006. Geochemical constraints on the origin of the Permian Baimazhai mafic-ultramafic intrusion, SW China. *Contributions to Mineralogy and Petrology* 152, 309-321.

- Wang, C. Y. & Zhou, M.-F., 2006. Genesis of the Permian Baimazhai magmatic Ni-Cu-(PGE) sulfide deposit, Yunnan, SW China. *Mineralium Deposita* 41, 771-783.
- Wang, C. Y., Zhou, M.-F. & Qi, L., 2007. Permian flood basalts and mafic intrusions in the Jinping (SW China)-Song Da (northern Vietnam) district: Mantle sources, crustal contamination and sulfide segregation. *Chemical Geology* 243, 317-343.
- Wang, C. Y., Prichard, H. M., Zhou, M.-F. & Fisher, P. C., 2008. Platinum-group minerals from the Jinbaoshan Pd-Pt deposit, SW China: evidence for magmatic origin and hydrothermal alteration. *Mineralium Deposita* 43, 791-803.
- Xiao, L., Xu, Y. G., Mei, H. J., Zheng, Y. F., He, B. & Pirajno, F., 2004. Distinct mantle sources of low-Ti and high-Ti basalts from the western Emeishan large igneous province, SW China: implications for plume-lithosphere interaction. *Earth and Planetary Science Letters* 228, 525-546.
- Xu, Y., Chung, S.-L., Jahn, B.-m. & Wu, G., 2001. Petrologic and geochemical constraints on the petrogenesis of Permian-Triassic Emeishan flood basalts in southwestern China. *Lithos* 58, 145-168.
- Zhang, Z. C., Mao, J., Mahoney, J. J., Wang, F. & Qu, W., 2005. Platinum group elements in the Emeishan large igneous province, SW China: Implications for mantle sources. *Geochemical Journal* 39, 371-382.
- Zhang, Z. C., Mahoney, J. J., Mao, J. W. & Wang, F. S., 2006a. Geochemistry of picritic and associated basalt flows of the Western Emeishan flood basalt province. *Journal of Petrology* 47, 1997-2019.

- Zhang, Z. C., Mao, J., Wang, F. S. & Pirajno, F., 2006. Native gold and native copper grains enclosed by olivine phenocrysts in a picrite lava of the Emeishan large igneous province, SW China. *American Mineralogist* 91, 1178-1183.
- Zhang, Z. C., Zhi, X., Chen, L., Saunders, A. D. & Reichow, M. K., 2008. Re-Os isotopic compositions of picrites from the Emeishan flood basalt province, China. *Earth and Planetary Science Letters* 276, 30-39.
- Zhong, H. & Zhu, W. G., 2006. Geochronology of layered mafic intrusions from the Panxi area in the Emeishan large igneous province, SW China. *Mineralium Deposita* 41, 599-606.
- Zhou, M.-F., Robinson, P. T., Lesher, C. M., Keays, R. R., Zhang, C. J. & Malpas, J., 2005. Geochemistry, petrogenesis, and metallogenesis of the Panzhihua gabbroic layered intrusion and associated Fe-Ti-V-oxide deposits, Sichuan Province, SW China. *Journal of Petrology* 46, 2253-2280.
- Zhou, M.-F., Arndt, N. T., Malpas, J., Wang, C. Y. & Kennedy, A. K., 2008. Two magma series and associated ore deposit types in the Permian Emeishan large igneous province. *Lithos* 103, 352-368.
- Zhou, M.-F., Chen, W. T., Wang, C. Y., Prevec, S. A., Liu, P. P. & Howarth, G. H., 2013. Two stages of immiscible liquid separation in the formation of Panzhihua-type Fe-Ti-V oxide deposits, SW China. *Geoscience Frontiers* 4, 481-502.

CHAPITRE 3

CONCLUSIONS GÉNÉRALES

3.1 INTRODUCTION

Pour cette étude de maîtrise une démarche scientifique originale a été appliquée afin d'évaluer l'effet de la cristallisation de la chromite sur le fractionnement des IEGP et du Rh dans les magmas picritiques sous-saturés en sulfures de la Grande Province Ignée d'Emeishan en Chine. Les conclusions générales qui ont été générées par les observations et les interprétations présentées dans le manuscrit du chapitre 2 sont synthétisées dans les trois prochaines sections (3.2, 3.3 et 3.4). La dernière section de ce chapitre (3.5) relate les travaux futurs qui pourraient être réalisés afin d'améliorer la compréhension actuelle du comportement des IEGP et du Rh lors de la cristallisation fractionnée des magmas sous-saturés en sulfures.

3.2 LES CHROMITES D'EMEISHAN

L'étude pétrographique a permis d'identifier deux populations de chromite dans les roches volcaniques de la ELIP : (1) les microphénocristaux libres dans la matrice, et (2) les chromites en inclusion dans les phénocristaux d'olivine. Les microphénocristaux libres dans la matrice sont caractérisés par la présence de bordure de surcroissance riche en Ti (Fig. 2.2b), tandis que les chromites en inclusion dans l'olivine montrent des interfaces

olivine-chromite relativement nettes (Fig. 2.2c). Les observations pétrographiques et les résultats d'analyses *in situ* par microsonde suggèrent que les deux populations de chromite sont en équilibre avec des compositions proche de celles des magmas primitifs de la ELIP (i.e., magmas picritiques; e.g., Chung et Jahn, 1995; Ali et al., 2005; Hanski et al., 2010; Zhou et al., 2013), et qu'elles sont originaires des premiers stades de la cristallisation fractionnée de ces magmas dans une chambre magmatique profonde, avant d'être acheminées vers la surface lors de l'ascension de magmas transporteurs plus évolués. Les analyses *in situ* par microsonde révèlent également que la composition des chromites reflète fortement la composition du magma à partir duquel elles ont cristallisé, en l'occurrence, les magmas picritiques riches en Ti ou pauvres en Ti (nommés *high-* et *low-Ti magmas* dans le manuscrit du chapitre 2, Fig. 2.3, 2.4 et 2.9; voir aussi Xu et al., 2001, Xiao et al., 2004 et Kamenetsky et al., 2012).

3.3 ASSOCIATION IEGP(RH)-CHROMITE

3.3.1 CONCENTRATIONS EN IEGP ET EN RH, COEFFICIENTS DE PARTAGE ET CALCULS DE BILAN DE MASSE

Les analyses *in situ* par LA-ICP-MS révèlent que les chromites d'Emeishan contiennent des concentrations uniformes en IEGP et en Rh allant de 8 à 151 ppb d'Os, de 6 à 56 ppb d'Ir, de 52 à 448 ppb de Ru et de 2 à 93 ppb de Rh (Figs. 2.10 et 2.12). Bien que la composition en éléments majeurs (e.g., Ti, Al et Fe) des chromites provenant des magmas

riches en Ti se distingue de celle des chromites qui proviennent des magmas pauvres en Ti, aucune différence notable n'a été observée entre les deux types de chromite (i.e., *high-* et *low-Ti chromites*) en termes de concentrations en IEGP et en Rh (Fig. 2.11).

Basés sur des calculs empiriques, les coefficients de partage déterminés lors de cette étude suggèrent que l'ordre de compatibilité des IEGP et du Rh dans les chromites d'Emeishan est la suivante : Ru > Rh > Ir \geq Os (Fig. 2.17). Cette différence comportementale avait également été noté par d'autres auteurs ayant déterminé des coefficients de partage à partir d'analyses *in situ* par LA-ICP-MS sur des chromites provenant d'autres séquences volcaniques mafiques à ultramafiques (Pagé et al. 2012; Park et al. 2012), confirmant d'ailleurs que le Ru est préférentiellement incorporé dans la chromite lorsque celle-ci cristallise.

Les calculs de bilan de masse révèlent que les chromites de picrites contrôlent jusqu'à 84% du budget roche totale en Ru, jusqu'à 49% du budget en Rh, mais moins de 22 et 20% des budgets en Ir et en Os, respectivement (Fig. 2.18). En revanche, le budget roche totale en IEGP et en Rh qui est contrôlé par les chromites des roches hypabyssales à phénocristaux d'olivine (nommés *OPSV rocks* dans le manuscrit du chapitre 2) et par celles du basalte aphyrique est généralement inférieur à celui des chromites de picrites. Puisque les chromites d'Emeishan ne contrôlent pas la totalité du budget roche totale en IEGP et en Rh, et plus particulièrement en Os et en Ir, il semblerait que d'autres phases enrichies en ces éléments, comme les MGP, soient présents dans les roches volcaniques de la ELIP, tel qu'il a été proposé par Pagé et al. (2012) pour expliquer les concentrations relativement

élevés en Os et en Ir des komatiites d'Alexo de la ceinture de roches vertes de l'Abitibi. De plus, puisqu'il a été démontré que les IEGP et le Rh peuvent être modérément compatible dans l'olivine (Brenan et al., 2003, 2005), il semblerait que celle-ci pourrait également jouer un rôle pour le contrôle de ces éléments.

3.3.2 PROCESSUS D'ENRICHISSEMENT EN IEGP ET EN RH

La corrélation positive entre le ratio $\text{Fe}^{3+}/(\text{Cr} + \text{Al} + \text{Fe}^{3+})$ et la concentration en Rh observée à partir des chromites d'Emeishan (Fig. 2.15) suggère que l'incorporation du Rh dans la chromite est contrôlée par le degré d'inversion de la structure du spinelle (représenté par le ratio $\text{Fe}^{3+}/(\text{Cr} + \text{Al} + \text{Fe}^{3+})$), et donc, que le Rh est sensible aux variations de la $f\text{O}_2$ au sein des magmas picritiques de la ELIP (le degré d'inversion de la structure du spinelle est influencé par la $f\text{O}_2$; voir aussi Brenan et al., 2012 et Park et al., 2012). Bien que cette relation ait également été observée avec les concentrations en IEGP des chromites des laves du volcan d'Ambae (Vanuatu) précédemment investiguées par Park et al. (2012), il n'en est rien pour les chromites d'Emeishan. Par conséquent, il semblerait qu'un ou plusieurs autres paramètres soient à l'origine de l'incorporation des IEGP dans les chromites des roches volcaniques de la ELIP, tels que la température élevée des magmas picritiques, laquelle influence la solubilité de ces éléments, et/ou la présence de concentrations élevées de ces éléments dans les magmas primitifs.

3.3.3 MGP EN ASSOCIATION AVEC LA CHROMITE

Les analyses *in situ* par LA-ICP-MS et l'étude des chromites par SEM révèlent la présence de grains micrométriques de laurite, de sperrylite et d'alliages d'Os-Ir (\pm Ru) et de Pt-Fe (\pm IEGP et Rh) en association avec les chromites d'Emeishan (Fig. 2.10 et 2.13). La présence de ces grains à la marge des cristaux de chromite, mais également en inclusion dans ces derniers, suggère fortement que la chromite a servi de nucléus pour la précipitation de MGP, et que ceux-ci ont ensuite pu être englobées par la chromite lors de la croissance ultérieure de cette dernière. Cette interprétation est consistante avec le modèle proposé par Finnigan et al. (2008), lequel suggère que la précipitation des MGP est favorisée à l'interface chromite-liquide, et ce, puisque c'est à cet endroit que la solubilité des IEGP et du Rh (et possiblement du Pt) est la plus faible.

3.4 ÉVOLUTION MAGMATIQUE ET FRACTIONNEMENT DES IEGP ET DU RH

La compétition qui existe entre la chromite et les sulfures en ce qui a trait au fractionnement des IEGP et du Rh entre les phases solides (ou un liquide immiscible) et le liquide silicaté dépend essentiellement du moment où le liquide sulfuré est ségrégué. Bien qu'il a été démontré à partir d'une modélisation du ratio Cu/Pd et de la concentration en Pd du liquide silicaté que les échantillons étudiés ont subi jusqu'à 1% de fractionnement avec ségrégation de liquide sulfuré en proportion cotectique (Fig. 2.14), plusieurs évidences

suggèrent que ce processus est ultérieur à la cristallisation de la chromite et des MGP. Par conséquent, il semblerait que le fractionnement des IEGP et du Rh lors des premiers stades de la cristallisation fractionnée soit contrôlé par la co-cristallisation d'olivine et de chromite et/ou par la formation de MGP, tandis que la ségrégation de liquide sulfuré serait plutôt à l'origine d'un appauvrissement tardif de ces éléments, mais également du Pt, du Pd et des autres éléments chalcophiles comme le Cu.

La modélisation des concentrations en IEGP et en Rh (Fig. 2.19 et 2.20) suggère que la chromite, l'olivine et les MGP contribuent tous au fractionnement de ces éléments lors des premiers stades de la cristallisation fractionnée. En assumant que les IEGP et le Rh sont compatibles dans l'olivine (Brenan et al., 2003, 2005), cette modélisation numérique évoque la possibilité que la co-cristallisation d'olivine et de chromite soit à l'origine des corrélations positives entre les concentrations roches totales en IEGP et en Cr observées à partir des roches volcaniques de la ELIP (Fig. 2.19). De plus, il a été interprété que la formation de MGP pourrait être à l'origine de certaines subtilités compositionnelles. Cependant, puisque la compatibilité des IEGP et du Rh dans l'olivine et la quantité de MGP présente dans les échantillons de picrites sont incertaines, l'importance relative entre l'olivine et les MGP en ce qui a trait au contrôle et au fractionnement des IEGP et du Rh reste à être établie avec plus de précision. En revanche, il semble évident que l'incorporation préférentielle du Ru dans la structure de la chromite est responsable de la présence d'anomalies négatives en Ru, telles qu'observées à partir des profils en Ni-Cu-EGP normalisés des basaltes les moins évolués de la ELIP (Fig. 2.20).

3.5 TRAVAUX FUTURS

Bien que cette étude de maîtrise ait permis de faire un pas en avant en ce qui a trait à la compréhension des processus qui gèrent le fractionnement des IEGP et du Rh dans les magmas sous-saturés en sulfures, certains aspects demeurent partiellement, voire même, totalement incompris, et mériteraient donc une investigation plus poussée. Voici quelques travaux qui pourraient être réalisés dans le futur afin de valider certaines interprétations ayant mené à nos conclusions tout en améliorant la compréhension actuelle du comportement adopté par les IEGP et le Rh lors du processus de cristallisation fractionnée :

- 1) Réalisation d'une étude complète au SEM portant sur la nature des MGP en association avec les chromites d'Emeishan; cette étude pourrait permettre de confirmer la présence d'alliages d'Os-Ir (\pm Ru), mais également de répertorier des phases qui n'ont actuellement pas été découvertes, telles que le ou les MGP qui contrôlent le budget roche totale restant en Rh.
- 2) Réalisation d'une étude portant sur la composition en éléments traces par LA-ICP-MS des phénocristaux d'olivine; cette étude permettrait de vérifier le partitionnement des IEGP et du Rh dans l'olivine, mais également de déterminer si des MGP sont en inclusion dans ce type de phénocristaux.

3.6 RÉFÉRENCES

- Ali, J. R., Thompson, G. M., Zhou, M.-F. & Song, X., 2005. Emeishan large igneous province, SW China. *Lithos* 79, 475-489.
- Brenan, J. M., McDounough, W. F. & Dalpé, C., 2003. Experimental constraints on the partitioning of rhenium and some platinum-group elements between olivine and silicate melt. *Earth and Planetary Science Letters* 212, 135-150.
- Brenan, J. M., McDonough, W. F. & Ash, R., 2005. An experimental study of the solubility and partitioning of iridium, osmium and gold between olivine and silicate melt. *Earth and Planetary Science Letters* 237, 855-872.
- Brenan, J. M., Finnigan, C. F., McDonough, W. F. & Homolova, V., 2012. Experimental constraints on the partitioning of Ru, Rh, Ir, Pt and Pd between chromite and silicate melt: The importance of ferric iron. *Chemical Geology* 302-303, 16-32.
- Chung, S.-L. & Jahn, B.-m., 1995. Plume-lithosphere interaction in generation of the Emeishan flood basalts at the Permian-Triassic boundary. *Geology* 23, 889-892.
- Finnigan, C. S., Brenan, J. M., Mungall, J. E. & McDonough, W. F., 2008. Experiments and model bearing on the role of chromite as a collector of platinum group minerals by local reduction. *Journal of Petrology* 49, 1647-1665.

- Hanski, E., Kamenetsky, V. S., Luo, Z.-Y., Xu, Y.-G. & Kuzmin, D. V., 2010. Primitive magmas in the Emeishan Large Igneous Province, southwestern China and northern Vietnam. *Lithos* 119, 75-90.
- Kamenetsky, V. S., Chung, S.-L., Kamenetsky, M. B. & Kuzmin, D. V., 2012. Picrites from the Emeishan Large Igneous Province, SW China: a Compositional Continuum in Primitive Magmas and their Respective Mantle Sources. *Journal of Petrology* 53, 2095-2113.
- Pagé, P., Barnes, S.-J., Bédard, J. H. & Zientek, M. L., 2012. In situ determination of Os, Ir and Ru in chromites formed from komatiite, tholeiite and boninite magmas: Implications for chromite control of Os, Ir and Ru during partial melting and crystal fractionation. *Chemical Geology* 302-303, 1-15.
- Park, J.-W., Campbell, I. H. & Eggins, S. M., 2012. Enrichment of Rh, Ru, Ir and Os in Cr spinels from oxidized magmas: Evidence from the Ambae volcano, Vanuatu. *Geochimica et Cosmochimica Acta* 78, 28-50.
- Xiao, L., Xu, Y. G., Mei, H. J., Zheng, Y. F., He, B. & Pirajno, F., 2004. Distinct mantle sources of low-Ti and high-Ti basalts from the western Emeishan large igneous province, SW China: implications for plume-lithosphere interaction. *Earth and Planetary Science Letters* 228, 525-546.

Xu, Y., Chung, S.-L., Jahn, B.-m. & Wu, G., 2001. Petrologic and geochemical constraints on the petrogenesis of Permian-Triassic Emeishan flood basalts in southwestern China. *Lithos* 58, 145-168.

Zhou, M.-F., Chen, W. T., Wang, C. Y., Prevec, S. A., Liu, P. P. & Howarth, G. H., 2013. Two stages of immiscible liquid separation in the formation of Panzhihua-type Fe-Ti-V oxide deposits, SW China. *Geoscience Frontiers* 4, 481-502.

ANNEXE 1 : LOCALISATION DES ÉCHANTILLONS

Localisation des échantillons

Échantillon	Lithologie	Localisation	UTM NAD83			Échantillonnage
			Zone	Abscisse	Ordonnée	
13-BC-02	Picrite	Binchuan	47	648911	2851817	Affleurement
13-BC-03	Basalte à plagioclase	Binchuan	47	648968	2851783	Affleurement
13-BC-04	Picrite	Binchuan	47	648958	2851836	Sub-en place
13-BC-05	Picrite	Binchuan	47	648959	2851825	Bloc
13-BC-06	Picrite	Binchuan	47	648928	2851827	Bloc
13-BC-07	Picrite	Binchuan	47	648861	2851813	Bloc
13-DL-01	Basalte à plagioclase	Dali	47	635708	2842611	Affleurement
13-DL-02	Picrite	Dali	47	640747	2835390	Bloc
13-DL-03	Picrite	Dali	47	640727	2835373	Bloc
13-DL-04	Picrite	Dali	47	641824	2836140	Affleurement
13-DL-05	Basalte à plagioclase	Dali	47	641824	2836140	Affleurement
13-DL-06	Picrite	Dali	47	641330	2835845	Sub-en place
13-JC-01	Picrite	Jianchuan	47	593893	2937275	Bloc
13-JC-02	Picrite	Jianchuan	47	593860	2937272	Bloc
13-JC-03	Picrite	Jianchuan	47	593860	2937272	Bloc
13-JC-04	Picrite	Jianchuan	47	593833	2937268	Bloc
13-JC-05	Picrite	Jianchuan	47	593833	2937268	Bloc
13-JC-06	Picrite	Jianchuan	47	593817	2937268	Bloc
13-JC-07	Picrite	Jianchuan	47	593748	2937215	Bloc
13-DJ-01	Basalte à pyroxène	Daju	47	625756	3004910	Sub-en place
13-DJ-02	Basalte aphyrique	Daju	47	625741	3004896	Affleurement
13-DJ-03	Picrite	Daju	47	625717	3004861	Affleurement
13-DJ-04	Picrite	Daju	47	625832	3004884	Bloc
13-DJ-05	Picrite	Daju	47	625832	3004884	Bloc
13-DJ-06	Picrite	Daju	47	625832	3004884	Bloc
13-DJ-07	Basalte à pyroxène	Daju	47	625899	3004771	Bloc
13-DJ-08	Picrite	Daju	47	625903	3004788	Bloc
13-DJ-09	Picrite	Daju	47	625903	3004788	Bloc
13-DJ-10	Basalte à pyroxène	Daju	47	625810	3004687	Affleurement
13-SM-01	Basalte à pyroxène	Shiman	47	618070	2972509	Sub-en place
13-SM-02	Picrite	Shiman	47	618070	2972509	Bloc
13-SM-03	Picrite	Shiman	47	618145	2972560	Bloc
13-SM-04	Basalte à pyroxène	Shiman	47	618136	2972756	Bloc
13-ET-02	Subvolcanique à olivine	Ertan	47	774647	2969870	Bloc
13-ET-03	Subvolcanique à olivine	Ertan	47	774666	2969838	Bloc
13-ET-04	Subvolcanique à olivine	Ertan	47	774666	2969838	Bloc

ANNEXE 2 : ANALYSES ROCHES TOTALES

Compositions roches totales recalculées à 100% anhydre

Échantillon	13-DL-01	13-DL-02	13-DL-03	13-DL-04	13-DL-05	13-DL-06	13-BC-02	13-BC-03	13-BC-04	13-BC-05	13-BC-06	13-BC-07	13-JC-01
<i>Éléments majeurs (% poids)</i>													
SiO ₂	50,41	45,41	45,51	50,41	49,16	45,38	44,52	50,39	44,20	44,46	45,46	44,58	45,47
TiO ₂	2,54	1,10	1,10	1,17	3,42	1,10	0,80	3,66	0,73	0,80	0,96	0,78	1,82
Al ₂ O ₃	13,53	10,09	9,86	10,14	12,95	9,93	8,67	13,28	8,03	8,67	10,67	8,74	8,50
Fe ₂ O ₃ ^{Total}	14,70	12,14	12,19	10,77	16,20	12,26	11,76	15,53	11,76	11,86	11,92	11,73	13,16
MnO	0,18	0,18	0,18	0,14	0,28	0,18	0,18	0,14	0,18	0,18	0,18	0,18	0,18
MgO	3,57	19,70	20,68	15,82	4,63	20,15	24,24	3,25	25,78	24,11	18,87	24,55	20,60
CaO	7,67	9,61	8,92	9,62	9,34	9,33	8,27	6,98	8,30	8,65	9,71	8,17	8,74
Na ₂ O	5,08	1,35	1,15	1,51	2,62	1,24	1,04	5,94	0,66	0,84	1,24	0,88	1,07
K ₂ O	1,34	0,28	0,25	0,24	0,98	0,27	0,33	0,40	0,19	0,27	0,76	0,23	0,26
P ₂ O ₅	0,95	0,16	0,16	0,17	0,42	0,16	0,18	0,43	0,16	0,18	0,22	0,17	0,20
Total	99,98	100,00	99,99	99,99	100,00	99,99	100,00	99,99	100,00	100,02	100,00	100,01	99,99
LOI	1,24	2,11	3,61	3,71	0,72	2,78	3,54	1,74	4,20	3,82	2,99	4,09	3,13
<i>Éléments du groupe du platine et Au (ppb)</i>													
Os	<LOD	1,24	1,20	1,39	0,03	1,34	2,15	0,08	2,10	1,80	0,68	1,27	1,52
Ir	<LOD	0,73	0,83	0,76	<LOD	0,87	1,28	0,05	1,31	1,19	0,72	0,96	0,86
Ru	<LOD	1,68	1,85	1,93	<LOD	1,58	2,44	0,19	3,06	2,07	1,98	2,16	1,77
Rh	0,05	0,39	0,51	0,49	0,21	0,41	0,61	0,50	0,74	0,58	0,73	0,66	0,43
Pt	2,61	7,32	8,14	6,70	4,62	7,02	7,14	8,67	7,81	6,79	10,53	8,95	7,43
Pd	5,85	5,65	7,20	5,78	13,54	5,77	6,15	12,58	5,53	4,52	9,10	5,79	5,89
Au	0,69	1,06	1,49	1,22	3,64	0,58	<LOD	0,79	<LOD	1,34	2,18	0,85	1,90

Compositions roches totales recalculées à 100% anhydre (suite)

Échantillon	13-DL-01	13-DL-02	13-DL-03	13-DL-04	13-DL-05	13-DL-06	13-BC-02	13-BC-03	13-BC-04	13-BC-05	13-BC-06	13-BC-07	13-JC-01
<i>Éléments traces (ppm)</i>													
Ba	402,67	66,65	56,80	53,75	373,22	66,93	255,72	50,73	165,36	269,29	713,32	123,44	107,45
Be	2,44	0,64	0,69	0,51	1,82	0,61	0,76	1,67	0,68	0,79	0,93	0,70	0,86
Bi	<0,15	<0,15	<0,15	<0,15	<0,15	<0,15	<0,15	<0,15	<0,15	<0,15	<0,15	<0,15	<0,15
Cd	0,06	0,06	0,07	0,06	0,09	0,07	0,08	0,19	0,08	0,07	0,09	0,08	0,08
Ce	67,66	11,02	11,03	12,23	55,41	10,97	31,61	67,95	27,97	30,35	37,41	29,00	36,79
Co	50,86	97,49	94,54	79,39	64,34	94,77	101,26	55,71	104,42	101,75	89,35	101,18	92,05
Cr	6,11	1746,94	1793,69	1774,55	54,62	1593,45	2110,19	82,51	2349,98	2158,94	1497,10	2221,99	1590,51
Cs	1,74	1,63	2,17	1,66	0,94	3,07	3,54	0,63	1,36	1,23	5,44	0,88	4,24
Cu	164,14	124,27	121,32	139,18	341,76	122,88	95,01	254,15	84,09	102,29	113,34	100,53	105,58
Dy	7,85	3,30	3,33	3,58	8,72	3,29	2,81	8,02	2,60	2,81	3,46	2,76	3,90
Er	4,25	1,82	1,80	1,93	4,46	1,82	1,53	3,89	1,39	1,53	1,90	1,48	1,89
Eu	2,38	0,93	0,94	1,03	2,77	0,95	1,03	2,88	0,93	0,99	1,22	0,98	1,53
Ga	18,65	13,71	13,47	12,00	24,25	13,29	9,85	20,99	9,36	9,65	11,92	10,62	12,89
Gd	8,44	3,25	3,27	3,44	9,43	3,20	3,08	9,45	2,76	3,03	3,67	2,95	4,51
Hf	5,83	1,86	1,87	1,94	6,56	1,84	1,48	6,94	1,35	1,51	1,80	1,40	3,39
Ho	1,53	0,64	0,65	0,70	1,63	0,65	0,56	1,47	0,49	0,54	0,69	0,53	0,71
In	0,08	0,05	0,05	0,06	0,11	0,05	0,04	0,10	0,04	0,04	0,05	0,04	0,06
La	32,42	4,64	4,61	5,17	24,99	4,60	16,10	30,37	14,05	15,29	19,05	14,88	16,30
Li	16,79	5,75	9,50	8,57	2,43	8,70	7,90	4,48	7,85	7,12	7,15	7,01	3,94
Lu	0,55	0,22	0,22	0,23	0,52	0,23	0,19	0,43	0,17	0,19	0,24	0,19	0,22
Mo	2,00	0,55	0,52	0,33	2,35	0,77	0,52	1,09	0,43	0,45	0,53	0,38	0,85
Nb	36,28	4,78	4,81	4,92	23,89	4,82	11,76	31,47	10,43	11,69	14,43	10,79	16,81
Nd	36,02	8,42	8,47	9,14	35,25	8,43	15,40	41,75	13,67	14,70	18,62	14,72	21,21

Compositions roches totales recalculées à 100% anhydre (suite)

Échantillon	13-DL-01	13-DL-02	13-DL-03	13-DL-04	13-DL-05	13-DL-06	13-BC-02	13-BC-03	13-BC-04	13-BC-05	13-BC-06	13-BC-07	13-JC-01
<i>Éléments traces (ppm)</i>													
Ni	13,33	933,04	963,88	996,24	56,34	920,02	1092,72	79,45	1148,60	1083,66	757,15	1095,93	906,02
Pb	6,11	1,23	1,36	0,84	4,55	1,14	2,18	3,16	1,99	2,30	2,59	2,09	1,45
Pr	8,68	1,73	1,69	1,89	7,79	1,71	3,92	9,54	3,48	3,72	4,70	3,66	5,00
Rb	53,46	14,49	19,03	5,04	21,51	15,63	17,73	4,36	11,06	17,07	32,84	13,73	18,73
S	<LOD	<LOD	<LOD	<LOD	110,14	<LOD							
Sb	0,06	0,05	0,04	<0,04	<0,04	0,05	0,04	0,08	<0,04	0,04	<0,04	0,04	0,04
Sc	18,22	28,76	27,88	30,01	27,31	27,66	29,00	24,65	29,43	27,12	32,74	29,40	25,80
Sm	8,13	2,61	2,64	2,85	8,86	2,66	3,12	9,55	2,82	3,06	3,80	3,06	4,68
Sn	2,27	0,78	0,80	0,83	2,95	0,80	0,63	2,53	0,57	0,60	0,73	0,58	1,23
Sr	493,64	145,32	141,05	132,39	424,09	150,44	326,72	159,01	165,46	214,11	385,52	185,79	245,05
Ta	2,43	0,72	0,62	0,48	2,23	0,73	0,91	2,47	0,84	0,96	1,17	0,85	1,41
Tb	1,28	0,52	0,53	0,56	1,45	0,52	0,47	1,37	0,43	0,47	0,58	0,45	0,66
Th	4,73	0,66	0,69	0,70	3,94	0,67	2,20	3,64	1,90	2,04	2,65	1,99	1,86
Ti	14637	6531	6429	6728	20587	6424	4515	21247	4170	4543	5516	4337	10198
Tl	0,07	0,03	0,05	0,01	0,06	0,04	0,05	0,02	0,04	0,03	0,08	0,03	0,05
Tm	0,60	0,25	0,25	0,27	0,60	0,25	0,21	0,52	0,19	0,21	0,26	0,20	0,25
U	1,03	0,24	0,24	0,25	1,04	0,25	0,45	0,64	0,39	0,44	0,52	0,39	0,47
V	305,28	237,96	240,66	235,80	>370	235,91	184,72	>370	170,28	186,89	221,92	174,91	239,25
W	106,05	100,01	77,26	47,49	>141	99,95	73,88	96,12	72,76	81,57	96,91	71,22	73,04
Y	41,24	17,47	17,15	18,55	43,52	17,13	14,47	40,14	13,21	14,31	17,91	14,39	18,24
Yb	3,76	1,53	1,54	1,62	3,64	1,55	1,30	3,04	1,19	1,32	1,62	1,24	1,50
Zn	112,95	87,30	87,70	69,02	138,57	85,99	75,88	112,05	74,35	76,43	78,74	74,28	92,22
Zr	242,19	68,81	68,91	72,15	256,90	67,34	60,29	279,11	54,46	59,68	72,52	56,49	132,63

Compositions roches totales recalculées à 100% anhydre (suite)

Échantillon	13-JC-02	13-JC-03	13-JC-04	13-JC-05	13-JC-06	13-JC-07	13-DJ-01	13-DJ-02	13-DJ-03	13-DJ-04	13-DJ-05	13-DJ-06	13-DJ-07
<i>Éléments majeurs (% poids)</i>													
SiO ₂	44,38	44,99	45,57	46,90	45,65	45,57	48,29	53,35	43,97	44,94	44,97	44,90	46,05
TiO ₂	1,37	1,20	1,84	1,97	1,71	1,84	2,31	2,19	1,21	1,78	1,76	1,76	2,17
Al ₂ O ₃	7,98	7,93	8,58	9,72	8,37	8,58	12,90	13,19	5,45	8,31	8,13	8,19	11,77
Fe ₂ O ₃ ^{Total}	12,86	12,20	13,11	12,51	13,06	13,22	12,08	11,25	12,78	12,71	12,69	12,77	13,14
MnO	0,19	0,18	0,18	0,18	0,18	0,18	0,18	0,11	0,17	0,18	0,18	0,18	0,22
MgO	23,35	23,99	20,46	17,80	20,64	20,26	9,97	5,93	30,45	21,43	21,99	21,65	11,15
CaO	8,42	8,14	8,69	9,17	8,95	8,75	9,55	7,09	5,79	8,74	8,65	8,79	11,94
Na ₂ O	0,84	0,82	1,06	1,33	0,94	1,13	3,72	5,92	0,02	0,98	0,81	0,88	2,31
K ₂ O	0,41	0,38	0,30	0,23	0,32	0,27	0,63	0,70	0,03	0,66	0,57	0,63	0,83
P ₂ O ₅	0,18	0,18	0,20	0,20	0,17	0,20	0,38	0,26	0,12	0,25	0,24	0,24	0,43
Total	99,99	100,01	100,00	100,01	100,00	100,00	100,00	100,00	100,00	100,00	100,00	100,00	100,01
LOI	3,76	4,62	3,03	1,88	3,13	2,58	2,95	1,50	8,79	3,90	4,82	4,19	2,87
<i>Éléments du groupe du platine et Au (ppb)</i>													
Os	2,21	1,67	2,17	0,55	1,57	2,81	0,15	0,21	2,82	1,64	1,74	2,09	0,19
Ir	1,31	1,24	1,32	0,67	0,97	1,88	<LOD	0,11	1,22	1,15	1,08	1,28	0,31
Ru	2,28	1,79	2,43	1,49	1,91	2,44	0,25	0,21	2,24	2,44	2,14	1,77	0,14
Rh	0,66	0,46	0,50	0,45	0,41	0,57	0,14	0,10	0,39	0,50	0,51	0,40	0,36
Pt	9,03	5,86	8,41	8,35	8,11	9,03	5,15	3,08	15,57	7,54	7,15	6,40	7,82
Pd	9,63	2,50	7,04	8,02	3,03	8,75	2,81	2,78	3,93	3,95	2,79	2,11	5,39
Au	2,77	1,56	2,04	2,62	0,74	2,72	0,76	<LOD	<LOD	1,19	1,07	<LOD	0,74

Compositions roches totales recalculées à 100% anhydre (suite)

Échantillon	13-JC-02	13-JC-03	13-JC-04	13-JC-05	13-JC-06	13-JC-07	13-DJ-01	13-DJ-02	13-DJ-03	13-DJ-04	13-DJ-05	13-DJ-06	13-DJ-07
<i>Éléments traces (ppm)</i>													
Ba	205,29	132,07	118,23	138,53	99,73	139,43	232,61	105,89	17,11	305,93	283,05	446,77	380,06
Be	0,86	0,87	0,94	0,85	0,70	0,94	1,61	1,28	0,56	1,26	1,23	1,31	1,81
Bi	<0,15	<0,15	<0,15	<0,15	<0,15	<0,15	<0,15	<0,15	<0,15	<0,15	<0,15	<0,15	<0,15
Cd	0,09	0,06	0,07	0,09	0,06	0,08	0,17	0,07	0,05	0,10	0,06	0,07	0,14
Ce	34,63	29,72	37,62	39,92	30,19	37,61	41,16	59,69	21,35	48,56	48,39	48,43	39,13
Co	98,65	92,26	90,96	86,86	93,02	93,39	64,60	51,54	119,19	96,02	94,39	95,49	70,41
Cr	2311,38	2161,14	1580,91	1280,84	1598,17	1550,82	624,55	428,05	2513,05	1922,31	1974,83	1935,62	712,88
Cs	1,09	1,59	3,21	2,88	0,88	4,79	0,10	0,12	0,80	0,39	0,46	0,50	0,18
Cu	99,21	86,57	119,47	131,16	97,97	125,32	59,47	75,42	73,66	135,01	128,31	130,76	80,61
Dy	3,15	2,75	3,80	4,25	3,55	3,86	4,84	4,82	2,42	3,42	3,38	3,41	4,31
Er	1,60	1,44	1,92	2,09	1,73	1,90	2,39	2,44	1,15	1,68	1,65	1,69	2,22
Eu	1,20	1,07	1,51	1,72	1,39	1,51	1,85	1,84	0,98	1,45	1,42	1,46	1,68
Ga	10,30	9,75	13,17	14,55	12,54	13,14	16,79	12,45	5,43	11,66	11,35	11,35	15,06
Gd	3,54	3,03	4,48	5,00	4,16	4,44	5,68	5,43	2,91	4,10	4,09	4,11	5,01
Hf	2,68	2,31	3,38	3,79	3,08	3,38	4,19	4,39	2,22	3,54	3,48	3,50	3,44
Ho	0,58	0,52	0,70	0,78	0,65	0,70	0,90	0,90	0,44	0,63	0,62	0,63	0,82
In	0,05	0,04	0,06	0,06	0,06	0,06	0,08	0,08	0,04	0,05	0,05	0,05	0,06
La	16,28	13,77	16,59	17,18	12,66	16,67	16,86	28,24	9,12	22,96	23,06	22,90	17,39
Li	10,32	9,90	4,04	3,48	3,94	5,05	4,02	2,14	8,11	5,67	6,56	5,68	4,66
Lu	0,19	0,17	0,21	0,24	0,19	0,21	0,29	0,30	0,13	0,19	0,20	0,19	0,26
Mo	1,00	0,45	0,94	1,05	0,55	0,93	0,74	0,87	0,36	0,76	0,73	0,72	2,28
Nb	16,62	14,71	16,90	17,03	12,99	17,11	24,92	26,74	9,21	21,91	22,01	22,26	26,15
Nd	18,34	15,72	21,23	23,76	18,71	21,91	24,95	28,31	13,20	24,69	24,12	24,69	22,77

Compositions roches totales recalculées à 100% anhydre (suite)

Échantillon	13-JC-02	13-JC-03	13-JC-04	13-JC-05	13-JC-06	13-JC-07	13-DJ-01	13-DJ-02	13-DJ-03	13-DJ-04	13-DJ-05	13-DJ-06	13-DJ-07
<i>Éléments traces (ppm)</i>													
Ni	944,87	944,60	898,02	774,96	906,60	890,74	239,72	171,02	1624,82	957,17	974,51	962,97	283,18
Pb	1,77	2,11	1,55	1,54	1,14	1,54	2,16	2,85	1,22	3,25	3,17	3,26	1,97
Pr	4,51	3,87	5,04	5,47	4,23	5,11	5,74	7,10	2,99	6,16	6,10	6,13	5,31
Rb	13,33	12,20	17,30	16,58	9,55	15,11	13,09	22,04	15,96	20,05	21,50	21,03	15,02
S	150,75	<LOD	72,96	64,08	59,22	85,80	<LOD	<LOD	296,89	221,29	273,53	<LOD	<LOD
Sb	0,05	<0,04	0,05	0,05	0,04	0,05	0,08	0,05	<0,04	0,04	0,04	0,04	0,10
Sc	27,20	28,44	26,09	27,85	27,71	26,05	32,57	30,47	22,00	27,61	27,50	27,04	34,50
Sm	3,78	3,30	4,68	5,13	4,28	4,81	5,67	5,82	3,03	4,71	4,59	4,77	5,01
Sn	0,93	0,86	1,26	1,46	1,05	1,22	1,69	1,89	0,91	1,34	1,31	1,20	1,84
Sr	208,11	149,87	239,88	302,55	200,91	260,01	217,25	166,63	69,33	258,48	230,70	241,32	285,15
Ta	1,33	1,13	1,40	1,56	1,17	1,51	1,85	2,19	0,76	1,66	1,61	1,68	1,91
Tb	0,52	0,46	0,66	0,73	0,62	0,66	0,83	0,80	0,41	0,59	0,58	0,60	0,74
Th	1,98	1,72	1,86	2,00	1,38	1,91	1,96	3,27	0,87	2,57	2,49	2,49	1,97
Ti	7513	6609	10547	11384	9754	10545	13550	12817	7008	10195	10110	10022	12211
Tl	0,03	0,01	0,05	0,05	0,01	0,05	0,02	0,03	0,01	0,02	0,02	0,02	0,02
Tm	0,22	0,19	0,25	0,28	0,22	0,25	0,32	0,34	0,15	0,23	0,23	0,23	0,29
U	0,48	0,35	0,50	0,50	0,42	0,53	0,56	0,57	0,19	0,56	0,55	0,55	0,42
V	205,50	196,84	247,64	262,31	234,85	246,94	257,24	299,63	150,43	232,13	229,00	226,91	304,42
W	69,39	49,58	68,97	102,31	71,23	90,74	86,66	123,11	38,76	72,78	58,64	72,50	78,47
Y	15,40	13,40	18,61	20,57	16,97	18,54	23,67	22,76	11,29	16,36	16,37	16,52	21,48
Yb	1,35	1,16	1,47	1,65	1,37	1,48	2,01	2,08	0,93	1,38	1,37	1,38	1,81
Zn	78,16	74,78	91,11	89,08	89,25	91,65	90,69	49,94	88,88	87,14	84,62	86,26	91,18
Zr	104,21	89,52	134,59	151,53	120,38	134,90	165,93	177,33	85,55	140,68	140,68	138,86	137,81

Compositions roches totales recalculées à 100% anhydre (suite)

Échantillon	13-DJ-08	13-DJ-09	13-DJ-10	13-SM-01	13-SM-02	13-SM-03	13-SM-04	13-ET-02	13-ET-03	13-ET-04	Limite de détection (LOD) *
<i>Éléments majeurs (% poids)</i>											
SiO ₂	44,88	44,67	48,33	46,66	45,35	45,20	45,14	46,30	46,10	44,89	0,040
TiO ₂	1,72	1,34	1,97	2,15	1,48	1,39	2,39	2,05	2,02	1,05	0,010
Al ₂ O ₃	8,02	6,81	12,01	11,81	7,61	7,30	11,03	6,80	6,74	5,76	0,020
Fe ₂ O ₃ ^{Total}	12,69	12,31	12,75	12,39	13,68	12,73	13,10	13,38	13,33	13,05	0,010
MnO	0,18	0,17	0,18	0,42	0,23	0,19	0,25	0,18	0,17	0,18	0,002
MgO	22,36	24,67	10,22	9,80	23,32	23,85	9,94	21,86	22,22	26,59	0,010
CaO	8,33	9,42	10,23	14,12	7,61	8,55	15,66	7,50	7,42	7,81	0,006
Na ₂ O	0,97	0,37	2,63	1,99	0,40	0,49	1,74	0,73	0,78	0,43	0,020
K ₂ O	0,61	0,12	1,42	0,26	0,13	0,14	0,22	0,97	0,99	0,18	0,010
P ₂ O ₅	0,23	0,13	0,26	0,39	0,17	0,16	0,54	0,22	0,22	0,08	0,002
Total	99,99	100,00	100,00	99,99	99,99	99,99	100,00	99,99	100,00	100,01	
LOI	3,63	4,50	2,53	2,07	6,76	5,91	2,20	3,87	3,34	4,17	0,050
<i>Éléments du groupe du platine et Au (ppb)</i>											
Os	2,04	2,26	0,25	0,25	2,21	3,76	0,12	5,31	5,07	2,23	0,065
Ir	1,24	1,30	0,46	0,72	1,42	2,22	0,83	1,94	1,84	1,82	0,025
Ru	2,23	2,04	0,36	0,26	2,54	3,19	0,18	3,51	3,77	3,46	0,120
Rh	0,51	0,36	0,34	0,89	0,54	0,79	0,85	0,60	0,65	0,79	0,082
Pt	7,74	6,15	8,78	13,71	9,40	9,94	17,40	18,81	18,98	15,64	0,084
Pd	2,79	4,12	6,63	12,94	3,01	3,83	11,90	7,86	7,95	7,96	0,471
Au	0,65	<LOD	1,02	4,58	0,92	1,86	3,68	1,45	1,81	4,26	

* Les limites de détection pour les EGP ont été tirées de Savard et al. (2010).

Compositions roches totales recalculées à 100% anhydre (suite)

Échantillon	13-DJ-08	13-DJ-09	13-DJ-10	13-SM-01	13-SM-02	13-SM-03	13-SM-04	13-ET-02	13-ET-03	13-ET-04	Limite de détection (LOD)
<i>Éléments traces (ppm)</i>											
Ba	292,62	143,41	1304,79	253,55	53,38	48,02	652,20	337,69	342,18	47,94	0,800
Be	1,14	0,54	1,04	1,97	0,81	0,77	2,21	0,84	0,87	0,37	0,040
Bi	<0,15	<0,15	<0,15	<0,15	<0,15	<0,15	<0,15	<0,15	<0,15	<0,15	0,150
Cd	0,06	0,07	0,09	0,19	0,09	0,09	0,17	0,07	0,07	0,09	0,013
Ce	45,04	21,80	43,31	29,37	26,38	24,36	42,05	63,42	63,26	13,82	0,120
Co	95,22	105,47	66,85	71,55	106,35	96,41	70,80	96,66	98,25	110,15	0,130
Cr	2054,49	2331,65	630,60	591,93	2243,64	2012,38	574,38	2053,08	2047,28	2212,69	3,000
Cs	0,44	0,31	0,15	0,10	0,70	0,54	0,12	1,15	1,75	0,66	0,013
Cu	120,26	86,17	116,23	>2900	81,86	108,09	192,69	86,82	69,67	75,78	1,400
Dy	3,23	2,82	4,48	4,04	3,00	2,78	4,19	3,66	3,65	2,19	0,009
Er	1,58	1,39	2,33	2,01	1,48	1,38	2,04	1,57	1,53	1,03	0,007
Eu	1,35	1,11	1,65	1,50	1,10	1,05	1,65	2,01	1,98	0,86	0,003
Ga	11,19	9,94	14,68	14,70	9,96	10,16	15,03	12,33	12,33	9,24	0,040
Gd	3,80	3,27	5,10	4,49	3,42	3,13	4,90	5,31	5,26	2,59	0,009
Hf	3,29	2,44	3,68	3,09	2,47	2,30	3,52	4,72	4,78	1,71	0,140
Ho	0,58	0,52	0,85	0,75	0,55	0,52	0,76	0,62	0,60	0,39	0,003
In	0,05	0,05	0,07	0,07	0,05	0,05	0,07	0,05	0,05	0,04	0,002
La	21,18	8,87	19,55	12,59	11,32	10,60	19,32	28,26	27,86	5,59	0,040
Li	5,43	5,47	2,78	5,97	9,75	7,47	7,78	9,19	10,21	10,26	0,400
Lu	0,18	0,15	0,28	0,24	0,18	0,16	0,23	0,15	0,15	0,11	0,002
Mo	0,71	0,44	0,74	1,07	0,49	0,64	1,10	1,02	1,11	0,45	0,080
Nb	20,19	9,41	21,34	20,22	13,22	12,16	27,93	26,05	25,90	5,23	0,028
Nd	22,76	14,49	23,55	18,70	15,56	14,61	24,11	35,39	34,62	9,56	0,060

Compositions roches totales recalculées à 100% anhydre (suite)

Échantillon	13-DJ-08	13-DJ-09	13-DJ-10	13-SM-01	13-SM-02	13-SM-03	13-SM-04	13-ET-02	13-ET-03	13-ET-04	Limite de détection (LOD)
<i>Éléments traces (ppm)</i>											
Ni	967,53	1062,61	225,14	172,23	1159,61	1025,93	178,25	1004,18	1033,95	1279,15	1,600
Pb	2,92	0,84	2,27	1,75	0,87	1,28	3,79	3,76	3,64	0,73	0,600
Pr	5,73	3,18	5,71	4,10	3,55	3,33	5,66	8,45	8,25	2,05	0,014
Rb	21,01	5,05	24,33	4,01	6,10	6,79	2,70	38,35	38,58	10,18	0,230
S	<LOD	<LOD	<LOD	91,07	152,85	124,53	164,79	88,37	49,46	297,71	49,00
Sb	0,05	<0,04	<0,04	<0,04	<0,04	<0,04	<0,04	0,06	0,05	<0,04	0,040
Sc	26,62	30,83	38,23	41,80	29,99	27,00	43,92	22,25	21,66	26,90	1,100
Sm	4,39	3,35	5,17	4,43	3,50	3,26	5,21	6,84	6,76	2,48	0,012
Sn	1,23	0,86	1,32	1,29	0,91	0,84	1,41	1,40	1,57	0,61	0,160
Sr	244,18	143,62	312,00	433,81	81,75	95,39	811,61	332,67	377,69	138,06	0,600
Ta	1,58	0,95	1,65	1,60	0,98	0,97	2,12	1,88	1,84	0,57	0,023
Tb	0,54	0,48	0,75	0,68	0,52	0,47	0,70	0,69	0,69	0,38	0,002
Th	2,31	0,91	2,31	1,27	1,29	1,18	2,16	3,55	3,56	0,55	0,018
Ti	9634	7604	11192	12335	8652	7864	14359	11599	11374	5996	7,000
Tl	0,02	0,01	0,04	<0,005	0,01	0,01	<0,005	0,03	0,03	0,01	0,005
Tm	0,21	0,18	0,31	0,27	0,20	0,19	0,27	0,19	0,20	0,13	0,002
U	0,51	0,26	0,46	0,31	0,31	0,30	0,42	0,82	0,80	0,15	0,011
V	221,94	194,97	332,72	348,36	224,91	204,55	>370	243,86	236,59	183,59	0,800
W	73,30	84,89	84,62	89,80	38,92	43,88	98,61	71,99	72,51	57,90	0,050
Y	15,50	13,65	22,09	19,59	14,89	13,74	20,50	15,85	15,78	10,19	0,050
Yb	1,28	1,11	1,91	1,63	1,22	1,12	1,67	1,13	1,12	0,77	0,009
Zn	82,47	77,86	82,43	103,97	92,04	81,09	94,19	94,03	94,76	80,59	7,000
Zr	130,49	97,85	140,13	115,30	97,46	89,63	133,10	192,25	191,61	62,80	6,000

ANNEXE 3 : MATÉRIAUX DE RÉFÉRENCES POUR LES ANALYSES ROCHE TOTALES

Compositions en éléments majeurs des matériaux de références

	SiO ₂ (% poids)	TiO ₂	Al ₂ O ₃	Fe ₂ O ₃ ^{Total}	MnO	MgO
<i>Valeurs analysées</i>						
KPT-1	53,39	0,90	14,45	12,29	0,14	4,28
OKUM	44,24	0,39	8,06	11,90	0,19	21,36
<i>Valeurs acceptées</i>						
KPT-1 ^a	54,14±0,10	0,90±0,004	14,41±0,05	12,24±0,03	0,14±0,001	4,30±0,02
OKUM ^b	43,57±0,13	0,40±0,01	8,05±0,03	12,14±0,02	0,18±0,01	22,37±0,11

Compositions en éléments majeurs des matériaux de références (suite)

	CaO	Na ₂ O	K ₂ O	P ₂ O ₅	LOI	Total
<i>Valeurs analysées</i>						
KPT-1	6,84	2,56	1,66	0,17	1,38	98,06
OKUM	7,88	1,10	0,05	0,02	4,69	99,89
<i>Valeurs acceptées</i>						
KPT-1 ^a	6,89±0,02	2,61±0,02	1,65±0,005	0,17±0,002	nd	nd
OKUM ^b	8,06±0,03	1,15±0,01	0,04±0,01	0,02±0,01	4,66±0,05	100,63±0,29

^a Valeurs tirées de Webb et al. (2006).

^b Valeurs tirées du certificat d'analyse de *Geo Labs, Geoscience Laboratories*.

Compositions en EGP des matériaux de références

Os (ppb)	Ir	Ru	Rh	Pt	Pd	Au
<i>Valeurs analysées</i>						
OKUM 1,10	0,85	4,24	1,33	13,6	11,67	1,92
<i>Valeurs acceptées</i>						
OKUM $0,98 \pm 0,34^{\text{a}}$	$0,99 \pm 0,07^{\text{b}}$	$4,25 \pm 0,30^{\text{b}}$	$1,40 \pm 0,13^{\text{b}}$	$11,04 \pm 0,55^{\text{b}}$	$11,73 \pm 0,50^{\text{b}}$	$1,49 \pm 0,16^{\text{b}}$

^a Valeur tirée de Savard et al. (2010).^b Valeurs tirées du certificat d'analyse de *Geo Labs, Geoscience Laboratories*.*Compositions en éléments traces des matériaux des références*

Ba (ppm)	Be	Bi	Cd	Ce	Co	Cr	Cs	Cu ^c	Dy
<i>Valeurs analysées</i>									
KPT-1 462,20	1,39	2,73	0,42	54,14	83,07	154	4,44	1249,10	4,50
OKUM 6,10	0,10	<0,15	0,07	1,29	89,46	2473	0,18	46,80	1,62
<i>Valeurs acceptées</i>									
KPT-1 ^a $465,27 \pm 2,17$	$1,42 \pm 0,05$	$0,95 \pm 0,07$	nd	$55,71 \pm 0,78$	nd	$152,24 \pm 2,24$	$4,42 \pm 0,08$	1112 ± 102	$4,47 \pm 0,05$
OKUM ^b 7±1	nd	nd	nd	1,4±0,1	84±1	2120±38	0,19±0,01	45±1	1,5±0,1

Compositions en éléments traces des matériaux des références (suite)

	Er	Eu	Ga	Gd	Hf	Ho	In	La	Li	Lu
<i>Valeurs analysées</i>										
KPT-1	2,80	1,24	18,46	4,63	4,59	0,92	0,10	26,29	33,70	0,41
OKUM	1,05	0,30	8,92	1,22	0,56	0,35	0,03	0,46	3,90	0,15
<i>Valeurs acceptées</i>										
KPT-1 ^a	2,72±0,03	1,24±0,02	18,21±0,22	4,60±0,05	4,41±0,08	0,95±0,01	nd	26,91±0,32	35,10±1,31	0,42±0,01
OKUM ^b	1,02±0,02	0,3±0,1	8±1	1,14±0,02	0,60±0,02	0,38±0,01	nd	0,47±0,02	4±1	0,15±0,01

Compositions en éléments traces des matériaux des références (suite)

	Mo	Nb	Nd	Ni ^c	Pb	Pr	Rb	Sb	Sc	Sm
<i>Valeurs analysées</i>										
KPT-1	1,57	8,35	24,31	1283	84,20	6,44	61,58	11,51	25,10	4,91
OKUM	0,33	0,35	1,55	893	<0,6	0,25	1,13	0,07	27,90	0,72
<i>Valeurs acceptées</i>										
KPT-1 ^a	1,72±0,12	8,48±0,15	24,64±0,24	1093±72	81,07±0,99	6,39±0,06	61,45±0,58	10,01±0,33	24,84±0,30	4,90±0,05
OKUM ^b	<1±nd	0,4±0,1	1,5±0,1	780±11	nd	0,27±0,01	1,14±0,04	nd	23±1	0,69±0,02

Compositions en éléments traces des matériaux des références (suite)

	Sn	Sr	Ta	Tb	Th	Ti	Tl	Tm	U	V
<i>Valeurs analysées</i>										
KPT-1	>14	255,80	0,59	0,72	6,93	5235	0,49	0,41	1,79	193,40
OKUM	0,36	16,00	0,02	0,22	0,03	2220	0,01	0,15	0,01	174,10
<i>Valeurs acceptées</i>										
KPT-1 ^a	19,13±0,38	261,04±2,23	0,60±0,02	0,74±0,01	7,27±0,14	nd	0,54±0,01	0,41±0,004	1,76±0,2	197,22±1,82
OKUM ^b	nd	16±1	<0,5±nd	<0,5±nd	<0,5±nd	nd	<0,5±nd	<0,3±nd	<0,03±nd	166±4

Compositions en éléments traces des matériaux des références (suite)

	W	Y	Yb	Zn	Zr
<i>Valeurs analysées</i>					
KPT-1	1,27	25,73	2,71	122	185
OKUM	0,12	9,45	0,98	66	18
<i>Valeurs acceptées</i>					
KPT-1 ^a	nd	25,82±0,31	2,69±0,03	120,24±1,83	158,12±0,35
OKUM ^b	nd	10,33±0,15	0,97±0,03	52±1	19±1

^a Valeurs tirées de Webb et al. (2006)^b Valeurs tirées du certificat d'analyse de *Geo Labs, Geoscience Laboratories*^c Valeurs internes du LabMaTer à l'Université du Québec à Chicoutimi

ANNEXE 4 : ANALYSES MINÉRALES PAR MICROSONDE

Analyses de chromites par microsonde

# Grain	Minéral	SiO ₂	TiO ₂	Al ₂ O ₃	Cr ₂ O ₃	V ₂ O ₅	FeO ^{Total}	MnO	MgO	Total	FeO ^a	Fe ₂ O ₃ ^a	Cr# ^b	Mg# ^c	Fe ³⁺ /R ^{3+, d}
<i>Contenu en % poids</i>															
Bc2a-Ci1	Chromite	0,10	0,57	15,97	50,50	0,09	20,16	0,12	12,95	100,45	15,52	5,16	67,96	60,15	0,06
Bc2a-Ci2	Chromite	0,11	0,60	16,18	49,65	0,14	19,71	0,17	13,17	99,73	15,05	5,18	67,30	61,39	0,07
Bc2b-Cm1	Chromite	0,07	0,60	16,30	48,45	0,13	24,28	0,28	10,57	100,67	19,21	5,63	66,60	49,81	0,07
Bc2d-Cm1	Chromite	0,37	0,60	16,84	44,70	0,13	27,49	0,17	9,39	99,70	21,30	6,88	64,03	44,83	0,09
Bc2c-Cb1	Chromite	0,09	0,54	16,96	51,41	0,12	16,55	0,08	14,47	100,22	13,28	3,64	67,04	66,42	0,05
Bc4d-Ci1	Chromite	0,48	0,58	16,69	47,61	0,12	20,52	0,11	12,41	98,54	16,40	4,58	65,68	58,78	0,07
Bc4e-Ci1	Chromite	0,16	0,59	15,57	50,85	0,10	18,70	0,13	11,39	97,49	16,98	1,91	68,67	54,96	0,03
Bc4c-Cm1	Chromite	0,07	0,56	15,98	46,61	0,19	25,95	0,26	9,43	99,04	20,49	6,07	66,18	45,41	0,08
Bc4G-Cm1	Chromite	0,07	0,42	12,64	46,41	0,12	30,59	0,23	8,27	98,74	21,48	10,13	71,12	40,94	0,13
Bc4d-Cb1	Chromite	0,05	0,47	14,41	46,00	0,10	27,27	0,30	9,60	98,19	19,41	8,73	68,16	47,05	0,11
Bc4e-Cb1	Chromite	0,09	0,56	15,59	44,89	0,17	26,99	0,30	9,70	98,28	19,74	8,06	65,89	47,04	0,10
Bc5a-Ci1	Chromite	0,07	0,33	16,44	46,42	0,15	22,57	0,15	12,26	98,40	15,84	7,48	65,45	58,37	0,09
Bc5a-Ci2	Chromite	0,10	0,31	16,19	46,89	0,12	21,81	0,08	12,84	98,35	14,97	7,60	66,03	60,91	0,10
Bc5d-Ci1	Chromite	0,12	0,56	16,75	48,30	0,14	19,45	0,00	12,56	97,88	15,64	4,24	65,93	59,36	0,06
Bc5a-Cib1	Chromite	0,08	0,33	16,17	46,00	0,17	21,90	0,23	12,51	97,38	15,05	7,60	65,62	60,14	0,10
Bc5c-Cm1	Chromite	0,18	0,26	15,51	49,25	0,09	21,39	0,19	11,24	98,11	17,08	4,79	68,05	54,53	0,06
Bc5e-Cm1	Chromite	0,07	0,60	11,70	50,28	0,15	26,46	0,08	9,40	98,73	19,88	7,31	74,24	46,04	0,10
Bc5a-Cb1	Chromite	0,08	0,31	16,32	47,72	0,15	21,15	0,13	12,31	98,17	15,69	6,08	66,23	58,72	0,08
Bc5c-Ci1	Chromite	0,12	0,61	15,69	49,29	0,13	21,36	0,11	12,09	99,42	16,57	5,32	67,82	57,00	0,07
Bc6a-Cm1	Chromite	0,12	0,68	16,63	46,48	0,18	23,67	0,11	11,13	99,00	18,21	6,07	65,21	52,61	0,08
Bc6b-Cm1	Chromite	0,11	0,67	16,60	44,89	0,14	25,56	0,07	10,50	98,54	19,00	7,29	64,47	50,03	0,09
Bc6e-Cm1	Chromite	0,08	0,62	13,02	50,83	0,14	22,73	0,16	11,19	98,77	17,29	6,04	72,37	53,92	0,08
Bc7a-Ci1	Chromite	0,26	0,47	11,82	50,31	0,12	23,56	0,17	10,89	97,60	17,31	6,94	74,06	53,63	0,10
Bc7e-Ci1	Chromite	0,11	0,58	16,60	49,57	0,13	17,18	0,06	14,36	98,58	13,02	4,62	66,70	66,80	0,06

Analyses de chromites par microsonde (suite)

# Grain	Minéral	SiO ₂	TiO ₂	Al ₂ O ₃	Cr ₂ O ₃	V ₂ O ₅	FeO ^{Total}	MnO	MgO	Total	FeO ^a	Fe ₂ O ₃ ^a	Cr# ^b	Mg# ^c	Fe ³⁺ /R ^{3+, d}
<i>Contenu en % poids</i>															
Bc7f-Cm1	Chromite	0,10	0,53	15,10	45,64	0,17	28,50	0,15	8,56	98,74	21,72	7,53	66,98	41,59	0,10
Bc7f-Cm2	Chromite	0,11	0,52	14,20	44,17	0,08	31,51	0,31	7,99	98,89	22,16	10,38	67,60	39,37	0,13
Bc7g-Cb1	Chromite	0,09	0,79	15,76	44,60	0,09	27,05	0,18	10,43	98,98	19,12	8,81	65,50	49,58	0,11
Dl2c-Ci1	Chromite	0,15	0,65	18,32	50,45	0,10	15,15	0,09	15,51	100,42	12,05	3,44	64,88	70,22	0,04
Dl2b-Cm1	Chromite	0,11	0,66	15,41	53,65	0,13	15,62	0,23	14,67	100,47	12,78	3,16	70,02	67,67	0,04
Dl2e-Cm1	Chromite	0,11	0,77	16,72	48,71	0,19	21,23	0,19	12,33	100,26	16,72	5,01	66,15	57,31	0,07
Dl2f-Cm1	Chromite	0,73	1,62	15,36	44,88	0,51	24,28	0,15	11,81	99,35	19,15	5,71	66,22	54,59	0,10
Dl2d-Cb1	Chromite	0,11	0,87	16,85	48,94	0,18	20,24	0,09	12,98	100,25	16,01	4,71	66,09	59,62	0,06
Dl3b-Ci1	Chromite	0,08	0,91	14,27	49,36	0,29	24,37	0,16	10,69	100,11	19,14	5,81	69,89	50,38	0,08
Dl3d-Ci1	Chromite	0,07	0,84	16,99	47,04	0,28	22,50	0,08	11,95	99,75	17,51	5,54	65,01	55,43	0,07
Dl3a-Cm1	Chromite	0,12	0,68	14,93	53,18	0,20	16,50	0,07	14,36	100,04	13,35	3,51	70,49	66,35	0,05
Dl3c-Cm1	Chromite	0,13	0,56	17,09	51,18	0,17	17,94	0,00	13,50	100,57	15,19	3,06	66,76	61,89	0,04
Dl3e-Cb1	Chromite	0,10	0,69	18,50	47,45	0,19	18,18	0,14	14,45	99,70	13,64	5,05	63,24	65,95	0,06
Dl4f-Ci1	Chromite	0,16	0,53	15,29	55,45	0,14	12,92	0,03	16,31	100,83	10,53	2,65	70,87	74,10	0,04
Dl4f-Ci2	Chromite	0,17	0,53	15,57	54,56	0,12	14,27	0,15	15,83	101,18	11,28	3,31	70,16	72,12	0,04
Dl4a-Cm1	Chromite	0,11	0,81	17,38	49,52	0,21	17,01	0,12	14,67	99,83	13,30	4,13	65,65	66,90	0,05
Dl4d-Cm1	Chromite	0,09	0,91	18,99	47,72	0,24	19,48	0,06	13,85	101,34	15,51	4,42	62,76	61,97	0,06
Dl4g-Cm1	Chromite	0,11	0,55	18,35	48,97	0,26	20,64	0,14	13,27	102,29	16,25	4,88	64,16	59,89	0,06
Dl4e-Cb1	Chromite	0,16	0,53	15,68	54,37	0,08	15,31	0,02	15,29	101,45	12,28	3,37	69,94	69,52	0,04
Dl4g-Cb1	Chromite	0,11	0,66	14,86	51,98	0,14	20,40	0,10	12,98	101,22	15,68	5,24	70,12	60,05	0,07
Dl6a-Ci1	Chromite	0,16	0,52	15,70	51,88	0,08	16,97	0,11	14,19	99,60	13,29	4,08	68,92	66,09	0,05
Dl6a-Ci2	Chromite	0,13	0,54	15,35	52,99	0,13	13,21	0,00	16,34	98,69	9,79	3,81	69,85	75,48	0,05
Dl6d-Ci1	Chromite	0,40	0,73	16,75	46,97	0,25	20,45	0,20	13,65	99,40	14,94	6,13	65,29	63,36	0,09
Dl6c-Cm1	Chromite	0,05	1,21	19,09	41,80	0,32	24,57	0,04	12,23	99,32	17,75	7,59	59,50	55,65	0,10

# Grain	Minéral	SiO ₂	TiO ₂	Al ₂ O ₃	Cr ₂ O ₃	V ₂ O ₅	FeO ^{Total}	MnO	MgO	Total	FeO ^a	Fe ₂ O ₃ ^a	Cr# ^b	Mg# ^c	Fe ³⁺ /R ^{3+, d}
<i>Contenu en % poids</i>															
Dl6c-Cm2	Chromite	0,08	1,04	20,68	41,33	0,35	24,35	0,20	10,96	98,98	19,53	5,35	57,28	50,58	0,07
Dl6d-Cb1	Chromite	0,11	0,85	17,46	47,22	0,23	22,80	0,25	11,46	100,37	18,32	4,98	64,47	53,24	0,07
Dl6a-Cb1	Chromite	0,14	0,56	15,42	52,87	0,05	16,44	0,11	14,73	100,31	12,61	4,25	69,70	68,00	0,05
Dj2a-Cm1	Chromite	0,13	0,86	15,09	43,74	0,29	27,16	0,19	10,32	97,77	19,14	8,90	66,04	49,62	0,12
Dj2a-Cm2	Chromite	0,08	0,90	14,86	45,72	0,21	26,30	0,03	10,39	98,50	19,27	7,82	67,36	49,43	0,10
Dj2b-Cm1	Chromite	0,07	1,37	12,26	43,28	0,27	30,86	0,29	9,31	97,71	20,48	11,54	70,32	45,18	0,16
Dj2c-Cm1	Chromite	0,09	1,37	15,23	42,56	0,41	27,40	0,20	11,38	98,63	18,43	9,96	65,21	53,10	0,13
Dj2d-Cm1	Chromite	0,11	2,09	16,12	39,22	0,40	28,01	0,23	11,77	97,95	18,36	10,72	62,00	54,08	0,15
Dj2d-Cm2	Chromite	0,08	1,77	16,60	40,22	0,39	27,33	0,10	11,54	98,02	18,62	9,68	61,91	53,15	0,13
Dj3a-Ci1	Chromite	0,10	1,03	13,24	51,48	0,12	19,98	0,12	14,18	100,24	13,61	7,08	72,29	65,45	0,09
Dj3d-Ci1	Chromite	0,12	1,50	10,87	52,16	0,22	23,90	0,15	11,16	100,07	18,42	6,08	76,29	52,45	0,08
Dj3g-Cm1	Chromite	0,07	1,64	10,62	49,94	0,23	28,60	0,05	8,91	100,06	22,01	7,32	75,93	42,29	0,10
Dj3g-Cm2	Chromite	0,08	1,64	10,74	51,29	0,20	25,01	0,06	11,39	100,41	18,28	7,48	76,21	53,05	0,10
Dj3f-Cm1	Chromite	0,10	1,52	11,36	52,31	0,20	22,48	0,00	12,37	100,32	16,83	6,28	75,55	57,23	0,08
Dj3f-Cm2	Chromite	0,09	1,45	11,07	51,91	0,13	24,50	0,00	10,87	100,02	18,79	6,35	75,88	51,12	0,08
Dj3c-Cb1	Chromite	0,14	1,50	12,34	49,81	0,22	24,37	0,15	11,19	99,71	18,45	6,58	73,02	52,52	0,09
Dj4f-Ci1	Chromite	0,23	1,69	13,68	46,82	0,19	22,27	0,00	12,67	97,54	16,11	6,84	69,66	59,18	0,10
Dj4f-Ci2	Chromite	0,16	1,93	13,76	49,83	0,43	22,44	0,01	12,82	101,38	17,61	5,37	70,84	57,38	0,08
Dj4c-Cm1	Chromite	0,08	2,21	13,33	43,23	0,26	28,26	0,21	9,62	97,20	20,80	8,29	68,51	45,62	0,12
Dj4d-Cm1	Chromite	0,05	1,75	10,87	47,50	0,27	29,86	0,17	7,93	98,41	22,98	7,65	74,57	38,42	0,11
Dj4e-Cb1	Chromite	0,10	2,61	12,83	41,60	0,33	32,15	0,20	7,51	97,32	24,48	8,52	68,50	35,76	0,12
Dj4e-Cb2	Chromite	0,08	2,33	12,95	43,06	0,32	30,80	0,15	8,60	98,27	22,94	8,73	69,05	40,48	0,12
Dj4a-Cb1	Chromite	0,10	1,68	14,39	46,01	0,27	25,39	0,28	10,36	98,48	19,76	6,26	68,21	48,83	0,09
Dj5a-Ci1	Chromite	0,08	2,22	13,85	44,41	0,26	29,85	0,03	9,20	99,89	22,52	8,14	68,26	42,51	0,11

Analyses de chromites par microsonde (suite)

# Grain	Minéral	SiO ₂	TiO ₂	Al ₂ O ₃	Cr ₂ O ₃	V ₂ O ₅	FeO ^{Total}	MnO	MgO	Total	FeO ^a	Fe ₂ O ₃ ^a	Cr# ^b	Mg# ^c	Fe ³⁺ /R ^{3+, d}
<i>Contenu en % poids</i>															
Dj5d-Ci1	Chromite	0,08	2,97	15,77	38,87	0,45	30,37	0,19	10,50	99,21	21,49	9,87	62,31	47,17	0,14
Dj5d-Ci2	Chromite	0,12	2,02	13,79	45,13	0,29	27,59	0,10	10,64	99,67	20,20	8,21	68,71	48,99	0,11
Dj5b-Cm1	Chromite	0,08	2,09	12,48	44,00	0,23	34,33	0,23	6,22	99,66	26,57	8,62	70,28	29,69	0,12
Dj5b-Cm2	Chromite	0,05	2,30	13,41	41,76	0,31	35,04	0,25	6,34	99,45	26,69	9,28	67,62	30,01	0,13
Dj5e-Cb1	Chromite	0,08	1,71	14,01	45,54	0,20	30,12	0,21	7,54	99,41	24,29	6,48	68,56	35,91	0,09
Dj6c-Ci1	Chromite	0,07	2,18	13,13	44,60	0,22	31,51	0,19	7,74	99,64	24,38	7,93	69,50	36,43	0,11
Dj6e-Ci1	Chromite	0,14	2,38	13,33	44,65	0,36	30,96	0,23	9,37	101,42	22,93	8,92	69,20	42,73	0,12
Dj6e-Ci2	Chromite	0,08	2,21	13,36	45,55	0,29	27,84	0,29	10,24	99,87	20,71	7,93	69,58	47,35	0,11
Dj6a-Cm1	Chromite	0,08	2,16	14,14	43,87	0,33	28,84	0,20	9,82	99,44	21,52	8,13	67,54	45,35	0,11
Dj6d-Cm1	Chromite	0,09	1,94	12,83	45,86	0,28	29,44	0,17	9,25	99,86	22,02	8,25	70,57	43,27	0,11
Dj6f-Cm1	Chromite	0,08	1,88	11,63	46,84	0,22	30,68	0,10	8,96	100,39	22,42	9,17	72,99	41,97	0,12
Dj6c-Cb1	Chromite	0,07	1,69	13,51	47,63	0,24	25,59	0,09	11,34	100,15	18,75	7,60	70,29	52,31	0,10
Dj6e-Cb1	Chromite	0,09	2,21	13,26	45,46	0,32	30,08	0,00	8,99	100,41	23,15	7,70	69,69	41,36	0,11
Dj7g-Cm1	Chromite	0,07	2,01	11,00	46,09	0,20	27,44	0,24	11,81	98,84	17,41	11,14	73,76	55,14	0,15
Dj8a-Ci1	Chromite	0,08	1,47	14,37	48,78	0,15	21,90	0,23	11,92	98,89	17,15	5,27	69,49	55,73	0,07
Dj8c-Ci1	Chromite	0,09	1,95	12,52	46,88	0,24	26,74	0,05	10,62	99,09	19,64	7,89	71,52	49,53	0,11
Dj8c-Ci2	Chromite	0,07	2,20	12,73	45,67	0,27	29,23	0,24	9,47	99,89	21,79	8,27	70,64	44,07	0,11
Dj8e-Cm1	Chromite	0,06	1,76	11,60	46,64	0,26	31,18	0,23	7,98	99,70	23,49	8,55	72,96	38,05	0,12
Dj8f-Cm1	Chromite	0,05	2,23	13,09	44,56	0,28	30,87	0,27	8,37	99,73	23,44	8,26	69,54	39,24	0,11
Dj8b-Cm1	Chromite	0,07	2,35	13,33	44,51	0,33	29,87	0,25	8,83	99,54	22,95	7,69	69,13	41,13	0,11
Dj8d-Cb1(a)	Chromite	0,05	1,52	13,71	47,02	0,23	26,79	0,18	10,46	99,96	19,79	7,78	69,71	48,89	0,10
Dj8d-Cb1(b)	Chromite	0,07	1,53	13,89	47,44	0,22	26,14	0,06	10,76	100,10	19,57	7,30	69,62	49,90	0,10
Dj8d-Cb1(c)	Chromite	0,08	1,53	13,88	47,44	0,23	26,11	0,05	10,54	99,85	19,89	6,92	69,63	48,99	0,09
Dj9b-Ci1	Chromite	0,05	1,48	10,06	46,17	0,26	29,08	0,16	9,56	96,82	19,70	10,43	75,48	46,78	0,14

Analyses de chromites par microsonde (suite)

# Grain	Minéral	SiO ₂	TiO ₂	Al ₂ O ₃	Cr ₂ O ₃	V ₂ O ₅	FeO ^{Total}	MnO	MgO	Total	FeO ^a	Fe ₂ O ₃ ^a	Cr# ^b	Mg# ^c	Fe ³⁺ /R ^{3+, d}
<i>Contenu en % poids</i>															
Dj9c-Ci1	Chromite	0,10	1,32	14,92	42,85	0,33	29,13	0,03	9,66	98,33	20,92	9,12	65,83	45,69	0,12
Dj9f-Ci1	Chromite	0,15	1,23	16,22	40,75	0,25	29,14	0,14	10,51	98,39	19,63	10,57	62,76	49,42	0,14
Dj9a-Cm1	Chromite	0,09	1,19	12,61	46,16	0,21	30,68	0,28	7,25	98,47	23,68	7,78	71,06	35,62	0,11
Dj9f-Cm1	Chromite	0,14	1,84	16,90	38,53	0,27	32,84	0,24	7,66	98,40	24,53	9,24	60,47	36,18	0,13
DJ9e-Cb1	Chromite	0,09	0,94	12,89	47,66	0,16	27,91	0,11	8,80	98,55	21,34	7,30	71,28	42,68	0,10
Sm1e-Ci4	Chromite	0,05	1,60	10,19	49,76	0,26	30,64	0,22	7,21	99,93	24,35	6,98	76,62	34,84	0,10
Sm1e-Ci3	Chromite	0,06	2,31	13,45	46,39	0,27	27,07	0,02	10,86	100,43	20,24	7,58	69,82	49,30	0,10
Sm1e-Ci2	Chromite	0,06	1,87	12,05	49,34	0,20	25,33	0,16	11,05	100,06	19,02	7,01	73,32	51,24	0,09
Sm1e-Ci1	Chromite	0,03	1,45	11,71	51,15	0,28	27,00	0,14	9,24	101,00	21,80	5,78	74,56	43,38	0,08
Sm2c-Ci1	Chromite	0,07	2,13	13,11	44,61	0,25	27,90	0,00	10,54	98,61	19,93	8,86	69,53	48,96	0,12
Sm2c-Ci2	Chromite	0,13	1,94	12,66	44,03	0,21	29,38	0,24	10,21	98,78	20,13	10,28	70,00	47,96	0,14
Sm2g-Ci1	Chromite	0,15	4,10	12,13	38,65	0,34	32,82	0,15	10,44	98,77	21,87	12,17	68,13	46,59	0,18
Sm2b-Cm1	Chromite	0,08	1,86	12,68	45,91	0,23	29,71	0,25	8,01	98,73	23,29	7,14	70,83	38,34	0,10
Sm2e-Cm1	Chromite	0,07	1,80	12,41	47,34	0,17	30,78	0,30	7,55	100,41	24,30	7,20	71,91	35,90	0,10
Sm2a-Cb1	Chromite	0,08	2,15	12,12	44,67	0,25	30,27	0,10	8,09	97,73	23,15	7,91	71,19	38,73	0,11
Sm2h-Cb1	Chromite	0,09	2,04	15,97	39,48	0,25	31,34	0,12	8,99	98,27	22,51	9,81	62,39	41,97	0,13
Sm3d-Ci2	Chromite	0,07	1,82	13,59	47,04	0,25	25,56	0,22	10,87	99,42	19,28	6,98	69,90	50,56	0,09
Sm3d-Ci1	Chromite	0,07	1,83	13,57	46,67	0,26	25,57	0,11	10,72	98,79	19,44	6,81	69,77	50,01	0,09
Sm3g-Ci2	Chromite	0,08	2,44	16,11	40,65	0,28	30,16	0,12	9,00	98,83	23,04	7,91	62,86	41,44	0,11
Sm3g-Ci3	Chromite	0,05	1,93	13,51	45,29	0,23	27,94	0,24	10,20	99,38	20,35	8,44	69,23	47,54	0,11
Sm3g-Ci1	Chromite	0,08	2,03	14,51	44,44	0,20	27,57	0,24	9,90	98,96	20,84	7,48	67,27	46,20	0,10
Sm3a-Cm1	Chromite	0,05	2,57	14,05	40,91	0,32	32,02	0,29	8,24	98,45	23,80	9,13	66,14	38,54	0,13
Sm3b-Cm1	Chromite	0,06	2,00	13,19	45,93	0,20	29,89	0,00	8,09	99,37	23,74	6,84	70,03	38,07	0,09
Sm3c-Cm1	Chromite	0,10	2,76	13,39	41,61	0,27	32,54	0,33	7,35	98,35	25,07	8,30	67,58	34,67	0,12

Analyses de chromites par microsonde (suite)

# Grain	Minéral	SiO ₂	TiO ₂	Al ₂ O ₃	Cr ₂ O ₃	V ₂ O ₅	FeO ^{Total}	MnO	MgO	Total	FeO ^a	Fe ₂ O ₃ ^a	Cr# ^b	Mg# ^c	Fe ³⁺ /R ^{3+, d}
<i>Contenu en % poids</i>															
Sm3g-Cb1	Chromite	0,10	2,34	16,91	40,55	0,33	29,55	0,22	9,35	99,36	22,74	7,57	61,67	42,79	0,10
Jc1b-Ci2	Chromite	0,06	2,72	14,22	43,03	0,38	28,52	0,07	9,95	98,95	21,74	7,54	67,00	45,44	0,11
Jc1b-Ci1	Chromite	0,06	2,66	14,01	42,37	0,41	28,33	0,19	10,68	98,70	20,44	8,77	66,99	48,80	0,12
Jc1a-Ci2	Chromite	0,08	1,89	12,13	49,28	0,26	24,74	0,12	10,44	98,94	19,70	5,60	73,16	49,03	0,08
Jc1a-Ci1	Chromite	0,07	1,62	12,96	48,60	0,22	23,91	0,06	11,30	98,75	18,29	6,25	71,55	52,83	0,08
Jc1a-Ci3	Chromite	0,09	1,66	12,73	48,82	0,24	24,00	0,20	11,30	99,03	18,27	6,37	72,01	52,93	0,09
Jc1d-Ci1	Chromite	0,10	1,92	13,70	48,12	0,24	24,32	0,12	11,02	99,54	19,21	5,68	70,20	51,06	0,08
Jc1d-Ci2	Chromite	0,07	2,54	13,80	46,14	0,44	25,82	0,06	10,72	99,60	20,67	5,72	69,17	48,68	0,08
Jc1c-Cb2	Chromite	0,06	2,50	13,41	46,51	0,43	27,24	0,13	10,06	100,34	21,71	6,15	69,93	45,80	0,09
Jc1c-Cb1	Chromite	0,09	1,88	12,35	48,51	0,19	27,08	0,02	9,60	99,73	21,26	6,48	72,48	44,95	0,09
Jc2a-Ci2	Chromite	0,09	1,73	16,81	45,32	0,22	22,14	0,09	13,57	99,96	15,85	6,98	64,40	60,92	0,09
Jc2a-Ci1	Chromite	1,39	1,70	11,93	37,94	0,17	32,79	0,03	11,07	97,03	19,79	14,44	68,10	53,13	0,23
Jc2c-Ci1	Chromite	0,10	2,03	16,02	43,69	0,30	26,19	0,07	12,01	100,42	18,64	8,39	64,65	54,03	0,11
Jc2c-Ci2	Chromite	0,07	1,92	15,60	44,24	0,23	25,16	0,12	11,78	99,11	18,29	7,63	65,55	53,88	0,10
Jc2a-Cm1	Chromite	0,09	2,21	14,79	43,17	0,25	27,17	0,16	10,71	98,53	19,85	8,14	66,20	49,48	0,11
Jc2b-Cm1	Chromite	0,10	1,84	17,00	44,49	0,24	24,12	0,11	11,99	99,90	18,36	6,40	63,71	54,31	0,09
Jc2a-Cb1	Chromite	0,06	2,18	14,51	41,12	0,24	31,34	0,19	8,27	97,91	23,32	8,91	65,53	39,05	0,12
Jc2b-Cb1	Chromite	0,21	2,09	13,57	45,66	0,28	26,60	0,27	11,14	99,83	19,45	7,95	69,29	51,30	0,11
Jc2d-Cb1	Chromite	0,11	1,56	15,57	48,13	0,25	20,81	0,06	13,88	100,36	15,26	6,17	67,46	62,47	0,08
Jc3c-Ci1	Chromite	0,08	1,50	12,41	48,29	0,21	26,68	0,06	10,53	99,77	19,66	7,80	72,30	49,25	0,10
Jc3c-Ci2	Chromite	0,04	1,42	12,98	47,48	0,20	26,45	0,15	10,67	99,38	19,08	8,18	71,04	50,24	0,11
Jc3a-Ci1	Chromite	0,11	0,77	15,63	49,00	0,13	21,15	0,09	11,85	98,73	16,88	4,74	67,77	56,01	0,06
Jc3a-Ci2	Chromite	0,06	1,79	14,96	45,20	0,28	24,66	0,04	11,46	98,44	18,39	6,97	66,96	53,09	0,09
Jc3d-Cm1	Chromite	0,08	0,96	13,19	50,83	0,10	24,28	0,12	10,61	100,17	18,95	5,93	72,10	50,23	0,08

Analyses de chromites par microsonde (suite)

# Grain	Minéral	SiO ₂	TiO ₂	Al ₂ O ₃	Cr ₂ O ₃	V ₂ O ₅	FeO ^{Total}	MnO	MgO	Total	FeO ^a	Fe ₂ O ₃ ^a	Cr# ^b	Mg# ^c	Fe ³⁺ /R ^{3+, d}
<i>Contenu en % poids</i>															
Jc3b-Cm1	Chromite	0,07	1,43	13,23	49,57	0,21	23,69	0,00	10,99	99,18	18,74	5,50	71,54	51,52	0,07
Jc4b-Ci1	Chromite	0,09	1,71	13,53	49,89	0,22	22,18	0,10	12,28	100,00	17,15	5,59	71,21	56,55	0,07
Jc4b-Ci2	Chromite	0,10	1,68	13,38	49,62	0,23	22,25	0,03	12,24	99,55	17,26	5,55	71,33	56,38	0,08
Jc4a-Ci1	Chromite	0,07	2,01	11,58	48,53	0,34	26,32	0,20	9,05	98,10	21,57	5,28	73,76	43,27	0,08
Jc4a-Ci2	Chromite	0,08	2,07	11,96	49,19	0,33	24,96	0,05	10,25	98,88	20,27	5,21	73,40	47,91	0,07
Jc4d-Cm2	Chromite	0,08	1,97	12,30	49,16	0,32	24,43	0,09	10,96	99,31	19,28	5,72	72,84	50,88	0,08
Jc4d-Cm1	Chromite	0,07	3,11	15,80	39,10	0,46	31,31	0,19	8,97	99,00	23,83	8,32	62,41	40,67	0,12
Jc4c-Cb1	Chromite	0,08	1,71	10,31	51,94	0,23	24,83	0,20	10,23	99,52	19,73	5,67	77,18	48,47	0,08
Jc4b-Cb1	Chromite	0,09	1,74	13,30	48,94	0,22	24,01	0,09	10,76	99,15	19,27	5,26	71,17	50,33	0,07
Jc4a-Cb1	Chromite	0,05	2,15	11,91	48,23	0,36	27,06	0,14	8,82	98,71	22,44	5,13	73,09	41,63	0,07
Jc5a-Ci1	Chromite	0,06	2,51	15,90	42,57	0,45	26,59	0,12	10,19	98,38	21,32	5,85	64,24	46,60	0,08
Jc5b-Ci1	Chromite	0,05	2,69	15,17	44,04	0,50	25,55	0,06	10,64	98,69	20,78	5,30	66,07	48,34	0,08
Jc5c-Cm1	Chromite	0,04	2,70	15,79	43,15	0,45	26,91	0,10	10,44	99,57	21,45	6,07	64,70	47,01	0,09
Jc6b-Ci2	Chromite	0,07	3,24	12,20	41,96	0,39	31,47	0,15	9,17	98,65	22,97	9,44	69,76	42,06	0,14
Jc6c-Ci1	Chromite	0,09	1,37	13,84	51,91	0,23	20,90	0,00	11,96	100,30	17,66	3,60	71,56	55,20	0,05
Jc6b-Ci3	Chromite	0,04	2,87	12,34	42,41	0,41	31,75	0,19	8,89	98,89	23,10	9,62	69,75	41,14	0,14
Jc6d-Cm1	Chromite	0,06	1,78	12,60	44,99	0,21	32,91	0,26	5,72	98,53	26,51	7,11	70,55	28,00	0,10
Jc6e-Cb1	Chromite	0,05	3,81	10,82	37,80	0,55	38,20	0,26	7,03	98,52	26,72	12,76	70,09	32,41	0,19
Jc6b-Cb1	Chromite	0,05	3,99	12,49	38,80	0,57	34,54	0,11	8,76	99,30	24,79	10,84	67,58	39,23	0,16
Jc6a-Cb1	Chromite	0,01	4,69	10,01	36,33	0,46	38,76	0,15	7,46	97,86	26,41	13,72	70,90	33,87	0,21
Jc6a-Cb2	Chromite	0,05	5,07	9,50	35,91	0,50	39,97	0,15	7,52	98,67	27,01	14,40	71,72	33,63	0,22
Jc6a-Cb3	Chromite	0,05	4,09	10,38	38,94	0,51	36,36	0,19	7,87	98,39	25,47	12,10	71,56	36,00	0,18
Jc7d-Ci1	Chromite	0,09	1,94	13,18	48,49	0,23	23,56	0,02	12,07	99,58	17,75	6,46	71,16	55,31	0,09
Jc7a-Cm1	Chromite	0,08	2,20	11,67	48,34	0,31	27,00	0,14	10,26	99,99	20,60	7,11	73,54	47,53	0,10

Analyses de chromites par microsonde (suite)

# Grain	Minéral	SiO ₂	TiO ₂	Al ₂ O ₃	Cr ₂ O ₃	V ₂ O ₅	FeO ^{Total}	MnO	MgO	Total	FeO ^a	Fe ₂ O ₃ ^a	Cr# ^b	Mg# ^c	Fe ³⁺ /R ^{3+, d}
<i>Contenu en % poids</i>															
Jc7b-Cm1	Chromite	0,09	1,58	13,23	50,60	0,26	23,16	0,06	11,40	100,37	18,71	4,95	71,95	52,58	0,07
Jc7a-Cb1	Chromite	0,05	1,90	13,23	48,21	0,25	25,09	0,10	10,98	99,81	19,36	6,36	70,97	50,68	0,09
Jc7c-Cb1	Chromite	0,07	1,94	12,38	49,08	0,28	24,25	0,03	11,33	99,36	18,67	6,20	72,68	52,45	0,09
Jc7c-Cb2	Chromite	0,08	2,07	12,28	47,67	0,25	28,11	0,14	9,23	99,83	22,00	6,79	72,25	43,17	0,09
Jc7d-Cb1	Chromite	0,06	2,94	14,46	42,39	0,36	27,49	0,06	11,62	99,38	19,57	8,80	66,29	51,98	0,12
Et2d-Ci1	Chromite	1,03	2,85	11,01	41,27	0,28	31,50	0,13	10,20	98,27	21,86	10,71	71,55	47,67	0,17
Et2d-Ci2	Chromite	0,14	3,26	12,09	43,80	0,37	28,99	0,16	10,45	99,26	21,26	8,59	70,84	47,35	0,12
Et2b-Ci1	Chromite	0,08	2,38	10,68	47,91	0,28	28,44	0,20	9,35	99,31	21,68	7,50	75,06	43,90	0,11
Et2d-Cb2	Chromite	0,06	3,51	11,03	41,97	0,36	36,33	0,18	5,85	99,29	28,28	8,95	71,85	27,22	0,13
Et2c-Cb1	Chromite	0,10	1,85	10,53	49,74	0,17	28,30	0,07	8,50	99,26	22,41	6,54	76,02	40,67	0,09
Et2b-Cb2	Chromite	0,07	2,10	10,14	48,64	0,22	30,08	0,00	7,57	98,81	23,94	6,83	76,30	36,35	0,10
Et2b-Cb1	Chromite	0,20	1,90	9,57	49,45	0,20	29,64	0,10	7,62	98,67	23,61	6,71	77,61	37,00	0,10
Et2a-Cb1	Chromite	0,07	3,08	10,32	43,52	0,32	34,69	0,23	5,98	98,21	27,06	8,48	73,88	28,56	0,13
Et2a-Cb2	Chromite	0,18	3,57	10,02	43,02	0,31	34,67	0,36	6,23	98,36	27,10	8,41	74,22	29,50	0,13
Et3c-Ci1	Chromite	0,09	2,17	10,85	48,36	0,32	27,40	0,05	9,01	98,24	21,94	6,06	74,93	42,74	0,09
Et3a-Ci1	Chromite	0,08	1,82	10,58	49,69	0,21	27,66	0,14	8,79	98,97	21,75	6,57	75,90	42,21	0,09
Et3d-Cm2	Chromite	0,11	2,26	9,72	48,26	0,23	30,92	0,27	6,96	98,72	24,81	6,79	76,91	33,66	0,10
Et3d-Cm1	Chromite	0,07	2,89	9,88	46,18	0,29	32,91	0,07	6,82	99,10	26,04	7,63	75,83	32,12	0,11
Et3b-Cm1	Chromite	0,65	2,70	9,96	44,50	0,27	34,59	0,17	6,00	98,82	27,67	7,70	74,99	28,82	0,13
Et3d-Cb1	Chromite	0,13	2,75	11,36	44,24	0,24	32,26	0,30	7,28	98,56	25,08	7,98	72,31	34,48	0,12
Et3d-Cb2	Chromite	0,08	2,73	10,49	45,45	0,25	33,12	0,24	7,02	99,37	25,47	8,50	74,40	33,23	0,12
Et3b-Cb1	Chromite	0,07	2,45	10,73	46,28	0,27	30,92	0,02	7,40	98,14	24,50	7,14	74,32	35,33	0,10
Et3a-Cb1	Chromite	0,07	2,21	9,98	47,93	0,24	30,52	0,20	7,19	98,34	24,43	6,76	76,31	34,72	0,10
Et4d-Ci1	Chromite	0,10	1,29	10,39	53,67	0,09	22,11	0,09	12,37	100,11	16,08	6,70	77,61	58,20	0,09

Analyses de chromites par microsonde (suite)

# Grain	Minéral	SiO ₂	TiO ₂	Al ₂ O ₃	Cr ₂ O ₃	V ₂ O ₅	FeO ^{Total}	MnO	MgO	Total	FeO ^a	Fe ₂ O ₃ ^a	Cr# ^b	Mg# ^c	Fe ³⁺ /R ^{3+, d}
<i>Contenu en % poids</i>															
Et4d-Ci2	Chromite	0,11	1,36	10,77	51,89	0,16	23,63	0,16	11,25	99,33	17,73	6,55	76,37	53,52	0,09
Et4a-Cm1	Chromite	0,08	2,08	10,98	47,78	0,23	26,16	0,15	10,83	98,28	18,80	8,18	74,48	51,11	0,11
Et4b-Cm1	Chromite	0,07	1,54	11,34	52,56	0,17	20,98	0,23	12,75	99,64	15,70	5,87	75,66	59,54	0,08
Et4d-Cm1	Chromite	0,10	1,59	10,84	49,99	0,15	26,56	0,18	9,50	98,91	20,46	6,78	75,57	45,63	0,09
Et4c-Cb1	Chromite	0,09	1,69	9,69	51,23	0,21	26,77	0,00	10,22	99,91	19,94	7,59	78,01	48,18	0,10
Et4d-Cb1	Chromite	0,08	1,51	10,68	52,38	0,14	22,01	0,13	12,52	99,46	15,92	6,77	76,69	58,75	0,09

^a FeO et Fe₂O₃ ont été obtenues à partir de calculs stoechiométriques en utilisant les équations de Barnes and Roeder (2001).

^b Cr# = 100 * Cr / (Cr + Al).

^c Mg# = 100 * Mg / (Mg + Fe²⁺).

^d Fe³⁺/R³⁺ = Fe³⁺ / (Cr + Al + Fe³⁺).

Analyses de bordures de surcroissance de chromite

# Grain	Minéral	SiO ₂	TiO ₂	Al ₂ O ₃	Cr ₂ O ₃	V ₂ O ₅	FeO ^{Total}	MnO	MgO	Total	FeO ^a	Fe ₂ O ₃ ^a	Cr# ^b	Mg# ^c	Fe ³⁺ /R ^{3+, d}
<i>Contenu en % poids</i>															
Bc2b-Cmf1	Ox. Fe-Ti	0,03	5,11	6,04	14,04	0,31	63,37	0,74	3,45	93,08	30,39	36,64	60,95	16,98	0,60
Bc2c-Cbf1	Ox. Fe-Ti	0,05	8,33	5,15	6,65	0,56	65,80	0,35	4,62	91,51	31,72	37,87	46,41	20,92	0,72
Bc4e-Cbf1	Ox. Fe-Ti	0,06	7,73	5,78	11,39	0,53	64,36	0,34	3,70	93,89	33,21	34,62	56,95	16,81	0,63
Bc5c-Cmf1	Ox. Fe-Ti	0,14	2,93	7,51	22,66	0,35	53,52	0,29	7,00	94,40	24,20	32,59	66,93	34,53	0,48
Bc6a-Cmf1	Ox. Fe-Ti	0,22	5,42	6,90	23,30	0,42	50,54	4,54	0,38	91,71	31,40	21,27	69,37	2,14	0,38
Bc7f-Cmf1	Ox. Fe-Ti	0,08	8,56	4,87	11,84	0,70	64,78	0,89	2,34	94,07	35,76	32,25	61,97	10,67	0,62
Dl2b-Cmf1	Ox. Fe-Ti	0,28	9,35	6,51	13,15	0,68	62,82	0,54	0,74	94,07	39,69	25,70	57,53	3,31	0,53
Dl3a-Cmf1	Ox. Fe-Ti	0,13	14,84	2,75	4,46	0,77	69,25	0,13	0,06	92,38	44,69	27,30	52,16	0,23	0,76
Dl6c-Cmf1	Ox. Fe-Ti	0,20	7,51	7,22	12,10	0,66	62,95	1,39	0,17	92,19	37,47	28,32	52,91	0,82	0,55
Dj3c-Cbf1	Ox. Fe-Ti	0,09	17,58	2,99	4,89	0,84	63,70	1,47	0,25	91,82	44,87	20,93	52,35	1,01	0,69
Dj3g-Cmf1	Ox. Fe-Ti	0,06	16,98	4,04	10,02	0,70	59,79	1,20	1,15	93,94	44,15	17,37	62,44	4,50	0,52
Dj4e-Cbf1	Ox. Fe-Ti	0,06	20,04	3,41	6,71	0,68	60,93	1,12	0,63	93,59	47,69	14,72	56,90	2,33	0,56
Dj5e-Cbf1	Ox. Fe-Ti	0,05	18,99	3,57	9,17	0,70	59,59	1,62	0,13	93,83	47,04	13,95	63,29	0,51	0,49
Dj6e-Cbf1	Ox. Fe-Ti	0,07	16,26	5,45	13,41	0,67	58,93	0,88	1,37	97,04	44,84	15,66	62,26	5,23	0,42
Dj6f-Cmf1	Ox. Fe-Ti	0,08	20,30	3,36	7,26	0,77	62,42	1,27	0,27	95,73	49,17	14,73	59,19	0,99	0,55
Dj8b-Cmf1	Ox. Fe-Ti	0,07	17,93	3,92	9,70	0,65	56,59	1,64	1,85	92,35	43,11	14,99	62,41	7,20	0,49
Dj9a-Cmf1	Ox. Fe-Ti	0,32	11,64	3,96	10,64	0,62	61,73	0,90	2,24	92,05	37,97	26,40	64,30	9,78	0,61
Sm2a-Cbf1	Ox. Fe-Ti	0,19	11,41	4,45	12,93	0,56	60,19	0,69	3,18	93,60	36,84	25,96	66,08	13,58	0,57
Sm2e-Cmf1	Ox. Fe-Ti	0,50	10,98	3,54	12,71	0,63	62,37	1,18	1,68	93,59	38,62	26,39	70,67	7,45	0,60
Sm3c-Cmf1	Ox. Fe-Ti	0,03	13,06	4,26	16,26	0,55	56,58	0,84	2,93	94,51	38,48	20,12	71,92	12,11	0,47
Sm3b-Cmf1	Ox. Fe-Ti	0,05	15,60	3,32	8,06	0,67	62,14	1,28	1,10	92,21	42,54	21,78	61,93	4,46	0,62
Sm3a-Cmf1	Ox. Fe-Ti	0,05	9,52	5,33	24,90	0,51	49,00	0,19	6,07	95,58	31,63	19,30	75,82	25,83	0,37
Jc2b-Cmf1	Ox. Fe-Ti	1,00	20,69	3,65	7,38	0,90	58,42	0,97	0,84	93,84	49,75	9,63	57,57	3,05	0,48
Jc3d-Cmf1	Ox. Fe-Ti	0,30	16,72	3,49	11,51	0,80	59,78	1,06	0,29	93,93	46,02	15,29	68,89	1,12	0,49

Analyses de bordures de surcroissance de chromite (suite)

# Grain	Minéral	SiO ₂	TiO ₂	Al ₂ O ₃	Cr ₂ O ₃	V ₂ O ₅	FeO ^{Total}	MnO	MgO	Total	FeO ^a	Fe ₂ O ₃ ^a	Cr# ^b	Mg# ^c	Fe ³⁺ /R ^{3+, d}
<i>Contenu en % poids</i>															
Jc6d-Cmf1	Ox. Fe-Ti	0,49	13,72	3,14	8,71	1,02	63,85	0,81	1,48	93,23	42,05	24,23	65,04	6,13	0,65
Et2c-Cbf1	Ox. Fe-Ti	0,07	17,51	1,85	2,83	1,54	68,36	0,07	0,44	92,67	47,77	22,88	50,57	1,68	0,81
Et3d-Cmf1	Ox. Fe-Ti	0,12	22,49	4,56	5,92	0,92	59,17	0,92	0,65	94,74	50,86	9,23	46,54	2,26	0,44
Et3b-Cbf1	Ox. Fe-Ti	0,17	19,62	3,92	6,10	1,02	59,94	0,66	0,64	92,06	48,04	13,23	51,10	2,38	0,54
Et3b-Cmf1	Ox. Fe-Ti	0,10	20,34	4,14	3,49	0,99	62,05	0,64	0,19	91,94	48,89	14,62	36,10	0,71	0,61
Et4a-Cmf1	Ox. Fe-Ti	0,11	15,32	2,10	2,63	1,02	69,02	0,46	0,12	90,77	44,60	27,14	45,65	0,49	0,82
Et4b-Cmf1	Ox. Fe-Ti	0,13	12,44	2,64	6,78	0,98	67,57	0,85	0,02	91,40	42,00	28,42	63,27	0,08	0,72

^a FeO et Fe₂O₃ ont été obtenues à partir de calculs stoechiométriques en utilisant les équations de Barnes and Roeder (2001).

^b Cr# = 100 * Cr / (Cr + Al).

^c Mg# = 100 * Mg / (Mg + Fe²⁺).

^d Fe³⁺/R³⁺ = Fe³⁺ / (Cr + Al + Fe³⁺).

Analyses d'olivines par microsonde

# Grain	Minéral *	SiO ₂	Al ₂ O ₃	Cr ₂ O ₃	FeO ^{Total}	MnO	MgO	CaO	NiO	Total	Fo (% mol.)
<i>Contenu en % poids</i>											
Bc2e-O1	Olivine	41,17	0,07	0,14	7,54	0,13	50,58	0,32	0,43	100,39	92,28
Bc2e-OB1	Olivine (bord.)	40,67	0,08	0,05	9,09	0,15	49,92	0,28	0,38	100,63	90,73
Bc2f-O1	Olivine	41,02	0,07	0,12	8,07	0,13	50,45	0,31	0,31	100,46	91,77
Bc4d-O1	Olivine	40,93	0,09	0,12	9,47	0,18	49,30	0,36	0,37	100,81	90,27
Bc4e-O1	Olivine	41,16	0,09	0,11	9,20	0,19	49,67	0,39	0,36	101,17	90,59
Bc4f-O1	Olivine	41,32	0,07	0,07	8,10	0,14	50,69	0,33	0,40	101,12	91,77
Bc4f-OB1	Olivine (bord.)	39,60	0,08	0,13	13,14	0,28	45,89	0,31	0,31	99,72	86,17
Bc5a-O1	Olivine	39,81	0,08	0,08	9,05	0,13	47,28	0,32	0,35	97,09	90,30
Bc5d-O1	Olivine	41,08	0,12	0,15	7,33	0,15	50,26	0,29	0,39	99,77	92,44
Bc6c-O1	Olivine	40,82	0,06	0,11	9,92	0,16	48,92	0,36	0,34	100,68	89,79
Bc6d-O1	Olivine	40,88	0,10	0,08	7,87	0,11	50,68	0,31	0,36	100,39	91,99
Bc7a-O1	Olivine	40,36	0,02	0,06	12,94	0,18	46,64	0,42	0,29	100,90	86,53
Bc7c-O1	Olivine	40,39	0,04	0,04	11,24	0,21	47,61	0,43	0,33	100,29	88,31
Bc7g-O1	Olivine	40,67	0,07	0,00	11,36	0,21	48,07	0,48	0,25	101,11	88,29
Dl2c-O1	Olivine	41,04	0,08	0,19	9,49	0,11	49,89	0,28	0,37	101,45	90,35
Dl2d-O1	Olivine	40,92	0,10	0,04	10,73	0,19	48,64	0,33	0,40	101,35	88,99
Dl3b-O1	Olivine	39,70	0,09	0,14	15,03	0,24	44,37	0,40	0,33	100,29	84,03
Dl3d-O1	Olivine	40,19	0,05	0,12	14,38	0,22	45,22	0,44	0,33	100,95	84,86
Dl3e-O1	Olivine	40,78	0,04	0,14	10,16	0,13	49,17	0,48	0,34	101,26	89,61
Dl6a-O1	Olivine	41,43	0,09	0,17	6,99	0,11	51,14	0,25	0,44	100,62	92,88
Dl6b-O1	Olivine	40,25	0,04	0,00	13,92	0,24	45,34	0,44	0,28	100,52	85,31
Dj3a-O1	Olivine	40,68	0,05	0,05	10,15	0,15	48,57	0,29	0,37	100,30	89,51
Dj3e-O1	Olivine	40,21	0,05	0,11	11,67	0,21	47,16	0,37	0,37	100,16	87,81
Dj4b-O1	Olivine	40,36	0,03	0,11	10,91	0,16	48,02	0,42	0,30	100,31	88,69

Analyses d'olivines par microsonde (suite)

# Grain	Minéral *	SiO ₂	Al ₂ O ₃	Cr ₂ O ₃	FeO ^{Total}	MnO	MgO	CaO	NiO	Total	Fo (% mol.)
<i>Contenu en % poids</i>											
Dj4e-O1	Olivine	40,27	0,03	0,05	13,01	0,16	46,68	0,48	0,29	100,97	86,48
Dj5a-O1	Olivine	39,81	0,04	0,12	10,04	0,15	45,14	0,30	0,29	95,88	88,91
Dj5d-O1	Olivine	39,88	0,03	0,08	14,51	0,20	44,90	0,40	0,30	100,30	84,66
Dj6c-O1	Olivine	40,61	0,04	0,06	11,36	0,17	47,31	0,47	0,33	100,35	88,13
Dj6e-O1	Olivine	40,36	0,04	0,04	12,76	0,22	46,56	0,48	0,32	100,77	86,68
Dj8a-O1	Olivine	40,60	0,04	0,06	11,53	0,16	47,82	0,38	0,30	100,89	88,09
Dj8b-O1	Olivine	40,35	0,05	0,08	11,87	0,23	47,19	0,46	0,30	100,52	87,64
Dj8c-O1	Olivine	40,31	0,04	0,11	12,02	0,19	46,50	0,48	0,32	99,98	87,34
Dj9b-O1	Olivine	40,59	0,01	0,00	11,16	0,18	47,63	0,41	0,29	100,26	88,38
Dj9c-O1	Olivine	40,23	0,04	0,00	13,21	0,18	46,48	0,40	0,34	100,88	86,25
Dj9f-O1	Olivine	40,32	0,05	0,08	12,70	0,21	46,56	0,39	0,26	100,59	86,72
Sm2C-O1	Olivine	40,46	0,05	0,00	11,70	0,22	47,66	0,37	0,26	100,72	87,90
Sm2g-O1	Olivine	40,20	0,03	0,05	13,49	0,25	46,26	0,50	0,26	101,04	85,94
Sm2h-O1	Olivine	40,90	0,04	0,00	11,27	0,16	48,00	0,41	0,29	101,07	88,36
Sm2i-O1	Olivine	39,93	0,05	0,05	14,87	0,23	44,54	0,44	0,29	100,40	84,23
Sm3d-O1	Olivine	40,24	0,04	0,06	10,32	0,18	47,33	0,42	0,30	98,89	89,10
Sm3f-O1	Olivine	40,42	0,02	0,05	11,02	0,18	47,12	0,34	0,37	99,51	88,40
Sm3g-O1	Olivine	39,86	0,04	0,00	11,31	0,19	46,46	0,39	0,36	98,61	87,98
Jc1d-O1	Olivine	39,90	0,06	0,04	13,62	0,21	44,42	0,38	0,34	98,97	85,32
Jc1b-O1	Olivine	39,38	0,05	0,04	14,56	0,24	44,23	0,37	0,29	99,16	84,41
Jc1a-O1	Olivine	40,20	0,04	0,11	10,91	0,14	47,43	0,36	0,36	99,54	88,57
Jc1a-O2	Olivine	40,47	0,05	0,08	11,74	0,16	46,53	0,33	0,35	99,70	87,60
Jc2a-O1	Olivine	40,20	0,06	0,05	12,47	0,20	45,86	0,48	0,31	99,61	86,77
Jc2a-O2	Olivine	40,42	0,03	0,07	11,01	0,15	47,32	0,38	0,33	99,71	88,45

Analyses d'olivines par microsonde (suite)

# Grain	Minéral *	SiO ₂	Al ₂ O ₃	Cr ₂ O ₃	FeO ^{Total}	MnO	MgO	CaO	NiO	Total	Fo (% mol.)
<i>Contenu en % poids</i>											
Jc2d-O1	Olivine	40,86	0,07	0,11	10,06	0,18	48,43	0,34	0,37	100,41	89,57
Jc3c-O1	Olivine	40,03	0,04	0,00	12,88	0,21	45,66	0,46	0,23	99,50	86,34
Jc3c-O1	Olivine	40,51	0,02	0,16	10,47	0,18	48,28	0,34	0,39	100,35	89,16
Jc4b-O1	Olivine	40,17	0,07	0,14	11,54	0,14	46,93	0,33	0,29	99,60	87,88
Jc4a-O1	Olivine	39,82	0,04	0,07	13,41	0,23	45,17	0,33	0,33	99,41	85,72
Jc5a-O1	Olivine	39,11	0,04	0,09	14,20	0,23	43,12	0,32	0,27	97,38	84,41
Jc5b-O1	Olivine	39,27	0,02	0,05	15,05	0,21	43,87	0,29	0,34	99,11	83,87
Jc6c-O1	Olivine	41,06	0,04	0,11	8,63	0,14	49,76	0,28	0,27	100,29	91,13
Jc6b-O1	Olivine	39,45	0,04	0,03	16,63	0,28	43,25	0,28	0,29	100,24	82,26
Jc6a-O1	Olivine	38,88	0,04	0,08	16,08	0,25	42,35	0,26	0,29	98,24	82,44
Jc7d-O1	Olivine	40,62	0,03	0,09	11,47	0,16	47,51	0,34	0,32	100,54	88,07
Et2d-O1	Olivine	40,39	0,03	0,00	13,34	0,22	45,00	0,29	0,26	99,53	85,74
Et2c-O1	Olivine	40,36	0,04	0,11	12,67	0,14	46,44	0,22	0,37	100,35	86,73
Et2b-O1	Olivine	39,26	0,03	0,07	13,40	0,19	44,74	0,26	0,33	98,28	85,62
Et3c-O1	Olivine	40,19	0,01	0,10	12,93	0,18	45,94	0,25	0,33	99,91	86,37
Et3a-O1	Olivine	39,68	0,04	0,03	12,17	0,19	46,27	0,23	0,37	98,99	87,14
Bc4h-Om1	Olivine	39,32	0,61	0,35	16,68	0,28	41,92	2,17	0,28	101,60	75,57
Bc5b-Om1	Olivine	39,66	0,03	0,06	13,98	0,29	44,57	0,39	0,24	99,21	79,69
Bc6d-Om1	Olivine	39,69	0,05	0,02	16,40	0,32	43,95	0,38	0,24	101,04	76,74
Bc7d-Om1	Olivine	39,46	0,03	0,00	15,52	0,30	44,21	0,36	0,23	100,11	77,81
Dl2a-Om1	Olivine	39,82	0,04	0,00	15,06	0,25	44,11	0,40	0,27	99,96	78,28
Dj8d-Om1	Olivine	40,04	0,06	0,11	15,06	0,28	44,97	0,49	0,29	101,29	78,61
Dj9d-Om1	Olivine	39,32	0,03	0,00	17,86	0,31	42,60	0,28	0,27	100,68	74,59

Analyses d'olivines par microsonde (suite)

# Grain	Minéral *	SiO ₂	Al ₂ O ₃	Cr ₂ O ₃	FeO ^{Total}	MnO	MgO	CaO	NiO	Total	Fo (% mol.)
<i>Contenu en % poids</i>											
Dl4c-AlO1	Olivine (serp.)	58,03	1,73	0,13	6,37	0,04	26,60	0,20	0,35	93,45	83,71
Dl4d-AlO1	Olivine (serp.)	59,22	1,27	0,12	5,23	0,04	27,50	0,15	0,40	93,92	86,63

* bord., bordure; serp., serpentinitisée.

Analyses de clinopyroxènes

# Grain	Mineral	SiO ₂	TiO ₂	Al ₂ O ₃	Cr ₂ O ₃	FeO ^{Total}	MnO	MgO	CaO	Na ₂ O	Total	Mg# ^a	Cr# ^b
<i>Contenu en % poids</i>													
Dl2a-Cxm1	Diopside	49,76	0,81	5,33	1,02	5,55	0,13	15,52	22,22	0,24	100,58	90,75	11,39
Dl3e-Cxm1	Diopside	50,10	1,11	5,53	0,72	5,88	0,10	15,12	22,00	0,31	100,88	86,61	8,05
Dl4b-Cxm1	Diopside	51,04	0,63	4,81	1,10	4,81	0,10	15,87	22,29	0,26	100,91	89,22	13,25
Dl4b-Cxm2	Diopside	49,53	0,83	5,29	1,66	4,55	0,13	15,71	21,81	0,32	99,82	92,17	17,36
Dj6a-Cxm1	Diopside	52,55	0,92	2,31	0,89	4,21	0,08	16,80	22,75	0,30	100,81	90,80	20,54
Dj8f-Cxm1	Diopside	49,07	1,35	4,32	0,27	8,11	0,19	14,46	21,03	0,42	99,22	83,83	4,02
Dj9d-Cxm1	Diopside	50,75	0,62	3,35	1,08	4,99	0,14	16,66	22,18	0,21	99,98	93,80	17,72
Sm3a-Cxm1	Diopside	49,53	0,89	3,83	1,07	5,10	0,10	15,50	22,88	0,39	99,28	95,98	15,84
Dl1d-Cxm1	Diopside	50,42	0,74	4,25	0,12	6,67	0,15	14,56	22,52	0,39	99,81	86,09	1,81
Sm4c-Cxm1	Diopside	52,47	0,64	1,94	0,26	3,62	0,05	16,67	24,28	0,24	100,17	95,81	8,38
Bc4a-Cx1	Diopside	51,76	0,50	3,82	0,12	4,96	0,09	16,02	23,22	0,26	100,75	91,35	2,10
Dj4b-Cx1	Diopside	50,83	1,13	2,89	0,71	4,43	0,09	16,52	22,78	0,28	99,65	94,48	14,07
Dj5c-Cx1	Diopside	51,01	1,04	3,05	1,02	4,49	0,09	16,56	22,67	0,30	100,22	94,14	18,26
Dj6b-Cx1	Diopside	51,61	0,97	3,08	1,39	3,89	0,08	16,27	23,00	0,31	100,58	91,75	23,24
Dj8e-Cx1	Diopside	51,00	0,82	3,40	1,24	3,99	0,16	15,84	23,16	0,40	100,01	94,08	19,58
Sm2f-Cx1	Diopside	50,82	0,64	2,95	1,01	4,67	0,10	16,68	22,69	0,27	99,81	96,32	18,65
Sm3e-Cx1	Diopside	50,35	0,84	3,22	0,55	4,30	0,11	16,32	22,68	0,24	98,62	94,84	10,25
Jc1a-Cx1	Augite	51,89	0,64	2,18	0,66	4,98	0,08	17,38	21,35	0,23	99,37	90,84	17,00
Jc3c-Cx1	Diopside	50,76	0,88	3,97	1,09	4,63	0,08	15,98	22,52	0,30	100,20	91,51	15,62
Jc4d-Cx1	Diopside	51,40	0,87	3,19	0,66	5,20	0,07	16,44	21,56	0,31	99,70	88,64	12,16
Jc4a-Cx1	Diopside	50,54	0,74	3,45	1,07	5,15	0,10	16,33	21,99	0,29	99,66	92,53	17,20
Jc5b-Cx1	Augite	50,36	0,91	3,40	1,22	5,12	0,08	16,56	20,87	0,25	98,77	89,37	19,45
Jc6b-Cx1	Diopside	51,40	0,78	2,71	1,01	5,06	0,13	16,84	21,71	0,26	99,89	91,16	19,97
Et4b-Cx1	Diopside	50,63	0,80	3,10	0,78	6,13	0,13	16,33	21,14	0,27	99,32	88,90	14,50

Analyses de clinopyroxènes (suite)

# Grain	Mineral	SiO ₂	TiO ₂	Al ₂ O ₃	Cr ₂ O ₃	FeO ^{Total}	MnO	MgO	CaO	Na ₂ O	Total	Mg# ^a	Cr# ^b
<i>Contenu en % poids</i>													
Et4b-Cx2	Augite	51,65	0,81	2,79	0,78	6,10	0,17	16,52	21,01	0,28	100,10	86,40	15,86
Dl1d-Cx1	Diopside	50,83	0,55	3,27	0,16	6,98	0,13	15,06	22,22	0,39	99,59	87,01	3,21
Dj1c-Cx1	Diopside	49,76	1,67	5,02	0,42	5,83	0,09	14,61	23,04	0,37	100,80	87,84	5,29
Dj7a-Cx1	Diopside	52,14	0,61	2,24	1,05	3,54	0,05	16,35	23,86	0,32	100,16	94,59	23,92
Dj7b-Cx1	Diopside	50,58	1,14	3,83	0,18	5,66	0,10	14,89	22,96	0,36	99,69	87,59	3,01
Dj7c-Cx1	Diopside	50,38	0,76	3,07	0,84	4,62	0,13	15,61	23,51	0,29	99,19	94,92	15,45
Dj7c-Cx2	Diopside	52,46	0,44	2,31	0,87	3,92	0,07	16,61	23,41	0,29	100,38	93,41	20,25
Dj10a-Cx1	Diopside	50,13	0,87	3,63	0,56	5,38	0,12	15,86	22,64	0,26	99,44	93,17	9,44
Dj10a-Cx2	Diopside	51,55	0,74	3,68	0,30	5,64	0,10	16,00	22,57	0,23	100,81	88,59	5,26
Sm1d-Cx1	Diopside	50,60	0,97	3,56	0,25	4,91	0,09	15,41	23,45	0,32	99,54	92,35	4,48
Sm1c-Cx1	Diopside	53,44	0,37	1,49	0,43	3,53	0,09	17,07	23,82	0,31	100,53	94,54	16,16
Sm4c-Cx1	Diopside	52,18	0,50	2,06	0,32	3,82	0,10	16,42	24,38	0,29	100,07	97,09	9,51
Bc4g-Cxma1	Diopside	49,95	0,68	5,03	0,36	6,35	0,10	14,85	22,59	0,49	100,40	91,31	4,63
Bc6a-Cxma1	Diopside	49,88	0,94	4,80	0,22	7,80	0,13	14,65	21,98	0,36	100,75	85,72	3,04
Bc7f-Cxma1	Diopside	50,44	0,61	4,47	0,50	6,03	0,12	15,60	22,28	0,38	100,42	91,58	6,92
Dl2f-Cxma1	Diopside	51,68	0,66	3,85	0,41	5,73	0,12	16,09	22,25	0,26	101,05	88,24	6,65
Dl3a-Cxma1	Diopside	49,41	1,04	5,12	1,31	5,33	0,12	15,84	21,19	0,29	99,64	90,08	14,64
Dl4g-Cxma1	Diopside	51,10	0,51	4,12	1,29	5,04	0,11	16,37	22,02	0,25	100,79	90,95	17,33
Dl6b-Cxma1	Diopside	50,92	0,66	3,84	0,53	5,74	0,13	16,04	22,22	0,22	100,31	89,89	8,50
Dj3d-Cxma1	Diopside	50,49	1,33	3,76	0,42	7,67	0,19	15,99	20,79	0,52	101,14	88,25	6,91
Dj4c-Cxma1	Augite	52,31	1,03	2,45	0,49	5,11	0,13	16,77	21,80	0,24	100,33	87,22	11,88
Dj5c-Cxma1	Diopside	50,19	1,18	3,76	1,15	5,83	0,10	15,85	22,18	0,33	100,58	91,09	17,03
Dj9d-Cxma1	Augite	52,50	0,55	1,61	0,77	5,25	0,10	18,53	20,32	0,02	99,64	89,26	24,23
Sm2f-Cxma1	Diopside	51,52	0,59	2,18	0,82	4,94	0,13	17,27	22,18	0,22	99,87	94,73	20,22

Analyses de clinopyroxènes (suite)

# Grain	Mineral	SiO ₂	TiO ₂	Al ₂ O ₃	Cr ₂ O ₃	FeO ^{Total}	MnO	MgO	CaO	Na ₂ O	Total	Mg# ^a	Cr# ^b
<i>Contenu en % poids</i>													
Sm3e-Cxma1	Diopside	50,26	0,92	3,13	1,19	4,63	0,10	16,40	21,65	0,27	98,55	91,97	20,39
Jc1c-Cxma1	Diopside	49,90	1,18	3,85	0,99	5,37	0,15	15,73	21,55	0,33	99,02	89,17	14,67
Jc2c-Cxma1	Diopside	48,85	1,49	4,89	0,11	7,64	0,19	14,21	21,47	0,38	99,23	84,17	1,53
Jc3b-Cxma1	Diopside	50,78	0,68	3,88	1,48	4,55	0,09	16,01	22,32	0,29	100,06	91,27	20,37
Jc4c-Cxma1	Augite	51,06	1,06	3,31	0,33	6,24	0,14	16,67	20,47	0,26	99,52	86,44	6,19
Jc6d-Cxma1	Augite	50,85	0,95	3,41	1,09	5,64	0,15	16,33	20,86	0,27	99,55	86,80	17,59
Et2b-Cxma1	Augite	50,27	1,67	3,21	0,67	6,87	0,15	15,88	20,79	0,28	99,79	84,58	12,26
Et3c-Cxma1	Diopside	50,74	1,30	3,07	0,91	6,04	0,13	16,03	21,35	0,28	99,86	86,48	16,57
Et4a-Cxma1	Augite	50,00	1,01	3,92	0,26	7,19	0,15	15,77	20,57	0,29	99,16	85,75	4,20
Dj2d-Cxma1	Diopside	49,03	1,38	4,93	0,50	6,45	0,16	14,98	21,70	0,35	99,45	88,12	6,31
Dj10c-Cxma1	Diopside	51,77	0,71	2,90	0,49	5,62	0,10	16,61	22,39	0,22	100,81	90,60	10,20
Sm1b-Cxma1	Diopside	48,38	1,92	4,93	0,04	7,94	0,15	13,41	22,41	0,40	99,57	82,80	0,49

^a Mg# = 100 * Mg / (Mg + Fe²⁺).^b Cr# = 100 * Cr / (Cr + Al).

Analyses de plagioclases

# Grain	Minéral	SiO ₂	Al ₂ O ₃	FeO ^{Total}	MgO	CaO	Na ₂ O	K ₂ O	Total	An (%)
<i>Contenu en % poids</i>										
Bc2e-Pma1	Oligoclase	61,60	21,34	1,18	0,76	3,37	7,59	2,80	98,63	16,47
Bc3c-Pma1	Albite	67,02	19,31	0,31	0,03	0,12	11,70	0,06	98,53	0,55
Bc3e-P2	Albite	67,84	19,09	0,04	0,00	0,13	11,65	0,08	98,82	0,60
Bc5d-Pma1	Labradorite	49,46	29,36	1,51	0,09	13,62	3,57	0,50	98,11	65,85
Dl1e-P1	Albite	52,07	31,16	1,23	0,24	0,61	3,26	7,43	96,01	3,99
Dl1e-Pma1	Albite	60,35	24,97	1,11	0,18	1,11	7,63	3,43	98,76	5,85
Dl3a-Pma1	Labradorite	50,07	29,38	1,24	0,63	14,01	3,53	0,13	98,97	68,17
Dl4g-Pma1	Bytownite	50,02	30,19	0,93	0,68	14,42	3,29	0,11	99,64	70,33
Dl5a-P1	Labradorite	51,68	29,49	1,26	0,33	10,66	3,53	2,30	99,23	53,90
Dl5a-P2	Labradorite	50,56	28,70	3,45	0,68	11,65	3,86	0,60	99,49	60,22
Dl5c-Pma1	Andésine	55,58	27,16	1,53	0,27	10,06	5,62	0,32	100,54	48,82
Dl6b-Pma1	Bytownite	49,59	30,49	0,91	0,27	14,99	3,08	0,11	99,44	72,43
Dj2d-Pma1	Albite	67,54	19,21	1,33	0,39	0,63	11,37	0,18	100,63	2,92
Dj7g-Pma1	Albite	65,28	21,15	0,38	0,21	1,07	10,35	0,98	99,42	5,11
Dj10c-Pma1	Albite	66,55	19,58	0,82	0,70	0,29	11,42	0,11	99,48	1,39
Sm1b-Pma1	Oligoclase	51,71	31,73	1,63	0,89	1,39	1,19	6,19	94,74	12,71
Sm3e-Pma1	Labradorite	51,80	29,45	1,06	0,10	12,74	4,20	0,31	99,65	61,52
Sm4d-Pma1	Andésine	58,92	25,95	0,53	0,03	6,90	6,31	1,04	99,67	35,29
Jc1c-Pma1	Labradorite	51,38	29,98	0,82	0,22	13,50	3,83	0,22	99,95	65,25
Jc4c-Pma1	Labradorite	50,96	30,69	0,80	0,23	14,06	3,46	0,19	100,39	68,43
Jc5c-Pma1	Bytownite	50,00	30,23	1,25	0,79	14,09	3,03	0,37	99,76	70,43
Jc6b-P1	Labradorite	51,44	29,43	0,78	0,20	14,04	3,58	0,17	99,64	67,76
Jc7c-Pma1	Labradorite	52,41	28,72	0,93	0,22	13,20	3,98	0,23	99,69	63,84
Et2b-Pma1	Labradorite	53,17	27,95	0,79	0,18	11,34	4,47	0,84	98,74	55,50

Analyses de plagioclases (suite)

# Grain	Minéral	SiO ₂	Al ₂ O ₃	FeO ^{Total}	MgO	CaO	Na ₂ O	K ₂ O	Total	An (%)
<i>Contenu en % poids</i>										
Et3c-Pma1	Labradorite	52,58	29,23	0,82	0,37	12,52	4,01	0,62	100,13	61,06
Et4a-Pma1	Labradorite	51,46	29,83	0,88	0,22	13,45	3,91	0,17	99,91	64,90
Et4c-P1	Labradorite	52,31	28,47	1,27	1,07	13,10	4,04	0,17	100,41	63,58

Analyses d'oxydes par microsonde

# Grain	Minéral	SiO ₂	TiO ₂	Al ₂ O ₃	Cr ₂ O ₃	FeO	Fe ₂ O ₃	MnO	MgO	CaO	Total
<i>Contenu en % poids</i>											
Bc2e-Oxma1	Magnétite (riche en Ti)	0,07	11,98	2,56	1,39	30,05	51,24	0,09	0,15	0,16	97,69
Bc3a-Ox1	Magnétite	0,08	0,16	0,16	0,01	29,09	65,00	0,08	0,04	0,03	94,64
Bc3b-Ox1	Magnétite	0,03	0,19	0,33	0,02	29,23	64,54	0,03	0,04	0,02	94,43
Bc3c-Oxma1	Magnétite	0,11	2,18	0,27	0,03	27,04	62,51	0,36	0,88	0,27	93,65
Bc4g-Oxma1	Magnétite (riche en Ti)	0,23	15,23	2,61	0,97	27,45	48,03	2,05	0,17	0,19	96,91
Bc5e-Oxma1	Magnétite (riche en Ti)	0,27	13,39	1,46	0,71	27,80	50,43	1,53	0,22	0,15	95,96
Bc6e-Oxma1	Magnétite (riche en Ti)	0,12	15,68	2,32	0,27	29,73	47,40	0,12	0,03	0,18	95,84
Bc7g-Oxma1	Magnétite (riche en Ti)	0,09	16,70	2,49	0,71	27,14	46,61	2,23	0,09	0,16	96,21
Dl1a-Ox1	Magnétite (riche en Ti)	0,12	19,76	3,69	0,07	28,38	42,50	1,27	0,41	0,14	96,33
Dl1b-Ox1	Magnétite (riche en Ti)	0,12	18,10	3,82	0,06	28,34	44,24	1,64	0,34	0,08	96,72
Dl1c-Ox1	Magnétite (riche en Ti)	0,19	17,62	4,78	0,02	28,33	42,75	1,91	0,16	0,07	95,84
Dl1f-Ox1	Magnétite (riche en Ti)	0,22	21,36	3,99	0,04	29,06	39,83	0,77	0,11	0,14	95,51
Dl2f-Oxma1	Magnétite (riche en Ti)	0,21	16,11	4,08	0,02	29,59	45,08	0,06	0,03	0,39	95,57
Dl3a-Oxma1	Magnétite (riche en Ti)	0,14	22,05	2,01	0,01	27,76	43,01	2,37	0,05	0,35	97,74
Dl3b-Ox1	Magnétite	1,13	0,02	0,02	0,04	28,49	64,20	0,00	0,58	0,03	94,51
Dl6b-Oxma1	Magnétite (riche en Ti)	0,31	15,80	3,96	0,04	29,51	44,57	0,07	0,10	0,22	94,59
Dj1b-Oxma1	Magnétite	1,56	5,08	1,44	0,03	24,94	58,67	0,62	2,66	0,22	95,24
Dj4c-Oxma2	Magnétite (riche en Ti)	0,36	26,49	0,84	1,24	26,66	38,06	2,62	0,24	0,29	96,79
Dj3d-Oxma2	Ilménite	0,37	47,45	0,10	0,03	25,70	20,22	2,33	1,20	0,34	97,73
Dj5c-Oxma2	Magnétite (riche en Ti)	0,07	23,07	2,35	2,00	27,78	39,38	2,11	0,13	0,06	96,93
Dj6d-Oxma1	Magnétite (riche en Ti)	0,66	22,46	2,16	0,10	27,37	42,82	1,84	0,55	0,30	98,26
Dj6d-Oxma2	Magnétite (riche en Ti)	4,27	26,39	2,00	0,12	22,78	36,07	1,97	2,96	1,37	97,93
Dj7a-Ox1	Magnétite	0,07	6,06	5,24	1,28	27,56	55,15	1,22	1,49	0,21	98,27
Dj7b-Ox1	Magnétite (riche en Ti)	1,08	9,02	1,78	0,07	28,19	52,94	0,18	0,52	0,34	94,11

Analyses d'oxydes par microsonde (suite)

# Grain	Minéral	SiO ₂	TiO ₂	Al ₂ O ₃	Cr ₂ O ₃	FeO	Fe ₂ O ₃	MnO	MgO	CaO	Total
<i>Contenu en % poids</i>											
Dj7b-Ox1	Magnétite (riche en Ti)	0,16	17,20	3,67	0,09	29,20	43,38	0,19	0,05	0,33	94,27
Dj8d-Oxma1	Magnétite (riche en Ti)	0,18	20,17	2,12	2,29	27,89	42,45	1,74	0,14	0,33	97,31
Sm1f-Ox1	Magnétite (riche en Ti)	0,39	18,45	3,95	0,05	30,01	42,83	0,27	0,13	0,03	96,10
Sm1b-Ox1	Magnétite (riche en Ti)	0,15	19,52	2,71	0,06	29,67	43,09	0,33	0,03	0,04	95,59
Sm1b-Oxma1	Magnétite (riche en Ti)	2,58	17,44	2,27	0,00	27,57	43,40	0,74	0,29	0,41	94,69
Sm2f-Oxma1	Ilménite	0,18	45,58	0,17	0,25	25,20	22,51	3,32	0,97	0,33	98,50
Sm2f-Oxma2	Ilménite	0,23	57,39	1,06	0,12	21,25	10,39	0,12	5,39	0,27	96,23
Sm3a-Oxma1	Magnétite (riche en Ti)	0,28	13,01	2,38	1,28	26,83	49,17	1,10	1,00	0,29	95,34
Sm4a-Ox2	Magnétite (riche en Ti)	0,55	14,51	6,26	1,14	29,09	41,19	0,23	0,35	0,17	93,49
Sm4a-Ox1	Magnétite (riche en Ti)	0,92	15,77	4,24	0,59	29,10	43,17	0,28	0,38	0,11	94,56
Sm4b-Ox2	Magnétite (riche en Ti)	0,18	13,12	6,65	0,10	29,91	44,42	0,14	0,24	0,07	94,82
Sm4b-Ox1	Magnétite (riche en Ti)	0,08	13,04	5,88	0,37	29,95	45,11	0,20	0,01	0,09	94,72
Sm4b-Oxma1	Magnétite (riche en Ti)	0,12	17,07	2,20	0,45	29,37	45,46	0,21	0,01	0,18	95,07
Sm4f-Ox1	Magnétite (riche en Ti)	0,41	15,00	5,73	0,82	30,32	43,34	0,21	0,16	0,04	96,01
Jc2c-Oxma1	Magnétite (riche en Ti)	0,08	19,12	1,40	0,03	28,70	46,27	1,38	0,04	0,18	97,20
Jc5c-Oxma1	Magnétite (riche en Ti)	0,65	16,93	2,40	0,03	28,95	46,63	0,83	0,25	0,15	96,83
Et2c-Oxma1	Ilménite	0,03	48,33	0,07	0,00	27,92	18,85	2,06	0,09	0,03	97,38
Et3c-Oxma1	Ilménite	0,07	48,68	0,08	0,05	27,55	18,62	2,28	0,25	0,02	97,59
Et4a-Oxma1	Magnétite (riche en Ti)	0,19	15,80	1,46	2,54	28,31	45,98	0,63	0,10	0,46	95,47

Limites de détection des analyses par microsonde^a

SiO ₂	TiO ₂	Al ₂ O ₃	Cr ₂ O ₃	V ₂ O ₅	FeO	Fe ₂ O ₃ ^b	MnO ^b	MgO	CaO ^b	Na ₂ O ^b	K ₂ O ^b	NiO
<i>Valeurs en % poids</i>												
0,025	0,022	0,053	0,181	0,168	0,179	nd	nd	0,029	nd	nd	nd	0,238

^a Les valeurs disponibles ont été tirées de Pagé et Barnes (2009).

^b L'erreur analytique relative est d'environ 2% sur les éléments majeurs et de 10% sur les éléments traces.

ANNEXE 5 : ANALYSES DE CHROMITE PAR LA-ICP-MS

Concentrations en IEGP(Rh) et en Ni-Cu dans les chromites déterminées par LA-ICP-MS

# Grain	Os (ppb)	Ir (ppb)	Ru (ppb) *	Rh (ppb) *	Ni (ppm)	Cu (ppm)	Correspondance microsonde
Dl2b-Cm1	46	33	219	8	1563	7	Oui
Dl2c-Ci1	22	15	224	4	1681	6	Oui
Dl2d-Cb1	26	30	272	10	1475	11	Oui
Dl2e-Cm1	43	25	285	9	1802	11	Oui
Dl2f-Cm1	62	19	236	7	1209	16	Oui
Dl2g-Ci1	43	19	278	8	1731	9	Non
Dl2h-Cb1	31	17	231	6	1733	10	Non
Dl2b-Cb1	19	17	227	12	1194	8	Non
Dl3a-Cm1	39	19	230	8	1465	9	Oui
Dl3b-Ci1	45	20	217	11	1145	18	Oui
Dl3c-Cm1	22	14	180	8	1170	14	Oui
Dl3d-Ci1	34	21	238	7	1167	14	Oui
Dl4a-Cm1	12	18	226	14	1504	12	Oui
Dl4d-Cm1	15	7	222	16	1635	13	Oui
Dl4f-Ci1	29	21	226	9	1980	7	Oui
Dl6a-Cb1(a)	33	36	180	4	1510	7	Oui
Dl6a-Ci1	36	13	203	2	1653	7	Oui
Dl6a-Ci2	39	14	214	2	1665	5	Oui
Dl6a-Cb1(b)	43	29	196	4	1882	8	Oui
Dl6a-Cb2	81	44	402	8	3620	12	Non
Dl6a-Ci3	83	56	437	15	3880	10	Non
Dl6a-Ci4	129	56	381	10	3111	13	Non
Dl6a-Cm1	31	29	349	24	3071	9	Non
Bc2a-Ci2	36	26	271	10	1388	80	Oui
Bc2a-Cb1	38	45	229	22	1010	117	Non
Bc2b-Cm2	31	28	221	12	648	135	Non
Bc2d-Cm1	18	24	366	24	728	207	Oui
Bc2d-Ci1	38	31	448	19	2020	34	Non
Bc2i-Cb1	35	26	280	20	1258	133	Non
Bc2j-Ci1	39	33	335	21	1421	137	Non
Bc2j-Ci2	35	32	322	17	1468	147	Non
Bc2k-Cb1	23	34	286	7	1220	65	Non
Bc4c-Cm1(a)	41	27	248	27	830	118	Oui
Bc4d-Cb1	34	28	235	31	902	207	Oui
Bc4d-Ci1(a)	17	25	278	14	1208	61	Oui
Bc4e-Ci1(a)	56	36	284	15	1259	56	Oui
Bc4g-Cm1	36	17	173	38	734	346	Oui
Bc4c-Cm1(b)	27	26	264	15	825	124	Oui
Bc4d-Ci1(b)	32	25	225	14	1097	78	Oui
Bc4e-Ci1(b)	35	33	247	15	1250	68	Oui
Bc4e-Cb1	24	24	305	35	915	172	Oui

Concentrations en IEGP(Rh) et en Ni-Cu dans les chromites déterminées par LA-ICP-MS (suite)

# Grain	Os (ppb)	Ir (ppb)	Ru (ppb) [*]	Rh (ppb) [*]	Ni (ppm)	Cu (ppm)	Correspondance microsonde
Bc4i-Cb1	18	16	205	12	850	106	Non
Bc4i-Cb2	23	15	266	16	818	173	Non
Bc5a-Cb1(a)	62	32	333	31	1085	64	Oui
Bc5a-Cib1(a)	58	22	316	31	1182	93	Oui
Bc5a-Ci1	50	16	283	27	1202	113	Oui
Bc5a-Ci2	43	25	350	30	1277	100	Oui
Bc5c-Cm1(a)	68	44	214	9	1229	25	Oui
Bc5d-Ci1	50	40	266	18	1483	71	Oui
Bc5a-Cib1(b)	46	42	308	21	1199	110	Oui
Bc5a-Ci4	51	48	314	20	1145	105	Non
Bc5a-Cb1(b)	47	41	344	15	1390	76	Oui
Bc5c-Cm1(b)	65	40	210	12	1181	36	Oui
Bc5c-Cm1(c)	50	42	216	16	1167	43	Oui
Bc5c-Cm1(d)	56	39	237	14	1147	48	Oui
Bc5d-Ci1(b)	29	18	252	11	1415	74	Oui
Bc5d-Ci1(c)	29	27	234	13	1186	70	Oui
Bc5d-Cm1(a)	47	24	286	12	1190	58	Non
Bc5d-Cm1(b)	40	38	288	13	1327	52	Non
Bc5d-Ci2	46	38	324	12	1590	77	Non
Bc5e-Cm1	16	17	240	23	1151	69	Oui
Bc6a-Cm1	21	25	251	14	1635	20	Oui
Bc6b-Cm1	23	30	443	53	1560	32	Oui
Bc6c-Ci2	18	22	318	93	2360	17	Non
Bc6c-Ci1	22	19	323	24	1355	48	Oui
Bc6e-Cm1	15	34	151	36	1051	39	Oui
Bc6f-Cb1	43	49	385	25	2316	17	Non
Bc6g-Cm1	38	21	329	28	1518	28	Non
Bc7e-Ci1(a)	20	18	289	30	1383	87	Oui
Bc7f-Cm2	46	17	300	56	827	226	Oui
Bc7f-Cm1	21	12	187	29	713	170	Oui
Bc7g-Cb1(a)	51	50	289	39	1012	87	Oui
Bc7e-Ci1(b)	40	41	279	23	1396	63	Oui
Bc7g-Cb1(b)	51	42	253	39	1076	115	Oui
Bc7g-Ci1	38	40	319	59	1283	125	Non
Bc7g-Ci2	39	29	235	49	899	135	Non
Dj2d-Cm2	18	11	162	19	1774	27	Oui
Dj2d-Cm1	13	8	138	20	1990	30	Oui
Dj3a-Ci1	35	25	238	12	1741	10	Oui
Dj3c-Cb1	35	28	269	19	1648	52	Oui
Dj3e-Ci1	30	23	140	22	1486	48	Non
Dj3f-Cm1	42	27	236	12	1330	35	Oui

Concentrations en IEGP(Rh) et en Ni-Cu dans les chromites déterminées par LA-ICP-MS (suite)

# Grain	Os (ppb)	Ir (ppb)	Ru (ppb) [*]	Rh (ppb) [*]	Ni (ppm)	Cu (ppm)	Correspondance microsonde
Dj3f-Cm2	27	26	241	11	1341	37	Oui
Dj3g-Cm1	22	29	142	22	1637	18	Oui
Dj3g-Cm2	16	16	67	16	963	71	Oui
Dj4a-Cb1	21	11	284	7	1480	33	Oui
Dj4d-Cm1	13	12	91	11	1130	78	Oui
Dj4e-Cb2	28	25	288	36	1412	86	Oui
Dj4e-Cb1	52	36	411	47	1319	115	Oui
Dj4f-Ci2	25	17	415	21	1671	17	Oui
Dj4c-Cm1	28	12	312	26	1284	79	Oui
Dj5a-Ci1	19	24	203	34	1489	70	Oui
Dj5e-Cb1(a)	16	20	249	21	1278	75	Oui
Dj5e-Cb1(b)	19	15	141	9	609	78	Oui
Dj5f-Cb2	16	18	322	36	1423	87	Non
Dj6a-Cm1	40	12	275	22	1469	48	Oui
Dj6c-Cb1	19	16	263	24	1341	42	Oui
Dj6d-Cm1	93	26	364	21	1409	57	Oui
Dj6e-Cb1	38	17	327	40	1304	63	Oui
Dj6e-Ci2	29	23	291	36	1556	47	Oui
Dj6f-Cm1(a)	80	20	315	28	1324	60	Oui
Dj6e-Cb2	23	13	309	22	1238	82	Non
Dj6f-Cm1(b)	25	21	248	15	1205	71	Oui
Dj6g-Cm1	17	11	307	20	1538	59	Non
Dj8a-Ci1(a)	17	15	283	18	1277	24	Oui
Dj8b-Cm1(a)	32	23	336	27	1449	73	Oui
Dj8c-Ci1	51	35	311	31	1431	67	Oui
Dj8c-Ci2	37	20	242	41	1206	119	Oui
Dj8d-Cb1(a)	15	11	268	22	1195	62	Oui
Dj8e-Cm1	30	15	309	40	1283	102	Oui
Dj8a-Ci1(b)	12	14	271	16	1310	23	Oui
Dj8a-Ci1(c)	15	15	205	13	1140	38	Oui
Dj8b-Cm1(b)	39	29	281	27	1302	102	Oui
Dj8b-Cm1(c)	27	22	299	21	1375	88	Oui
Dj8b-Cb1	15	17	257	25	1302	96	Non
Dj8b-Cb2	21	20	243	15	1300	60	Non
Dj8d-Cb1(b)	22	13	269	18	1230	55	Oui
Dj8d-Ci1	17	23	235	17	1113	149	Non
Dj8g-Cm1	16	14	182	22	1417	66	Non
Dj9a-Cm1	40	14	75	30	817	165	Oui
Dj9b-Ci1	23	18	105	34	1098	297	Oui
Dj9c-Ci1	17	11	52	25	1184	204	Oui
Dj9e-Cb1(a)	91	21	148	19	1021	165	Oui

Concentrations en IEGP(Rh) et en Ni-Cu dans les chromites déterminées par LA-ICP-MS (suite)

# Grain	Os (ppb)	Ir (ppb)	Ru (ppb) [*]	Rh (ppb) [*]	Ni (ppm)	Cu (ppm)	Correspondance microsonde
Dj9b-Ci2	21	21	90	15	1096	331	Non
Dj9b-Ci3	17	23	116	20	1491	503	Non
Dj9e-Cb1(b)	35	30	113	6	1064	206	Oui
Dj9f-Cm1	14	12	87	9	857	291	Oui
Sm2b-Cm1(a)	32	18	276	28	982	180	Oui
Sm2c-Ci1	36	24	159	43	1282	264	Oui
Sm2c-Ci2	30	11	188	42	1183	303	Oui
Sm2e-Cm1(a)	23	23	290	39	847	192	Oui
Sm2h-Cb1(a)	56	25	149	53	1274	212	Oui
Sm2a-Cb1	14	12	78	18	1158	265	Oui
Sm2b-Cm1(b)	27	19	316	22	1122	164	Oui
Sm2e-Cm1(b)	10	26	304	24	853	241	Oui
Sm2h-Cb1(b)	15	14	139	32	1261	248	Oui
Sm2i-Ci1	17	17	75	26	1960	291	Non
Sm2j-Ci1	32	24	212	46	1660	197	Non
Sm3a-Cm1	21	14	192	41	1506	114	Oui
Sm3b-Cm1	12	16	233	25	1302	78	Oui
Sm3c-Cm1	18	21	151	41	1529	128	Oui
Sm3g-Cb1	19	17	212	55	1534	371	Oui
Sm3g-Ci1	25	15	259	24	1284	214	Oui
Sm3g-Ci2	21	28	141	31	1318	221	Oui
Sm3h-Ci1	15	15	158	11	1445	21	Non
Sm3i-Cb1	26	25	195	20	1306	154	Non
Jc1a-Ci1	27	21	177	13	1128	14	Oui
Jc1a-Ci2	35	23	325	17	1305	22	Oui
Jc1a-Ci4	36	30	265	15	1689	18	Non
Jc1b-Ci1	37	28	298	23	1549	21	Oui
Jc1b-Ci2	8	15	176	23	1519	24	Oui
Jc1c-Cb1	25	14	360	16	1326	22	Oui
Jc1c-Cb2	31	27	348	27	1339	26	Oui
Jc1d-Ci1	24	17	258	17	1247	21	Oui
Jc1d-Ci2	15	12	242	26	1263	22	Oui
Jc1d-Cb1	22	15	324	21	1323	25	Non
Jc2a-Ci1	23	23	357	44	1845	21	Oui
Jc2a-Cb1	19	18	231	30	1230	13	Oui
Jc2a-Cm1	20	26	281	35	1558	18	Oui
Jc2a-Ci2	27	24	192	21	1423	11	Oui
Jc2b-Cb1	25	23	205	23	1227	16	Oui
Jc2b-Cm1	19	19	218	23	1349	15	Oui
Jc2c-Ci1	21	20	221	29	1324	16	Oui
Jc2c-Ci2	28	28	264	29	1365	15	Oui

Concentrations en IEGP(Rh) et en Ni-Cu dans les chromites déterminées par LA-ICP-MS (suite)

# Grain	Os (ppb)	Ir (ppb)	Ru (ppb) [*]	Rh (ppb) [*]	Ni (ppm)	Cu (ppm)	Correspondance microsonde
Jc2c-Ci3	12	14	153	23	1108	19	Non
Jc2d-Cb1	31	21	212	15	1512	10	Oui
Jc2e-Ci1	19	19	247	29	1429	15	Non
Jc2f-Cb1	35	18	161	24	1431	16	Non
Jc2g-Cm1	34	14	153	42	1367	18	Non
Jc2g-Ci1	21	21	259	46	1552	12	Non
Jc3a-Ci1	97	53	240	12	1271	23	Oui
Jc3b-Cm1	28	30	211	36	1264	27	Oui
Jc3c-Ci1	23	25	222	30	1180	9	Oui
Jc3d-Cm1	16	6	98	10	1017	23	Oui
Jc3e-Ci1	9	20	154	50	1319	66	Non
Jc3f-Cb1	8	7	54	26	931	62	Non
Jc3g-Ci1	14	24	177	27	1229	10	Non
Jc4a-Ci1	32	25	305	12	1140	19	Oui
Jc4a-Cb1	36	30	343	29	1198	45	Oui
Jc4b-Cb1	55	42	213	14	1369	18	Oui
Jc4c-Cb1	14	18	97	19	1247	18	Oui
Jc4d-Cm1	17	21	190	23	1715	23	Oui
Jc4e-Ci1	46	17	293	11	1312	28	Non
Jc6a-Cb1	29	14	304	65	1531	776	Oui
Jc6a-Cb3	18	17	269	60	1540	828	Oui
Jc6b-Cb1	17	19	350	56	1534	526	Oui
Jc6b-Ci1	24	20	399	65	1820	494	Non
Jc6b-Ci2	38	31	283	37	1405	299	Oui
Jc6b-Ci4	34	23	325	67	1567	523	Non
Jc6c-Ci1	31	22	287	17	1193	89	Oui
Jc6d-Cm1	17	15	172	41	734	401	Oui
Jc6e-Cb1	29	23	337	56	1303	674	Oui
Jc7a-Cb1	73	39	294	14	1136	25	Oui
Jc7a-Cm1	32	25	222	21	1188	22	Oui
Jc7b-Cm1	31	22	271	7	1250	17	Oui
Jc7c-Cb1	13	16	151	17	1220	17	Oui
Jc7d-Cb1	25	26	93	15	1683	22	Oui
Jc7d-Ci1	14	11	208	13	1429	15	Oui
Jc7e-Cm1	12	16	305	17	1276	27	Non
Jc7e-Cb1	53	23	320	21	1300	21	Non
Jc7f-Cb1	58	35	319	12	1466	30	Non
Jc7g-Cm1	18	23	313	13	1490	19	Non
Et2b-Cb1	142	50	166	9	1096	26	Oui
Et2b-Cb3	57	32	97	17	1057	44	Non
Et2b-Cb2	77	36	143	12	1053	34	Oui

Concentrations en IEGP(Rh) et en Ni-Cu dans les chromites déterminées par LA-ICP-MS (suite)

# Grain	Os (ppb)	Ir (ppb)	Ru (ppb) [*]	Rh (ppb) [*]	Ni (ppm)	Cu (ppm)	Correspondance microsonde
Et2b-Ci1	83	36	122	16	1153	42	Oui
Et2c-Cb1	93	42	110	12	1140	23	Oui
Et2c-Ci1	151	49	256	14	946	60	Non
Et2d-Ci1	64	40	203	31	1603	7	Oui
Et2e-Cm1	56	27	190	27	878	72	Non
Et3a-Ci1	124	48	155	11	1204	24	Oui
Et3a-Ci2	55	22	161	17	794	60	Non
Et3b-Cb1	49	37	104	17	1070	32	Oui
Et4a-Cm1	29	29	222	23	1016	15	Oui
Et4b-Cm1	68	48	280	20	1579	21	Oui
Et4c-Cb1	52	38	260	23	1194	20	Oui
Et4d-Cb1	89	52	334	13	1698	13	Oui
Et4d-Cm1	67	39	312	15	1367	13	Oui
Et4e-Cb1	61	30	248	21	1606	14	Non
Et4e-Ci1	57	40	216	23	1508	17	Non
Et4g-Cb1	78	35	253	9	1036	15	Non
Et4h-Cm1	88	49	366	16	1687	13	Non
Et4h-Cb1	34	23	205	7	614	7	Non

* Valeurs corrigées pour les interférences Ni-Ar et Cu-Ar. Les détails concernant la correction des interférences sont donnés dans la section *Sample locations and analytical methods* du Chapitre 2.

**ANNEXE 6 : MATÉRIAUX DE RÉFÉRENCES POUR LES ANALYSES
PAR LA-ICP-MS**

Compositions des matériaux de références et du moniteur de chromite AX37

	Os (ppm)	Ir (ppm)	Ru (ppm)	Rh (ppm)	Ni (ppm)	Cu (ppm)	Fe (wt.%)
<i>Valeurs acceptées</i>							
Laflamme Po727 ^a	46,7±2,6	48,0±1,2	36,5±0,3	41,6±0,3			61,07±0,21
GSE-1G ^b					440±30	380±40	9,87±0,23
AX37 ^c	0,016±0,006	0,019±0,009	0,304±0,042	0,015±0,007			
<i>Valeurs obtenues</i>							
Laflamme Po727 (n = 36)	46,7±0,8	48,0±0,8	36,5±0,4	41,6±0,4			
GSE-1G (n = 36)					440±2	380±2	
AX37 (n = 30)	0,018±0,004	0,014±0,004	0,274±0,029	0,012±0,002	1056±128	5,41±0,63	

^a Valeurs tirées du certificat d'analyse du *Memorial University of Newfoundland*, Sylvester, P. J., 2006.

^b Valeurs pour le Ni et le Cu tirées de la base de donnée de GeoReM, et valeur pour le Fe tirée de Jochum et al. (2005; *Geostandards and Geoanalytical Research* 29 (3), 285-302)

^c Valeurs basées sur 63 analyses par LA-ICP-MS effectuée au LabMaTer de l'Université du Québec à Chicoutimi.